QUADRUPOLE MOMENTS IN THE CADMIUM ISOTOPES

by

Mehmet Tezer Esat

A thesis submitted to

The Australian National University

for the degree of

Doctor of Philosophy

September 1976

"They're all made out of ticky-tacky,

And they all look just the same"

- words of popular song.

PREFACE

This thesis describes a series of experiments designed to measure the quadrupole moments Q_{2^+} of the stable even-mass cadmium isotopes. The work was carried out in the Department of Nuclear Physics at the Australian National University under the supervision of Drs. R. H. Spear and D. C. Kean.

The project was initiated by Dr. Kean. The work was carried out jointly by Dr. Kean, Dr. Spear and myself with assistance from Dr. R. A. I. Bell in the initial stages and Dr. A. M. Baxter in the final stages. Analysis of the data was largely performed by myself. Dr. Kean wrote the least-squares program for the extraction of B(E2) and Q_{2^+} values from the data and handled most of this portion of the analysis. Other computer programs, including the non-linear least-squares fitting routine, were written by me.

Some of the work described in this thesis has appeared or will appear in the following publications:
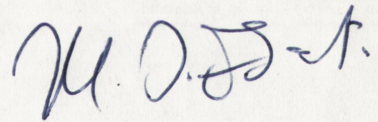
(1) Quadrupole Moments in the Cadmium Isotopes,

M. T. Esat, D. C. Kean, R. H. Spear and R. A. I. Bell,

Phys. Lett. <u>61B</u> (1976) 242.

(2) Mass Dependence of the Static Quadrupole Moments of the

First 2^+ States in the Cadmium Isotopes,

M. T. Esat, D. C. Kean, R. H. Spear and A. M. Baxter,

to be published in Nuclear Physics.

(3) Vibrational Excitations in the Even-Mass Cadmium Isotopes,

R. H. Spear, M. T. Esat, D. C. Kean, A. M. Baxter, M. P. Fewell,

S. M. Hinds, A. M. Joye and J. P. Warner,

to be published.

It is a pleasure to thank Drs. Spear and Kean for their supervision and guidance during the course of this work. I must also thank them for their comments and constructive criticism during the writing of this thesis.

I am indebted to my wife, Sevilay, for her patience throughout this work and for undertaking to type this thesis.

Finally, I would like to thank Professor J. O. Newton for the opportunity of working in the Department of Nuclear Physics and the Australian National University for the award of a Postgraduate Scholarship.

No part of this thesis has been submitted for a degree at any other university.

M. T. Esat.

Canberra,

September 1976.

TABLE OF CONTENTS

ABSTRACT

The static quadrupole moments Q_{2^+} and the B(E2; $0^+ \to 2^+$) values of the first 2^+ states in the even-mass cadmium isotopes have been determined using the reorientation effect. The Coulomb excitation probabilities were measured by resolving the inelastically and elastically backward-scattered ^{4}He and ^{16}O projectiles in an annular surface barrier detector. The results, in contrast to theoretical predictions and previous experimental work, indicate no significant variation of Q_{2^+} with mass number. On the basis of these and other results, it is argued that the cadmium isotopes possess a relatively uniform vibrational character.

CHAPTER 1.

INTRODUCTION

More than ten years ago de Boer et al. (de Bo 65) used the reorientation effect to make the initial measurement of the static quadrupole moment Q_{2^+} of the first 2^+ state of ^{114}Cd. Since then, Q_{2^+} has been measured in about 70 nuclei throughout the periodic table, from ^{18}O to ^{206}Pb. Most of the measurements are concentrated in the mass A=100 region in Ru, Pd, Cd, Sn and Te nuclei (Hä 74, Kl 75). In particular, "The study of the ^{114}Cd first excited state quadrupole moment", has been a recurring theme in numerous publications and conference reports (see, for example, Smilansky, Sm 71). The present thesis describes a series of experiments designed to measure the quadrupole moments Q_{2^+} of all the stable even-A cadmium isotopes. Included among these is the 12th measurement of ^{114}Cd quadrupole moment. No apologies are intended for remeasuring it; indeed there may be others in the future. That our results will survive the scrutiny of future experimenters is not to be taken for granted. Reorientation effect measurements have been notorious in this respect, mainly due to advances in experimental techniques and the elucidation of small additional effects which when correctly accounted for have altered significantly the conclusions reached in some of the earlier experiments. Included among these extraneous effects are attenuation of gamma-ray angular distributions (Go 68), Coulomb-nuclear interference (Wa 70) and the virtual excitation of the giant dipole resonance (de Bo 68). The present study is not so much concerned with ^{114}Cd but primarily with the mass dependence of Q_{2^+} in the cadmium isotopes. The issue is controversial (Ha 74), with theoretical inter- pretations whose evaluation is rendered difficult due to conflicting experimental results (Ha 75).

The nucleus ^{114}Cd is a text book example of a good vibrational nucleus. The original measurement of Q_{2+} in ^{114}Cd (de Bo 65), however, resulted in a large value (Q_{2+} = -0.7 e.b) and was close to that predicted by the rotational model. The basic rotational and harmonic vibrational models are fairly successful in describing the prominent features of a large number of nuclei. Low lying excited states of these nuclei are strongly coupled by quadrupole excitations. In certain well defined mass regions these levels can be identified as members of the ground state rotational band expected from deformed rotating nuclear shapes. In other regions (e.g. Z=50) spherical shapes dominate; the low lying energy spectra of these nuclei can be described by assuming that the individual nucleons participate in collective surface oscillations similar to vibrations in a liquid drop. The basic properties of these two models with regard to energy spectra, transition probabilities and predictions for Q_{2+} will be briefly discussed in the following sections. Initially, however, the static quadrupole moment is defined in section 1.1, and section 1.2 deals with the predictions of the extreme single particle model for ground state quadrupole moments.

1.1 The Electric Quadrupole Moment

The interaction energy between a system of charges with charge density ρ and an externally applied electric field E can be expressed as

$$H = q\phi_0 - \underline{P} \cdot \underline{E}_0 - \frac{1}{6} \sum_{ij} Q_{ij} (\delta E_j / \delta x_i)_0 - \dots \quad , \qquad (1.1)$$

where ϕ is the electrostatic potential due to $\underline{E}$ and o denotes the origin of coordinates for the charge distribution. The first term is the inter- action energy due to a "point" charge $q = \int \rho \, dv$, the second term gives the energy of a dipole $\underline{P} = \int \rho \underline{r} \, dv$ and the third term is the energy of a quadrupole where $Q_{ij} = \int \rho (3x_i x_j - \delta_{ij} r^2) \, dv$ is the electric quadrupole

tensor. Equation 1.1 shows that P can be deduced from the shift in the energy of the system in an externally applied electric field and that Q_{ij} produces an energy shift provided the field gradient is non-zero.

For nuclei the field E may be due to atomic electrons or to molecular fields, or the projectile charge in a collision process. Nuclear states with well defined parity cannot have odd order electric multipole moments; in particular, the dipole moment P is zero. The principle of time reversal invariance also requires that odd order electric moments are zero (Bo 69). The lowest order electric moment, apart from the monopole term in equation 1.1, is therefore the electric quadrupole. Since nucleons possess orbital angular momentum, current distributions inside the nucleus can give rise to magnetic multipole moments. The magnetic dipole moment is by far the largest and from arguments similar to those above only odd order magnetic multipoles are possible. No experimental evidence exists, however, for static magnetic moments higher than dipole.

For a spheroid with symmetry axis x_3 $Q_{ij}=0$ for $i \neq j$ and $x_1 = x_2$. The quadrupole interaction energy can then be written as

$$\Delta H_Q = - \frac{1}{4} (\delta E | \delta x_3)_0 \int \rho (3x_3^2 - r^2) \, dv = \frac{eQ}{4} (\delta E | \delta x_3)_0 \quad , \quad (1.2)$$

where Q is called the electric quadrupole moment. Quantum mechanically Q has to be related to a specific direction; in nuclei this is chosen to be along the total angular momentum vector J. The quadrupole moment is defined as the expectation value of operator Q_{33} in the state in which the z-component of J has its maximum value:

$$eQ = e\langle Q_{33} \rangle_{M=J}$$

$$= e\langle JJ | (3x_3^2 - r^2) | JJ \rangle$$

$$= e\langle JJ | (16\pi/5)^{\frac{1}{2}} r^2 Y_{20}(\theta,\phi) | JJ \rangle \quad , \quad (1.3)$$

where Y_{20} is the spherical harmonic function, (r,θ,ϕ) are the nuclear coordinates and the term $|J, M=J>$ represents the wave function of a nuclear state with spin J and z-component M=J. For a spherical charge distribution Q=0. Quadrupole moment measurements, therefore, probe the deviation from spherical symmetry of the nuclear charge distribution. The measured deviation relates to a particular state $|JJ>$ and may vary between the different states of the same nucleus.

As stated earlier a uniform electric field applied over the nuclear volume does not produce a net change in the interaction energy of the nuclear charge distribution with the electric field. The determination of Q in general involves the measurement of the quadrupole interaction energy in an electric field gradient (EFG). The experimental quantity determined is the product of the EFG and Q. The EFG must then either be calculated or measured independently in order to extract Q.

Assuming a uniform field gradient V_z in the z direction, the quantum mechanical equivalent of equation 1.2 is

$$\Delta H_Q = e \ Q \ V_z \left(3M^2 - J(J+1) \right) / 4J(2J-1) \quad , \qquad (1.4)$$

and an associated characteristic precession frequency w_Q can be defined as (Fr 65)

$$w_Q = - \ e \ Q \ V_z \ / 4J(2J-1) \ \hbar \quad . \qquad (1.5)$$

Equation 1.4 indicates that for $J = 0$ or $J = \frac{1}{2}$, ΔH_Q is undefined. In general nuclear states with spin $J = 0,\frac{1}{2}$ do not produce a measurable change in the interaction energy H (equation 1.1). The charge distribution of such states, however, need not be spherically symmetric. The quadrupole interaction is quadratic in M; therefore magnetic substates differing in the sign of M will not be split in an EFG (the magnetic dipole interaction is linear in M and an additional magnetic field removes the degeneracy).

1.2 The Extreme Single Particle Model

Properties of individual nuclei can in principle be determined from the experimentally deduced nucleon-nucleon potential. This is a complex many-body problem and is only approximately soluble. In the simple shell model approach the interaction between a single nucleon and all the others in the nucleus is replaced by a one-body potential. The properties of the nucleus such as spin, electric and magnetic moment and energy levels are ascribed to the behaviour of a few individual nucleons outside an inert core. The nucleons are assumed to fill states in a potential, composed of a central and spin-orbit part, in accordance with the Pauli exclusion principle. The neutrons and protons fill separate potentials. The experimentally observed magic numbers correspond to shell closures indicated by energy gaps in the calculated level sequence. A completely filled shell is assumed to be inert with nucleons coupled to zero spin. In the extreme single particle model the extra core nucleons are assumed to couple in pairs to zero spin. Thus the ground state spin of an odd-even nucleus is determined by the last unpaired nucleon. A particle hole in an otherwise closed shell behaves in a manner similar to a single particle.

In the simplest case the ground state quadrupole moment of a single particle or a single hole nucleus can be determined from equation 1.3 using the appropriate wave functions $|JJ>$. For a single proton the result is

$$Q_{sp} = -e \frac{2J-1}{2J+2} <r^2> \quad , \tag{1.6}$$

where $<r^2>$ is the mean square distance of the proton from the centre of the nucleus. For single proton nuclei near major closed shells predictions of equation 1.6 are in agreement with the experimentally determined values (see for example Bo 69a). In an odd neutron nucleus Q_{sn} is non-zero due to the recoil motion of the rest of the nucleus and a value similar to that

given by equation 1.6 is experimentally found. The quadrupole moment for proton hole nuclei should be positive, since a proton hole is equivalent to a particle with negative charge. Thus in the extreme single particle picture the sign of Q should change from positive to zero to negative as a major shell is filled at the magic numbers. The experimentally determined ground state quadrupole moments are shown in figure 1.1. The predicted behaviour at the magic numbers is clearly demonstrated. The ordinate in figure 1.1 Q/ZR^2 is a measure of deformation which compensates for the increasing size of nuclei. According to equation 1.6, $Q/ZR^2 \sim 1/Z$, whereas many nuclei have values much larger than this (fig. 1.1). Moreover there is a predominance of prolate shapes. Therefore, while the measured ground state quadrupole moments provide evidence for shell structure, the observed large moments can only be accounted for if a significant fraction of protons in the nucleus contribute to the quadrupole moment. This observation played a prominent part in the development of collective models (Ra 50).

Further evidence against the predictions of the single particle model can be obtained from an examination of the low lying energy spectra of some nuclei. The separation between major shells is about 4-6MeV and the spacings between subshells is roughly 1MeV. Therefore excited states in this picture should occur at least at 1MeV excitation relative to the ground state. Experimentally two major types of energy spectra are observed in even-even nuclei. For those nuclei near closed shells the first excited 2^+ states occur at ~0.5MeV excitation, in others away from closed shells the first excited states are found at ~100keV excitation. Such nuclei are broadly classified as vibrational and rotational respectively. Their properties can best be described in terms of coordinated collective effects. The main features of these models will be discussed below.
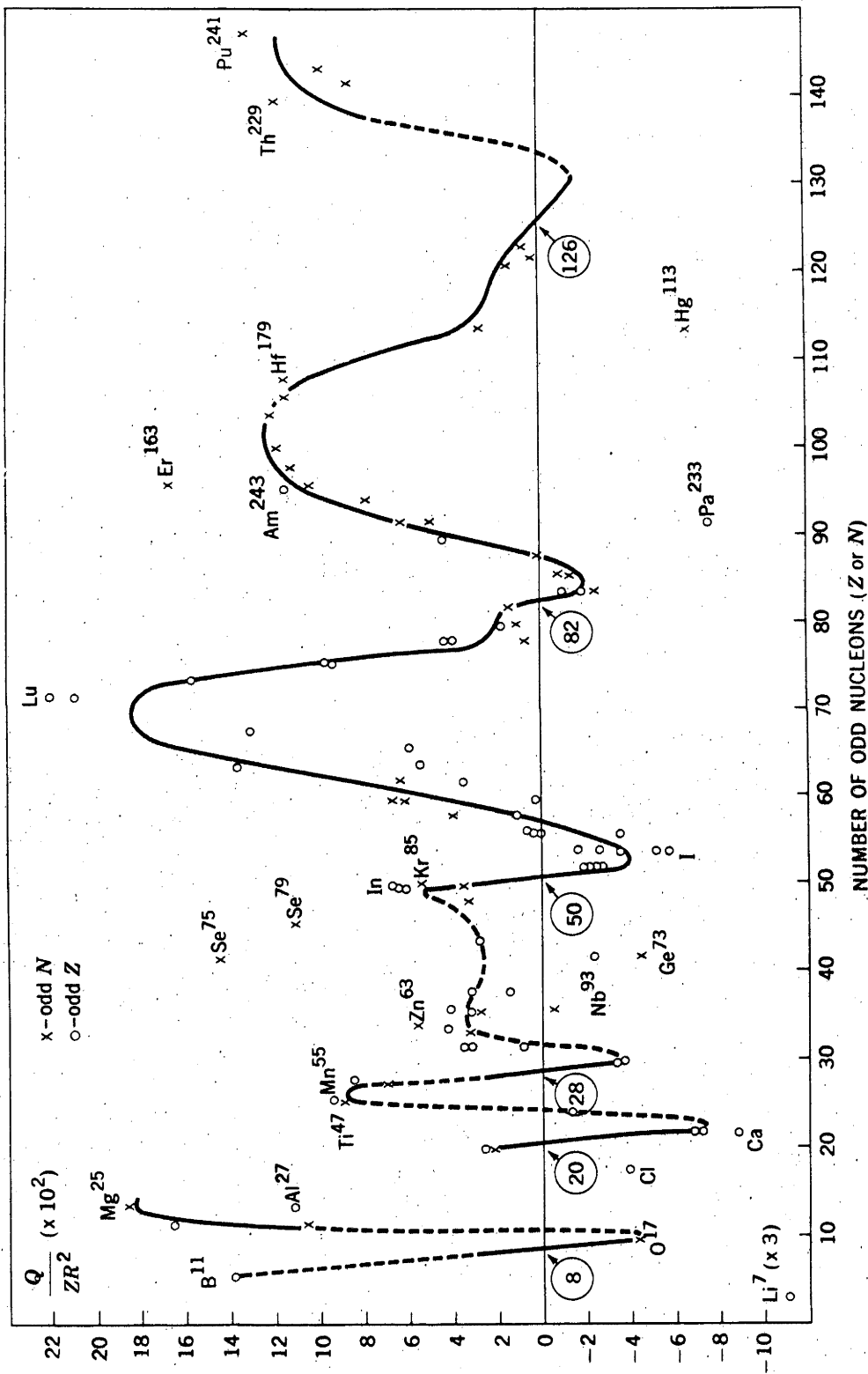
Figure 1.1. Quadrupole moments of odd-mass nuclei. The change from positive to negative values at closed shells is strikingly evident. Regions of large deformation occur near nucleon numbers 70, 100 and 140. Diagram reproduced from B. L. Cohen (Co 71).

1.3 Rotational Model

The occurrence of large quadrupole moments away from closed shells (fig. 1.1) suggests the existence of permanently deformed nuclear shapes. The deformation can be attributed to the polarizing effect of the outer nucleons on the otherwise spherical core. In even-even nuclei the lowest order excitations can be related to the rotation of an axially symmetric spheroid about an axis perpendicular to the symmetry axis. The extracore nucleons couple to zero spin and the total angular momentum $\underline{J}$ of the system is due to its rotation. Only even values of $\underline{J}$ are allowed and the energy spacing is proportional to $J(J+1)$. For example $E_{4^+}/E_{2^+} = 10/3$. Enhanced E2 gamma transitions occur between the successive members of the band and relations such as

$$B(E2; \; 4^+ \to 2^+) = \frac{10}{7} B(E2; \; 2^+ \to 0^+) \quad , \tag{1.7}$$

$$Q_{2^+} = \pm 0.91 \left(B(E2; \; 0^+ \to 2^+) \right)^{\frac{1}{2}} \text{ e.b} \quad , \tag{1.8}$$

can be derived through a detailed treatment (see for example Pr 75). In the more general case where the component of angular momentum K along the symmetry axis is non-zero the quadrupole moment can be obtained from equation 1.3 using the appropriate wave functions $|JJ\rangle$. The result is

$$Q = \left\{ \left(3K^2 - J(J+1) \right) / (J+1)(2J+3) \right\} Q_0 \quad , \tag{1.9}$$

where Q_0 is called the intrinsic quadrupole moment and is defined with respect to the symmetry axis of the nucleus. In the ground state band K=0 and Q will be negative for prolate shapes $(Q_0 > 0)$.

1.4 Vibrational Model

In even-even nuclei near closed shells a simple form of

collective behaviour arises from excitation modes due to small oscillations about a spherical equilibrium shape. These are analogous to the oscillations of a charged liquid drop. The distorted surface of a liquid drop can be parametrized in terms of spherical harmonic functions $Y_{\lambda\mu}(\theta,\phi)$ with amplitudes $\alpha_{\lambda\mu}$. The vibrations of the surface are represented through the time dependence of $\alpha_{\lambda\mu}$. Quantum mechanically λ is interpreted as the angular momentum carried by the vibration or phonon and μ is its z-component. The $\lambda=0$ phonon state is independent of θ and ϕ and vibrations of this type would correspond to compression modes which are unlikely at low energy. The $\lambda=1$ modes describe the vibrations of the centre of mass. Therefore the lowest order excitation will correspond to a $\lambda=2$ mode with one $\lambda=2$ phonon. One $\lambda=3$ phonon has roughly the same energy as two $\lambda=2$ phonons. The observed structure of vibrational type nuclei indicates that in most cases there is a triplet of states 0^+, 2^+, 4^+ at roughly twice the energy of the first excited 2^+ state and they are identified as the $\lambda=2$ two phonon states. Similarly higher excited states can arise from one $\lambda=4$ phonon, or from the coupling of three $\lambda=2$ phonons with 0^+, 2^+, 3^+, 4^+, 6^+ members which are degenerate in energy. In a more realistic model the degeneracy of these states will be removed and the triplet, and the quintuplet split. In figure 1.2 the sequence of levels expected from the simple vibrational model is shown together with the low lying level scheme for ^{114}Cd which is generally regarded as a good example of a vibrational nucleus. The agreement of level energies and spins in ^{114}Cd with that of simple vibrator is good; there are, however, two additional levels 0^+ and 2^+ which are not accounted for. These could be the depressed members of the quintuplet or possibly correspond to single particle excitations. The spin assignment of the 1957 keV level as 3^- is controversial (Gi 74, Sp 76) but it, most likely, is the $\lambda=3$ octupole state. The simple vibrational model is also able to make predictions
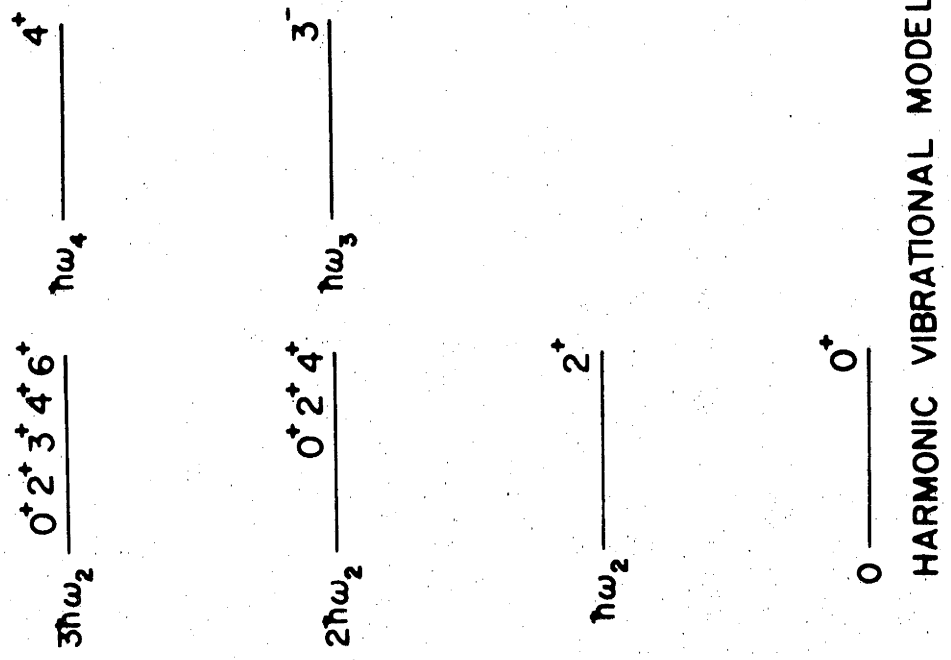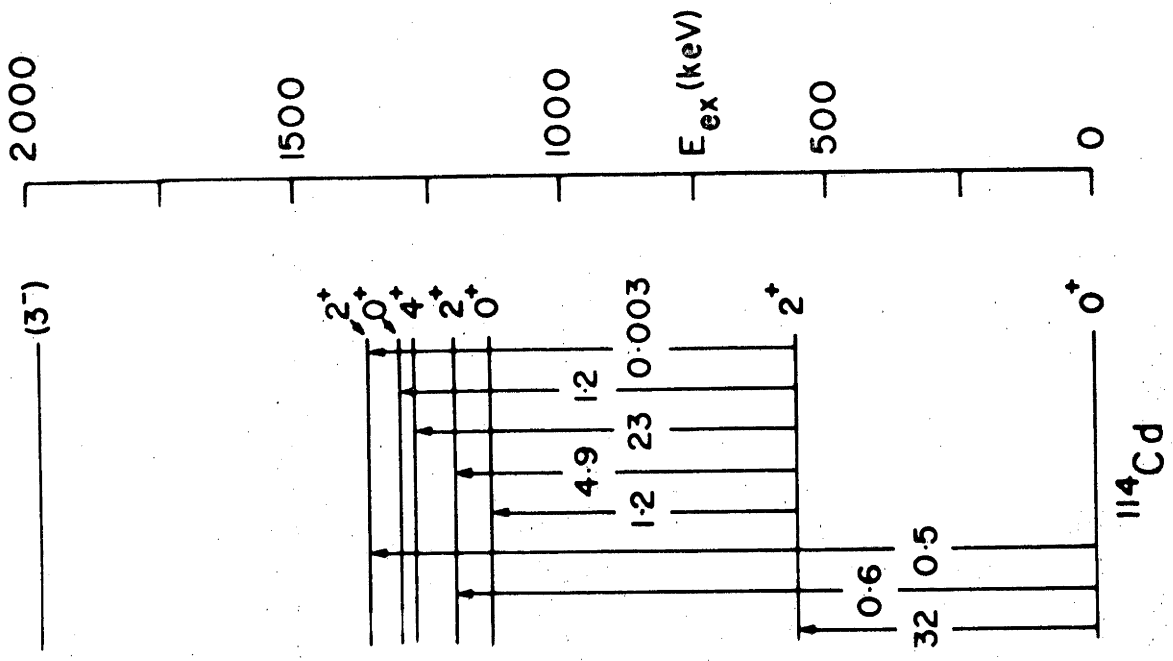
Figure 1.2.

The sequence of levels and their relative energies $(E=\hbar\omega_\lambda)$ expected from the simple harmonic vibrational model. The low lying level scheme of ^{114}Cd has been included for comparison. The transition strengths shown are in Weisskopf units.

about the electromagnetic decay properties of vibrational states; these
are as follows (see for example Pr 75):

a) There should be enhanced E2 transitions from the first excited 2^+
state to the ground state and from the members of the two phonon
triplet ($0^{+'}$, $2^{+'}$, 4^+) to the 2^+ state. In particular

$$B(E2; \ 2^{+'} \rightarrow 2^+) = 2B(E2; \ 2^+ \rightarrow 0^+) \quad , \tag{1.10}$$

$$B(E2; \ 4^+ \rightarrow 2^+) = 2B(E2; \ 2^+ \rightarrow 0^+) \quad . \tag{1.11}$$

In figure 1.2 the observed transition strengths are given in terms of
single particle estimates (We 51). The $2^+ \rightarrow 0^+$ transition is enhanced
by a factor of 30 over the single particle value. Relation 1.11 is in
good agreement with the experimental values (cf. equation 1.5) whereas
1.10 is not. This feature is also observed in other vibrational nuclei.

b) No transitions can occur between states which differ in phonon number
by more than one. For example cross-over transitions between the $2^{+'}$
and 0^+ state in ^{114}Cd should be zero. In practice this transition
strength is small compared with the $2^+ \rightarrow 0^+$ transition (fig. 1.2).

c) The harmonic vibrational model predicts zero quadrupole moment for the
one phonon 2^+ state. The generally accepted experimental value of Q_{2^+}
in ^{114}Cd is -0.4 e.b (Kl 75) which is not much smaller than the value
Q_{2^+} = -0.7 e.b (equation 1.8) predicted by the rotational model.

The possible existence of large quadrupole moments in nuclei
well described by the vibrational model has stimulated extensive experi-
mental investigation (Kl 75). Many other vibrational nuclei have been
found to possess relatively large quadrupole moments. These results have
necessitated the revision of nuclear theories dealing with such nuclei
(see for example Ta 66 and chapter 5). Although advances have been made
in this direction a satisfactory explanation for the measured Q_{2^+}'s
together with the electromagnetic properties of the low lying energy

levels awaits advances in theoretical understanding and mathematical techniques, together with more detailed and precise measurements over a wide mass region (Hä 74). In particular the systematic determination of the variation of Q_{2^+} with neutron number for a given element provides an exacting test of the applicability of the various nuclear theories to such nuclei (see section 1.5).

1.5 The Previous Situation Regarding the Quadrupole Moments in the Cadmium Isotopes

A summary of the previous results for Q_{2^+} in the cadmium isotopes is shown in figure 1.3. Included are the values from the compilation of Christy and Häusser (Ch 72) and the recent results of Hall et al. (Ha 75) for $^{106, 108, 116}$Cd. The two curves represent theoretical calculations. One is by Sorensen (So 73), using a boson expansion method, and the other is a particle-vibration coupling calculation by Sips (Si 71). It is clear from this diagram that a satisfactory evaluation of theoretical predictions is prevented by the confusion among the experimental results for $^{106, 108}$Cd. Furthermore, the value for ^{116}Cd is surprisingly large in magnitude compared to the now generally accepted value of -0.4 e.b (Kl 75) for the neighbouring isotope ^{114}Cd. The first calculation is in agreement with the earlier results for $^{106, 108}$Cd and predicts a minimum in $\left|Q_{2^+}\right|$ at ^{112}Cd. The second calculation, however, agrees better with the recent values reported by Hall et al. and predicts a steady increase in $\left|Q_{2^+}\right|$ from ^{108}Cd to ^{116}Cd.

The present investigation was undertaken in an effort to resolve the above-mentioned conflicts in the experimental results for Q_{2^+} in the cadmium isotopes. It was further hoped that a distinction
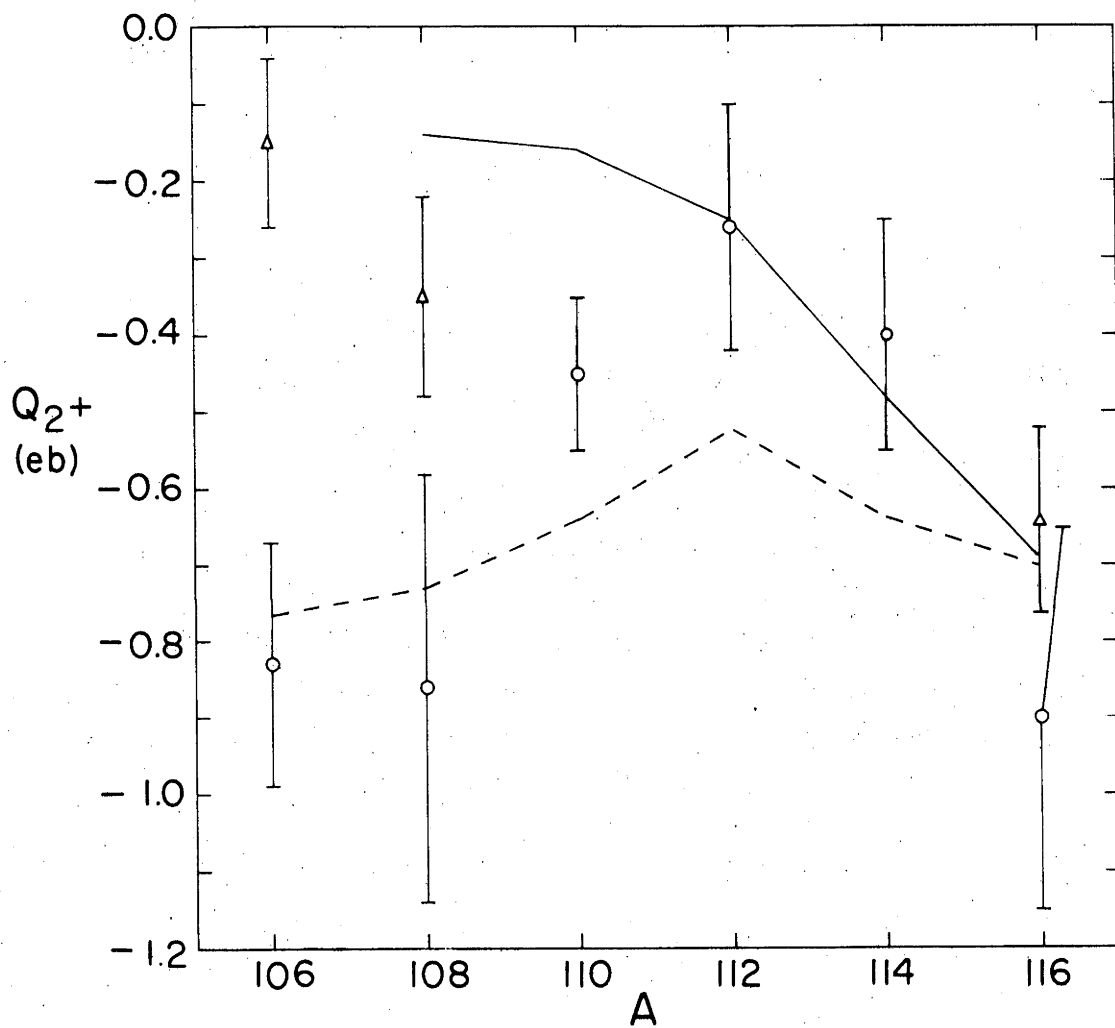
Figure 1.3. Summary of the previous results for Q_{2+} in the cadmium isotopes. The experimental points are taken from the survey of Christy and Häusser (Ch 72) (open circles) and the recent work of Hall et al. (Ha 74, Ha 75) (triangles). The theoretical calculations are by Sorensen (So 73) (dashed line) and Sips (Si 71) (full line).

could be made between the various theoretical models: for example, the two calculations shown in figure 1.3 (which predict divergent trends for the lower mass Cd isotopes) and several other calculations for the frequently studied isotope ^{114}Cd (see chapter 5). In particular the particle-vibration coupling model of Alaga (Al 67) has had some success in explaining many properties of the low-lying states of nuclei in the mass A=100 region. For ^{114}Cd this model predicts Q_{2^+} = -0.33 e.b which is in good agreement with the currently accepted value of about -0.4 e.b (Kl 75).

1.6 Experimental Methods for Determining Excited State Quadrupole Moments

The systematic trends observed in ground state quadrupole moments, e.g. the occurrence of relatively large values in well-defined mass regions (section 1.2), has stimulated the development of collective nuclear models. Further important advances may be expected to follow from the measurement of excited state quadrupole moments with improvements both in quality and quantity of experimental data.

The measured quadrupole moments in even-even nuclei at present are largely restricted to first excited 2^+ states. The quadrupole moments of higher states, for example the second 2^+ state in vibrational nuclei, have not as yet been measured with model independent methods. There is no general agreement as to the magnitude or sign of $Q_{2^{+'}}$; the sensitivity and accuracy of the present methods used are inadequate for such measure-ments.

A brief description of various methods which can be used to measure excited state quadrupole moments is given below with references to more detailed treatments.

a)   The Mössbauer Method

The strongest laboratory produced external electric field
gradients are several orders of magnitude too small to produce a detectable
quadrupole interaction energy.   In crystalline solids a nucleus situated at
a lattice point is subject to strong local electric and magnetic fields.
In crystals with a cubic lattice structure the electric field gradient is
zero.   If the structure has lower symmetry, for example tetragonal or
hexagonal, the field gradient is axially symmetric and non-zero.   Field
gradients as large as $10^{18}V/cm^2$ can be obtained in suitable crystals.   The
charge distribution of a nucleus embedded in such a crystal and excited
through resonant γ-ray absorption will interact with the field gradient
causing a splitting in the magnetic substates of the nuclear levels
participating in the excitation provided at least one has a spin ≥ 1.   The
splitting due to the quadrupole interaction is of the order of 10^{-6}-$10^{-7}eV$
and can be larger than the natural linewidths of the γ-rays ($\sim 10^{-8}eV$).   It
is possible to detect the individual transitions between the substates of
the two levels using the Mössbauer effect if the γ-ray energies involved
are <200keV.   The usual procedure consists of preparing a source nucleus
in a cubic crystal lattice which has zero electric field gradient (unsplit
source).   The absorber (containing nuclei of the same kind) is then
prepared in a lattice with lower symmetry.   The resonant absorption of
γ-rays due to various transitions can be observed when the source is in
relative motion with respect to the absorber and the product QV_z extracted
from the relative positions of the absorption peaks.   The source has to be
prepared in a crystal lattice and kept at low temperature such that an
appreciable fraction of the γ-rays are emitted without recoil or excitation
of the crystal lattice.   This limits the applicability of the method to
nuclei which have low-lying excited states E<200keV; for example the first
2^+ states in deformed rotational nuclei.   If the ground state and the

excited state both have spins $\geqslant 1$ only the difference between the quadrupole moments of the two states can be measured. Determination of Q relies on the knowledge of the EFG in the crystal. Theoretical estimates of this quantity, however, are not very reliable at present (Bo 75). The Mössbauer method, on the other hand, can be used to obtain highly accurate ratios of Q for different isotopes.

b) Perturbed Angular Correlations

The angular correlation of gamma-rays emitted from radioactive nuclei embedded into single- or poly-crystalline compounds or metals is perturbed due to the interaction of the quadrupole moment with the EFG. For nuclear states with lifetimes longer than 10^{-9} sec. the perturbation can be observed experimentally and the magnitude of the associated frequency $|w_Q|$ (equation 1.5) determined. There are two basic methods:

1) The source is prepared in a single crystal and the angular correlation (or distribution) of γ-rays determined as a function of the crystal symmetry axis. The effect of the quadrupole interaction is observed as an attenuation of the angular correlation and depends on $|w_Q \tau|$, where τ is the lifetime of the state.

2) The source is prepared in a single- or poly-crystalline material and the angular correlation (or distribution) is determined as a function of time (differential method).

Due to the M^2 degeneracy (equation 1.4) an aligned EFG has to be applied to polarized nuclei in order to determine the sign of w_Q and thus the sign of Q. This can be achieved in several ways:

i)   By determining the polarization of the deexcitation γ-rays (Be 62).

ii)   Through β-γ angular correlations (Ra 73).

iii) By polarizing the initial state (Gr 71).

The latter condition can be satisfied by recoil implanting excited nuclei into a suitable environment following Coulomb excitation or a nuclear reaction. For example the (d,p) reaction (Bl 72) has recently been used for this purpose, demonstrating the possibility of in-beam experiments. Isomeric states are particularly suitable candidates for study by this method. However, if time-integrated perturbations are observed states with lifetimes in the sub-nano second region can be studied.

A major drawback of all of the above methods is that they require a knowledge of the EFG in crystalline materials. Uncertainties in calculated electric field gradients can be larger than 30%. In some cases the EFG can be calibrated; for example, by comparison with a Mössbauer measurement. A further difficulty arises in the recoil implantation method (He 71); recoil implantation of excited and ionized nuclei can produce non-axial and fluctuating EFG's through damage and defects created by heavy recoiling ions in crystals. The effects of these additional electric fields have been observed as an attenuation in the quadrupole interaction. The damping is temperature dependent and diminishes at high temperatures near the melting point where crystal damage due to recoil is expected to be minimal (He 74).

c) Muonic X-rays

The hyperfine splitting observed in muonic atoms is due to the interaction of the nuclear dipole and quadrupole moments with the bound muon in an electronic orbit (De 69). The muonic orbits are $m_\mu/m_e \sim 200$ times closer to the nucleus than the corresponding electronic orbits. The muon in fact spends about 50% of its time inside the nuclear volume when in an $s_{\frac{1}{2}}$ orbit. In high Z nuclei the muon has several MeV of energy and mixing of nuclear and muonic states occurs. Even-even nuclei with 0^+ ground states can produce hyperfine splitting through excitation to

higher states in this way. The hyperfine splitting ($\propto QZ^3$) of the muonic

X-rays can be resolved in Ge(Li) detectors and Q determined by assuming a

given shape for the radial nuclear charge distribution. The method,

therefore, is somewhat model dependent. The effect is enhanced in heavy

nuclei due to the Z^3 dependence. In light nuclei the splitting is too

small to be detected with present Ge(Li) detectors. Magnetic dipole

splitting is also present but it is a factor of 200 smaller than the

quadrupole splitting.

d) Inelastic Scattering

It is possible to relate the cross-sections for inelastic

scattering of protons, deuterons and alpha particles to a set of nuclear

surface deformation parameters β_λ (Ta 65) defined by

$$R = R_0 \left(1 + \beta_2 Y_{20} + \beta_4 Y_{40} + \ldots \right) \tag{1.12}$$

where R is the radius parameter for the deformed optical potential used in

the analysis. The deformation parameters, in turn, are related to the

intrinsic quadrupole moment (equation 1.9) by

$$Q_0 = \frac{3}{\sqrt{(5\pi)}} ZR_0^2 (\beta_2 + 0.36\beta_2^2 + 0.33\beta_4^2 + 0.97\beta_2 \beta_4) \tag{1.13}$$

Similar information can be obtained from inelastic electron

scattering experiments (Li 72). The results of recent electron scattering

measurements in cadmium isotopes (Gi 76) both for B(E2, $0^+ \to 2^+$) and Q_{2^+} are in

agreement with those obtained from Coulomb excitation experiments and will

be discussed in chapters 4 and 5.

e) Coulomb Excitation

A projectile with charge $Z_1 e$ impinging on a target nucleus

produces a time dependent electric field gradient of extremely short

duration ($\sim 10^{-20}$ sec.). The magnitude of the field gradient, assuming

a point charge distribution for the projectile, is given by $V_Z = Z_1 e/4\pi\epsilon_0 d^3$,

and can be greater than 10^{30}V/cm^2. Here d is the closest distance of

approach and for a given bombarding energy occurs in a head-on collision.

The bombarding energy is chosen such that the dominant interaction is

through the Coulomb field with negligible contribution from nuclear forces.

Under these conditions, and in contrast to EFG's in crystals, the field

gradients in Coulomb excitation can be calculated exactly, with no model

dependent assumptions.

The time dependent EFG can excite the low-lying nuclear levels

and intereact with the quadrupole moment of an excited state causing a

redistribution in the magnetic substate populations, that is a reorien-

tation of the nuclear spin axis. This precession can be detected in the

angular distribution of the subsequent γ-rays (Gr 73) and is called the

reorientation effect. The term is somewhat misleading in that no change

in the magnetic-substate populations can occur during a head-on collision

whereas the quadrupole moment effect (i.e. the time dependent hyperfine

splitting of the excited state) is a maximum (since V_Z is a maximum for

180° scattering). For example, if 40MeV ^{16}O projectiles scattered from

^{114}Cd are observed close to 180°, the quadrupole interaction can be

detected as a decrease of about 7% in the 2$^+$ state cross section. At

90°, however, the change in cross section is only about 3%.

The reorientation method has been applied to the measurement

of the quadrupole moments of the first excited 2$^+$ states in stable even-

even nuclei from ^{18}O to ^{206}Pb. A compilation of these moments has been

given by Christy et al. (Ch 72). In principle the quadrupole moments of

all states that are Coulomb excited can be measured. However, Coulomb

excitation cross-sections drop rapidly with increasing excitation energy and there are, usually, additional effects of similar magnitude competing with the reorientation process (Hä 74).

In the present work the reorientation effect has been used to measure the quadrupole moments of the first excited 2^+ states in the stable cadmium isotopes. Aspects of the Coulomb excitation mechanism relevant to quadrupole moment measurements will be outlined in chapter 2, together with a comparative description of various experimental methods exploiting the reorientation effect.

CHAPTER 2.

SEMICLASSICAL COULOMB EXCITATION THEORY

The theory of Coulomb excitation and the associated experimental methods have been extensively discussed in review articles; most recently by de Boer and Eichler (de Bo 68), McGowan and Stelson (McGo 74), Häusser (Hä 74) and Newton (Ne 75). A detailed theoretical treatment and additional references can be found in the book of Alder and Winther (Al 75). The Coulomb excitation mechanism can best be illustrated through a perturbation theory approach which provides a convenient classification for various effects. For example, the first order term describes a single step excitation process, whereas multiple excitation through intermediate states and a dependence on quadrupole moment arise in the second order. In this chapter a qualitative description of the Coulomb excitation theory will be given with emphasis on aspects relevant to the extraction of quadrupole moments from experimental data.

2.1 Bombarding Energies

The main feature of Coulomb excitation which distinguishes it from other types of nuclear excitation is the absence of effects due to the nuclear interaction (electron scattering is another example, in which the electron interacts with nucleons through the electromagnetic field). Excitation via electromagnetic forces is well understood and exact calculations are possible. Any interference from nuclear forces on the other hand would require assumptions dependent on various models of the nuclear force. If a collision between a projectile of mass A_1 and charge Z_1 with a target nucleus of mass A_2 and charge Z_2 occurs at sufficiently low bombarding energy, the long range repulsive Coulomb field ensures that the projectile does not enter the region of the short range nuclear force.

The closest distance of approach (2a) corresponds to a head-on collision; the separation S between the surfaces of the two nuclei can then be expressed as

$$2a = 2Z_1 Z_2 e^2/(m_0 v^2) = r_0 (A_1^{1/3} + A_2^{1/3}) + S \quad , \qquad (2.1)$$

where r_0 is usually taken to be 1.25 fm, $m_0 = A_1 A_2/(A_1 + A_2)$ is the reduced mass, v is the velocity of the projectile in the centre of mass system, and e the electronic charge. For example no nuclear effects (<0.5%) are observed when 10MeV ^{4}He or 44MeV ^{16}O projectiles are scattered from ^{112}Cd. In this case a = 7.2 fm and S = 5-6 fm for both projectiles. The range of the nuclear force is about 2 fm; roughly three times this distance is required between the surfaces of the target and the projectile because of the quantal nature of the orbit. The projectile is not completely localized but moves in a smeared out wave packet characterized by wavelength λ. In the above example λ = 4.5 fm for the ^{4}He projectile and 1 fm for ^{16}O. The quantal non-penetration requirement can be expressed qualitatively through the Sommerfeld parameter η defined as

$$\eta = \frac{a}{\lambdabar} = \frac{Z_1 Z_2 e^2}{\hbar v} \quad . \qquad (2.2)$$

The projectile is considered to move in a well localized classical Rutherford orbit if the orbit parameter a is much larger than the extent of the wave packet, i.e.

$$\eta \gg 1 \qquad (2.3)$$

It is apparent that quantal effects will be more important for the ^{4}He projectile ($\eta \sim 10$) than for ^{16}O ($\eta \sim 37$).

2.2   Qualitative Description of the Excitation Process

As the projectile sweeps past the target it is accelerated and

gives rise to a pulsed electromagnetic (E-M) field. The mediator of the E-M field is the photon and the force field can be pictured to arise from a continuous exchange of virtual photons. If one or more of these are absorbed by the target during the collision, the nucleus will be excited to a higher energy state. The projectile will lose energy and the orbit of the scattered particle will differ from the initial orbit. It is not clear, however, at which point along the classical Rutherford orbit the energy exchange occurs and therefore the change in the orbit cannot be calculated in a purely classical treatment. This change is small if the energy transferred in exciting a level n, ΔE_n, is small compared to the projectile kinetic energy, i.e.

$$\Delta E_n/E \ll 1 \quad . \tag{2.4}$$

Another useful picture of the Coulomb excitation process arises from the consideration of possible distortions in nuclear shapes. During a collision the repulsive Coulomb field can distort the shape of spherical nuclei and give rise to surface oscillations. These will be quantized and, for example, quadrupole, octupole and hexadecapole transitions are observed implying a dynamic deformation of nuclei into these shapes during the collision. In permanently deformed nuclei the Coulomb field will induce a rotation in transferring energy and the low-lying rotational states will be excited.

The remainder of the discussion will be limited to target excitation. The possible simultaneous excitation of both the target and the projectile will be ignored. This is a very good approximation for the case which will be used as an example, i.e. the scattering of ^{4}He and ^{16}O projectiles from ^{112}Cd. In addition the emphasis will be on the situation where scattered particles are detected, rather than the gamma rays from the decay of excited states.

The first excited state of ^{112}Cd is at 0.617MeV; the natural oscillation period associated with this state (assuming a vibrational type excitation mode) is $T = h/\Delta E_n = 6.7 \times 10^{-21}$ sec. In comparison, the collision period τ can be defined as the time required for the projectile to traverse a distance a

$$\tau(\theta) = \frac{a(\theta)}{v} = \frac{a}{2v} (1 + 1/\sin \frac{\theta}{2}) \quad . \quad (2.5)$$

Here θ is the centre of mass scattering angle and the particular dependence on θ arises from a consideration of the geometry of the Rutherford orbit (Al 75). In a head-on collision with a = 7 fm,

$$\tau = \frac{a}{v} = 3 \times 10^{-22} \text{ sec.} \quad , \quad (2.6)$$

for both ^{4}He and ^{16}O projectiles. Therefore, $\tau_{coll} \ll T_{nuc}$, which is an essential condition if energy is to be transferred to the target from the projectile. Classically a similar situation arises in compressing a spring with one end mounted on a rigid support and the other free. If the spring is compressed and then released slowly only a small amount of energy can be transferred to it (adiabatic process). If, however, the compressive force is an impulse of short duration, the spring will oscillate for some time after the encounter. The condition for non-adiabatic excitation is expressed through the "adiabaticity parameter" ξ defined as

$$\xi = \tau_{coll} \, \Delta E_n/\hbar \quad , \quad (2.7)$$

where $\Delta E_n/\hbar$ is the nuclear frequency corresponding to the excited level n. Appreciable excitation from the ground state to state n is possible only if $\xi \lesssim 1$. It can be shown that the excitation probability decreases as $\exp(-2\pi\xi)$ when $\xi > 1$ (Al 75).

In an adiabatic collision dynamic deformation of the nucleus may occur, but as in the case of the spring energy transfer is impeded.

Nevertheless, such a process may interfere with other modes of excitation. During a collision the Coulomb repulsion acts on the protons. The resulting relative displacement of the neutron and proton fluids in the nucleus is responsible for the excitation of the giant dipole resonance-GDR (Ei 70). In ^{112}Cd the GDR is observed at 16.3MeV excitation (Ar 70), corresponding to a period of oscillation of 2.5 x 10^{-22} sec., which is comparable to the collision time τ_{coll}. Therefore the GDR can only be excited adiabatically. However, as discussed below and in chapter 4, it may participate as an intermediate virtual state in the excitation of another level, giving rise to a small change in the excitation probability.

2.3   Outline of First Order Theory

Apart from kinematic parameters, such as η and ξ, the excitation probability depends on the matrix elements of the interaction Hamiltonian H(t) between the initial state $|i>$ and final state $|f>$. The initial state, in Coulomb excitation, is always the ground state. In general H(t) will contain terms describing the electric multipole-multipole interaction between the target and the projectile, the magnetic multipole-multipole interaction and an interaction between the electric and magnetic multipole moments of the system. As stated earlier, the multipole moments of the projectile electric charge distribution will be neglected. The projectile will be considered as a point charge with mass A_1 interacting with the target only through the monopole term. Furthermore, the magnetic excitation will be ignored. The largest terms of this type arise from the interaction between the electric monopole moment of the projectile and the magnetic multipole moments of the target. They are proportional to the relative motion between the projectile and the target and scale as v/c (Al 75). They contribute to the excitation probability as $(v/c)^2$ (about 0.006 in the case of ^{112}Cd). With these assumptions the electric

interaction can be written as,

$$H_E(t) = \int \frac{\rho(\underline{r})Z_1 e}{|\underline{r}-\underline{r}_p(t)|} \, d\tau \quad , \qquad (2.8)$$

where $\underline{r}$ is the radius vector for a volume element $d\tau$ in the target with charge density $\rho(\underline{r})$, and $\underline{r}_p(t)$ is the time dependent vector describing the separation of the target and projectile. Because of the non-penetration situation $\underline{r}_p \gg \underline{r}$ and $|\underline{r}-\underline{r}_p(t)|^{-1}$ can be expanded in powers of r/r_p in the usual multipole expansion. The result is

$$H_E(t) = 4\pi Z_1 e \sum_{\lambda\mu} \frac{1}{(2\lambda+1)} \left(\int Y^*_{\lambda\mu}(\underline{r}) r^\lambda \rho(\underline{r}) d\tau \right) \left(r_p^{-\lambda-1} Y_{\lambda\mu}(\underline{r}_p) \right) , \quad (2.9)$$

with λ ranging from 0 to ∞ and μ from $-\lambda$ to $+\lambda$. The first term in the expansion ($\mu=\lambda=0$) represents the monopole-monopole interaction and does not give rise to any excitation. It determines the relative motion of the two particles - the Rutherford orbit:

$$H_{(\lambda=0,\mu=0)} = \int \frac{Z_1 e\rho(r)}{r_p(t)} \, d\tau \quad . \qquad (2.10)$$

H_E can be expressed in terms of the electric multipole moments $M(E\lambda,\mu)$ of the target defined as

$$M(E\lambda,\mu) = \int \rho(\underline{r}) r^\lambda Y_{\lambda\mu}(\underline{r}) \, d\tau \qquad (2.11)$$

for multipole order λ; they have the property

$$M(E\lambda,-\mu)(-1)^\mu = M(E\lambda,\mu)^* \quad . \qquad (2.12)$$

The left-hand side of equation (2.12) is then identical with the terms in the first bracket of equation (2.9).

The differential cross-section for exciting the state $|f\rangle$ from the initial state $|i\rangle$ is proportional to the Rutherford cross-section and can be expressed in terms of an excitation probability $P_{if}(\theta)$

$$\left.\frac{d\sigma}{d\Omega}\right)_f = \left.\frac{d\sigma}{d\Omega}\right)_{Ruth} \times P_{if}(\theta) \tag{2.13}$$

$$= \frac{1}{4} a^2 \sin^{-4}(\theta/2) \times P_{if}(\theta) \qquad . \tag{2.14}$$

The excitation probability can be expressed in terms of the excitation amplitudes b_{if}. If the initial state is unpolarized, a summation over the final magnetic sub-states and an average over the initial magnetic sub-states is required:

$$P_{if} = (2J_i+1)^{-1} \sum_{M_i M_f} |b_{if}|^2 \qquad . \tag{2.15}$$

In the first order perturbation theory approximation, the first order excitation amplitude $b_{if}^{(1)}$ is given by (Me 62)

$$b_{if}^{(1)} = (i\hbar)^{-1} \int_{-\infty}^{+\infty} <J_f M_f | H_E(t) | J_i M_i > \exp(i\omega_{fi}t) \, dt \quad , \tag{2.16}$$

where $\omega_{fi} = (E_f - E_i)/\hbar$, E_f is the excited state energy and E_i the ground state energy ($=0$). The matrix element in equation (2.16) represents the strength of the interaction, with H_E given by equation (2.9). Using equations (2.9), (2.11) and (2.12), that part of the matrix element which depends on the nuclear properties of the target can be separated from the time dependent orbital parameters. The nuclear part reduces to

$$<J_i M_i | M(E\lambda,\mu) | J_f M_f > = (-1)^{J_i - M_i} \begin{pmatrix} J_i & \lambda & J_f \\ -M_i & \mu & M_f \end{pmatrix} M_{fi}^{(\lambda)} \quad , \tag{2.17}$$

where $M_{fi}^{(\lambda)}$ is the reduced matrix element given by

$$M_{fi}^{(\lambda)} = <I_i \| M(E\lambda) \| I_f > \quad , \tag{2.18}$$

and the quantity in brackets is a 3j symbol. The excitation probability (2.15) can then be expressed in terms of the reduced matrix element and an integral over the time dependent projectile coordinates:

$$P_{if}(\theta) = \sum_{\lambda} |\chi_{i \to f}^{(\lambda)}|^2 \sum_{\mu} |R_{\lambda\mu}(\theta,\xi)|^2 \quad . \tag{2.19}$$

It is the second term in equation (2.19) which describes the properties of the orbit and is called the orbital integral. The quantities $R_{\lambda\mu}(\theta,\xi)$ have been tabulated by Alder and Winther (Al 75) for a range of values of λ,μ,θ and ξ. The nuclear matrix element is contained in $\chi^{(\lambda)}$:

$$\chi_{i\rightarrow f}^{(\lambda)} = \frac{\sqrt{16\pi} \ (\lambda-1)!}{(2\lambda+1)!!} \ \frac{Z_1 e}{\hbar v} \ \frac{<J_i \| M(E\lambda) \| J_f>}{a^\lambda (2J_i+1)^{\frac{1}{2}}} \quad , \qquad (2.20)$$

and is an indicator of the interaction strength for a transfer of angular momentum $\lambda\hbar$ and z-component $-\mu\hbar$ subject to selection rules:

$$|J_i - J_f| < \lambda < |J_i + J_f|$$

$$(2.21)$$

$$- M_i + M_f = - \mu \quad .$$

An interesting interpretation of $\chi^{(\lambda)}$ arises (Al 75) from the photon emission-absorption description of the Coulomb field. In this picture $\chi^{(\lambda)}$ represents the number of photons (in the statistical sense) transferred during the collision from the E-M field to the target.

In figure 2.1 $\chi_{0^+\rightarrow 2^+}^{(2)}$ is plotted for ^{4}He and ^{16}O projectiles scattered from ^{112}Cd as a function of projectile energy. The energy dependence of $\chi^{(\lambda)}$ for $\lambda=2$ is proportional to $E^{3/2}$.

Having determined P_{if} the differential excitation cross-section can be calculated using equation (2.14). The interaction strength and the various other related formulae are usually expressed in terms of the reduced transition probability $B(E\lambda)$, for multipole order $E\lambda$, defined as

$$B(E\lambda;J_i\rightarrow J_f) = (2J_i+1)^{-1}|<J_i \| M(E\lambda) \| J_f>|^2 \quad . \qquad (2.22)$$

So far the excitation probability has been described in terms of first order perturbation theory as a single step (i$\rightarrow$f) process dependent on the reduced transition probability and geometric components
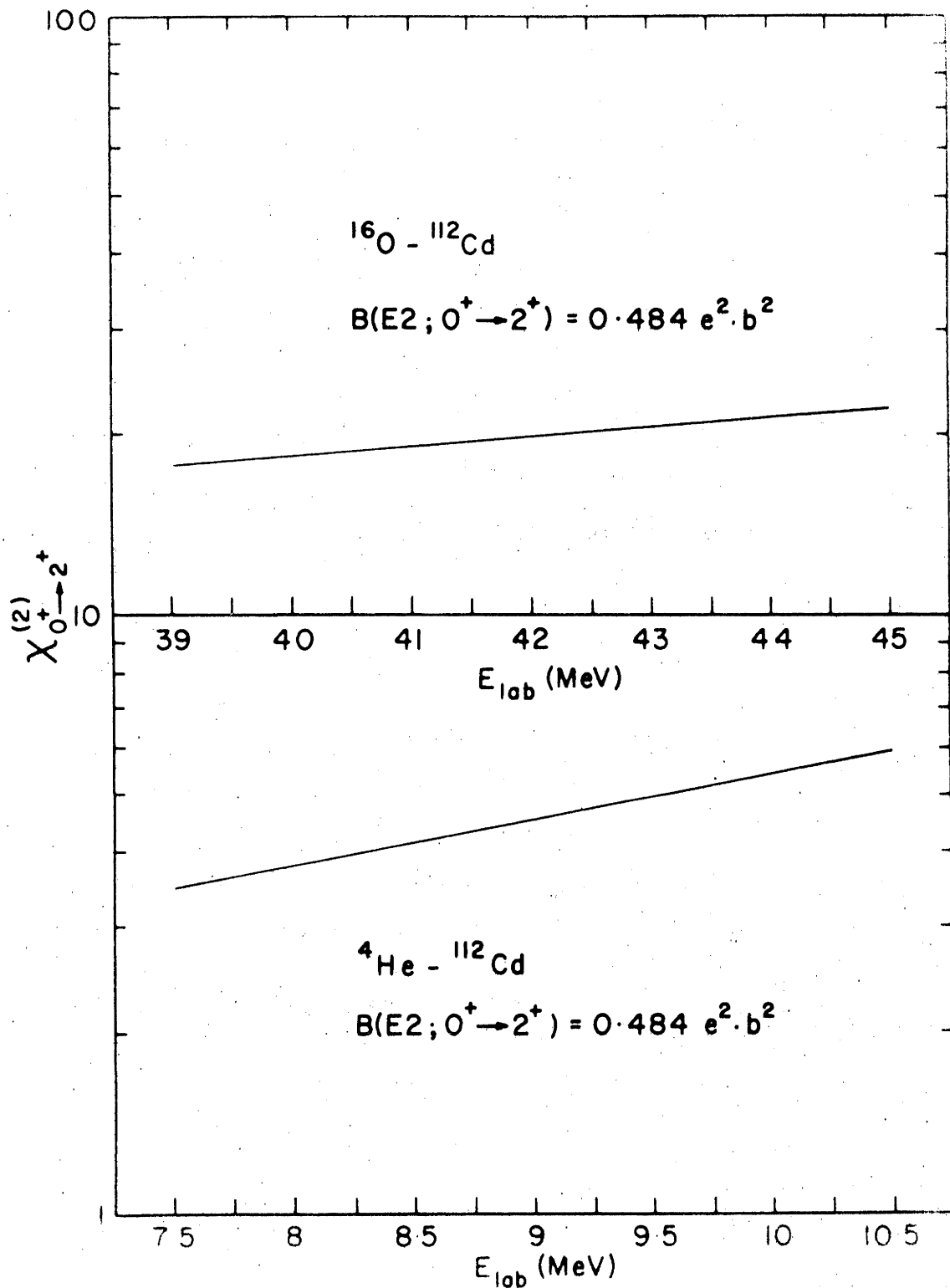
Figure 2.1. The interaction strength $\chi^{(2)}_{0^+\to 2^+}$ for ^{4}He and ^{16}O projectiles backscattered from ^{112}Cd. The energy ranges shown correspond to those used in the present work.

describing the orbit (the orbital integral). If, however, the parameters $\chi^{(\lambda)}$ become larger than or comparable to unity, as in heavy ion bombardment with ^{16}O, ^{32}S, ^{40}Ar, ... , projectiles, higher order processes such as multiple excitation can occur. The dependence of excitation probability on quadrupole moment arises in the second order perturbation treatment and will be briefly outlined below.

2.4 Higher Order Perturbation Theory

As can be seen from equation (2.19) the first order excitation probability depends on $|\chi_{i \to f}^{(\lambda)}|^2$. In a higher order perturbation expansion the excitation probability will not only contain second, third, ... etc., order terms but also terms arising from interference between first order and second order amplitudes; between first order and third order amplitudes; ... etc. The perturbation expansion in terms of χ's will then be of the form

$$P_{i \to f} = c_2 \chi^2 + c_3 \chi^3 + c_4 \chi^4 + \dots \quad , \qquad (2.23)$$

where c's depend on the orbit parameters. The lowest order term, beyond first order, is $c_3 \chi^3$, the interference term between the first and second order processes. It is instructive to consider pictorially the various types of excitation that can give rise to interference between the first and second order processes. Some of these are shown in figure 2.2 for a nucleus with 0^+ ground state labelled i, 2^+ first excited state f, and an additional higher energy 2^+ state n. The magnetic substates of the first 2^+ state are also shown. In terms of excitation amplitudes, $b_{if}^{(1)}$ represents the first order term. In second order it is possible to populate state f through n with corresponding amplitudes $b_{inf}^{(2)}$. Another possibility is a rearrangement in the magnetic substate populations of level f, $b_{if'f}^{(2)}$. The total amplitude is the sum of all such terms,
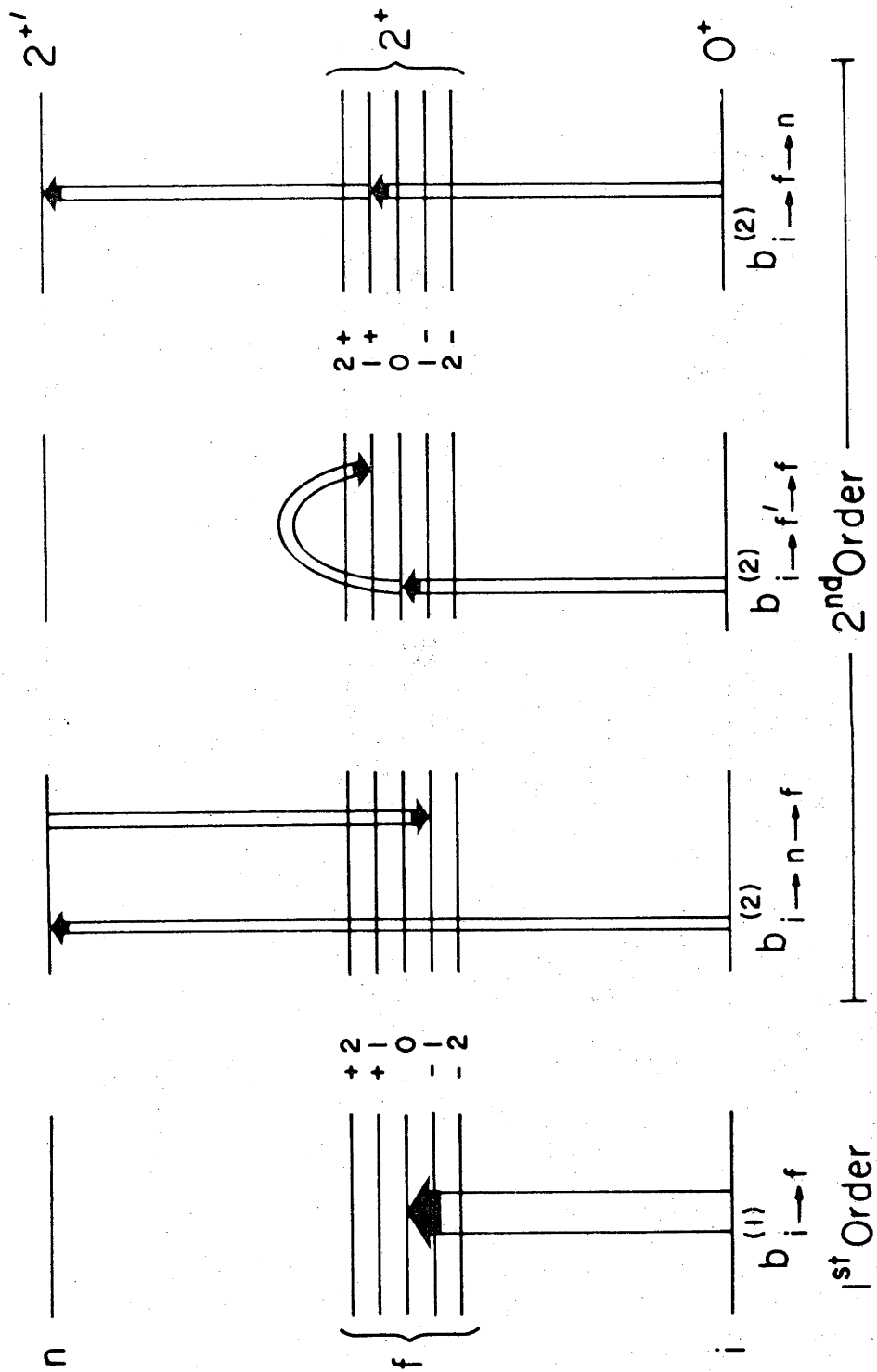
Figure 2.2.   Schematic representation of first and second order excitation processes in a nucleus with three energy levels 0^+, 2^+, $2^{+'}$.

$$b_{if} = b_{if}^{(1)} + b_{if'f}^{(2)} + b_{inf}^{(2)} + \ldots \quad , \qquad (2.24)$$

and the excitation probability up to the second term in equation (2.23) can be written as

$$P_{if} = c_2'|b_{if}^{(1)}|^2 + c_3'(b_{if}^{(1)}b_{if'f}^{(2)} + b_{if}^{(1)}b_{inf}^{(2)} + \ldots) + \ldots, (2.25)$$

where the c' again depend on orbital parameters.

In analogy with equation (2.16) the second order excitation amplitude, for an intermediate state n, is given by (Me 62)

$$b_{inf}^{(2)} = (i\hbar)^{-2}\int_{-\infty}^{+\infty} dt<f|H_E(t)|n>e^{i\omega_{fn}t}\int_{-\infty}^{t} dt'<n|H_E(t')|i>e^{i\omega_{ni}t'} \quad . \quad (2.26)$$

As in the case of the first order theory the excitation probability P_{if}, in second order, can be separated into a geometric part, this time involving the evaluation of a double integral, and a part dependent on the matrix elements connecting the initial-intermediate-final states.

In some circumstances direct excitation may have to take place through a higher multipole order; for example, direct excitation of a 4^+ level from a 0^+ ground state. Then the first order term will be small, and significant double excitation may take place through another state such as an intermediate 2^+ level.

The reorientation effect, which is of interest here, arises from the interference between first and second order terms when the intermediate state is identical with either the initial or the final state (provided one or both have spins $>\frac{1}{2}$). In the specific case of 0^+ ground state and 2^+ excited state this occurs if f=f' in equation (2.25) and figure 2.2. It also implies a dependence on a matrix element of the type $<f|H_E(t)|f>$. Now, the usual definition of the static quadrupole moment Q is (see chapter 1, equation 1.3)

$$eQ = e<JJ|\sqrt{\frac{16\pi}{5}}\ r^2 Y_{20}(\theta,\xi)|JJ> \tag{2.27}$$

$$= \sqrt{\frac{16\pi}{5}}\ e \begin{pmatrix} J & 2 & J \\ -J & 0 & J \end{pmatrix} <J\| r^2 Y_{20}\| J> \quad,$$

or in terms of the reduced matrix elements

$$M_{if}^{(\lambda)} = <J_f\| r^\lambda Y_{\lambda 0}\| J_i> \quad,$$

$$Q = \sqrt{\frac{16\pi}{5}}\ (\ \frac{J(2J-1)}{(J+1)(2J+1)(2J+3)}\ )^{\frac{1}{2}}\ M_{JJ}^{(2)} \quad. \tag{2.28}$$

Considering only the first two terms in equation (2.25), the excitation probability for the 2^+ state can be written as

$$P_{0^+\to 2^+} = |\chi_{0\to 2}^{(2)}|^2 R_2^2(\theta,\xi)\left(1 + \chi_{2\to 2}^{(2)}\ c(\theta,\xi)\right) \quad, \tag{2.29}$$

where $R_2(\theta,\xi) = \sum_\mu |R_{2\mu}(\theta,\xi)|^2$ as in equation (2.19) and $c(\theta,\xi)$ have been tabulated by Alder and Winther (Al 75). From equation (2.20) we see that

$$\chi_{2\to 2}^{(2)} = \frac{4}{15}\sqrt{\frac{\pi}{5}}\ \frac{Z_1 e}{\hbar v}\ \frac{1}{a^2}\ <2\| M(E2)\| 2> \tag{2.30}$$

$$= \sqrt{\frac{7}{90}}\ \frac{Z_1 e}{\hbar v a^2}\ Q_{2^+} \quad.$$

Over a restricted energy interval, $c(\theta,\xi)$ is approximately proportional to ξ, and P_{2^+} can be expressed in a more convenient and often used form as

$$P_{0^+\to 2^+} = P_{0^+\to 2^+}^{1st}\ \left(1+1.32\ \frac{A_1}{1+A_1/A_2}\ \Delta E_{0^+\to 2^+}\ \frac{K(\theta,\xi)}{Z_2}\ Q_{2^+}\right) \quad, \tag{2.31}$$

where $P_{0^+\to 2^+}^{1st}$ is the first order excitation probability, given by

$$P_{0^+\to 2^+}^{1st} = B(E2;\ 0^+\to 2^+)F(\theta,\xi) \quad. \tag{2.32}$$

The excitation energy $\Delta E_{0^+\to 2^+}$ of the 2^+ state is in MeV, θ is the centre of mass scattering angle, Q_{2^+} is given in e.b and $B(E2;\ 0^+\to 2^+)$ in $e^2.b^2$. The quantity $F(\theta,\xi)$ is related to the orbital integral through equations (2.19), (2.20) and (2.22), and K is proportional to c/ξ.

The second term in equation (2.31) is only one of a number of similar terms which may contribute to the excitation probability of the 2^+ state. Another significant term arises when the intermediate state n is a higher energy second 2^+ state (fig. 2.2); in vibrational type nuclei this is usually the 2^+ member of the two phonon triplet. The amplitude of this interference term is

$$ b^{(1)}_{0^+ \to 2^+} \ b^{(2)}_{0^+ \to 2^{+\prime} \to 2^+} \quad , \tag{2.33} $$

and in the case of the Cd isotopes it is the largest second order contributor, after the quadrupole moment term, to the excitation probability of the first 2^+ state. In quadrupole moment measurements through Coulomb excitation, it is important, therefore, to know the matrix elements involved in equation (2.33). The effect of this term will be discussed in more detail in chapter 4.

A similar type of term arises in the virtual excitation of the GDR. As mentioned earlier the GDR can only be excited adiabatically. However, as an intermediate participant, it may contribute to the excitation of the 2^+ state appreciably. This type of excitation can be treated as a polarization effect and will also be discussed in chapter 4.

The outline of Coulomb excitation theory given above is referred to as being semiclassical. This arises because the actual trajectory of the projectile differs from the classical Rutherford orbit due to the transfer of energy to the target. For example, the velocity before the collision, v_i, will differ from the velocity after the collision, v_f. This is not a big effect provided ($\eta \gg 1$) and the energy transferred is a small fraction of the projectile kinetic energy. The semiclassical equations can be improved through an averaging procedure called symmetrization. It involves replacing v_i by $\sqrt{(v_i v_f)}$, and similar recipes apply

for other parameters of the theory. Differences still exist, however, and they can only be corrected by comparing the symmetrized semiclassical results with those of a full quantal calculation (see chapter 4).

Equation (2.31) was derived by using a perturbation expansion and it only contains the first two leading terms. Nevertheless, it provides a valuable guide in evaluating the sensitivity of the quadrupole moment effect to variations in the various parameters. Furthermore, $F(\theta,\xi)$ and $K(\theta,\xi)$ can be calculated - including the effects of higher states and all orders of perturbation - with the de Boer-Winther semiclassical computer code (Wi 66) which solves the Schrödinger equation numerically. Equation (2.31) can then be used to parametrize the excitation probability over the energy region employed in an experiment (see section 4.6).

2.5 Theoretical Basis of Reorientation Effect Experiments

In this section equation (2.31) will be used to discuss the relative merits of the various experimental methods employed in measuring quadrupole moments via the reorientation effect. The discussion will be restricted to even-even nuclei around the mass A=100 region where most reorientation measurements have been concentrated. The second term on the right hand side of equation (2.31) determines the sensitivity of the measured cross sections to Q_{2+}. The properties of this term influence the choice of experimental conditions which will maximize the effect:

a) It is approximately linear in the projectile mass A_1 and linear in Q_{2+}. Both the magnitude and the sign of Q_{2+} can, therefore, be determined.

b) Both of the functions $F(\theta,\xi)$ and $K(\theta,\xi)$ vary monotonically with energy. This variation is shown in figure 2.3 for ^{4}He and ^{16}O ions scattered from ^{112}Cd over the relevant energy region. In practice the 'usable' energy region is restricted by considerations of barrier penetration
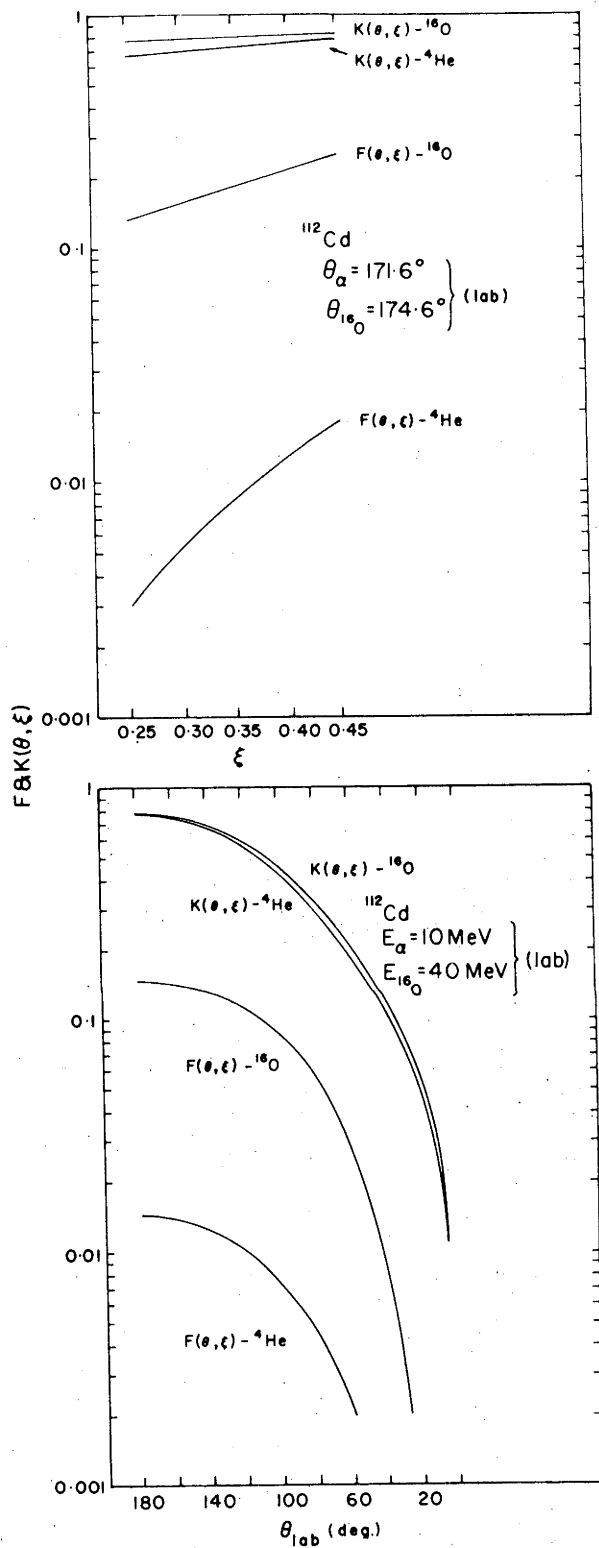
Figure 2.3. Dependence of $F(\theta,\xi)$ and $K(\theta,\xi)$ on
ξ and scattering angle for ^{4}He and
^{16}O projectiles scattered from ^{112}Cd.

and interference from nuclear reactions at the higher energies, and
the rapid drop-off in excitation probability at the lower bombarding
energies.

c)   In figure 2.3 the dependence of $F(\theta,\xi)$ and $K(\theta,\xi)$ on scattering angle
     θ_{lab} is shown. They both have their maximum values at 180° and vary
     strongly with θ, falling off to zero at forward angles.

d)   There are two unknowns in the reorientation term, $B(E2)$ and Q_{2^+},
     requiring two independent measurements of the excitation probability
     with differing sensitivity to Q_{2^+}.

       The basic difficulty that arises in all reorientation experiments
involving target excitation is that the effect to be measured is small.
For example, the difference in $P_{0^+\rightarrow 2^+}$ for $Q_{2^+}=0$ and $Q_{2^+}=-0.4$ e.b is only
about 8% for 44MeV ^{16}O projectiles back scattered from ^{112}Cd. Therefore,
in order to measure Q_{2^+} within a reasonable error of, say, 0.05 e.b, the
excitation probability has to be determined to 1% accuracy. At such a
level of precision any additional effects which may contribute to the
excitation probability by more than 0.5% become important and require
investigation. Some of these were mentioned at the end of the last section
and will be discussed in more detail in chapter 4.

       From the properties of equation (2.31) listed in (a) and (c),
it is evident that the reorientation effect can be isolated by either
varying the projectile species or the particle scattering angle. Varying
the bombarding energy (property b) does not produce a sufficiently large
change in $P_{0^+\rightarrow 2^+}$ to permit accurate determination of both the $B(E2)$ and
Q_{2^+}.

       Quantitatively, if P_a is the excitation probability for one type
of projectile (or scattering angle θ_a) and P_b for another (or scattering

angle θ_b), equation (2.31) for the two cases gives

$$P_a = B(E2)F_a(1 + \rho_a Q_{2^+})$$

and

$$P_b = B(E2)F_b(1 + \rho_b Q_{2^+}) \quad , \qquad (2.34)$$

where the sensitivity parameter ρ is given by

$$\rho = 1.32 \frac{A_1}{1+A_1/A_2} \Delta E_{0^+ \to 2^+} \frac{K(\theta,\xi)}{Z_2} \quad , \qquad (2.35)$$

and to first order in ρQ_{2^+} ($\rho Q \ll 1$)

$$\frac{P_a}{P_b} = \frac{F_a}{F_b}\left[1 + (\rho_a - \rho_b)Q_{2^+}\right] \quad . \qquad (2.36)$$

This shows that Q_{2^+} can be determined from the ratio of the two excitation probabilities and that the net sensitivity to Q_{2^+} depends on the magnitude of the difference between the two parameters ρ_a and ρ_b. Equation (2.36) implies that in a relative measurement of excitation probabilities (i.e. P_a/P_b) Q_{2^+} is independent of the B(E2) value. In practice this will be true only if the systematic errors arising from the experimental measurements affect P_a and P_b in the same manner. For example, different analysis methods are used in extracting P from [4]He and [16]O particle data (chapter 4) and they will be subject to different sources of systematic error. Therefore, in order to achieve 10% accuracy in Q_{2^+}, in the cadmium isotopes, a 1% accuracy in the B(E2) measurement is required (Be 72).

The excitation probabilities can be determined either by detecting the scattered elastic and inelastic particles or by detecting the γ-rays from the decay of the excited state. In the latter method the γ-rays are usually recorded in coincidence with the inelasticly scattered particles; however, relative measurements are possible if only "singles" γ-rays are detected.

2.6 Measurements Involving Gamma-Rays

a) Particle-Gamma Coincidence Methods

The usual configuration consists of one or more γ-ray detectors, together with a single surface barrier detector placed close to 180° in order to enchance the quadrupole moment effect (see fig. 2.4). An annular surface barrier detector is suitable for this purpose as it can subtend a large solid angle for a given angle of acceptance. The scattered elastic and inelastic particles are resolved by requiring coincidence with the γ-rays emitted from the 2^+ state. The excitation probability is determined from the ratio of the coincident yield I_{coin} to the total particle yield in the surface barrier detector $I_{el}+I_{inel}$. Relatively thick targets can be used as it is not necessary to resolve the elastic and inelastic particle groups in the particle detector. However, the yield is proportional to the product of the solid angles of two detectors and can be low. For a $2^+\to0^+$ transition the coincidence yield can be expressed in terms of $d\sigma_{inel}/d\sigma_{Ruth}$ - which is the quantity of interest - as

$$\frac{I_{coin}}{(I_{el}+I_{inel})} = \varepsilon(E_\gamma)\frac{d\sigma_{inel}(\theta_p)}{d\sigma_{Ruth}(\theta_p)}\left(1+\frac{J_2}{J_0}G_2A_2P_2(\cos\theta_\gamma)+\frac{J_4}{J_0}G_4A_4P_4(\cos\theta_\gamma)\right)d\Omega. \quad (2.37)$$

Here $\varepsilon(E_\gamma)$ is the efficiency of the gamma detector and θ_p and θ_γ are the laboratory angles of the particle and gamma detectors respectively. Quantities J_2/J_0 and J_4/J_0 are geometric attenuation coefficients which account for the finite solid-angle of the gamma detector. The angular correlation coefficients A_2 and A_4 are obtained from the Winther-de Boer program (Wi 66). Finally P_2 and P_4 are Legendre polynomials, and G_2, G_4 are the hyperfine attenuation coefficients. The latter arise from the recoil of highly ionized target nuclei into vacuum. Any unpaired atomic electrons produce strong fluctuating magnetic fields at the nucleus. The interaction of the magnetic dipole moment of the nucleus with these fields

results in a precession of the nuclear spin axis, affecting the angular

distribution of the γ-rays. The effect is a maximum for γ-rays detected

in coincidence with backward scattered particles, and for heavy projectiles,

due to the large recoil imparted to the target nuclei. This effect is

indistinguishable from the quadrupole moment effect and can change the

value of the quadrupole moment derived by more than 40% (Kl 70) if it is

not allowed for. The modified angular distribution can only be determined

experimentally and the parameters $(J_k/J_0)G_k$ are found to be highly sensi-

tive to the axial position of the gamma detector and its effective distance

from the target (Sm 71). If thick targets are used such that the recoiling

nuclei stop in the target (or in the target backing), the angular distribu-

tion is unaffected.

Additional precautions required in the coincidence experiments

include monitoring of the dead time losses in the electronic coincidence

circuitry used. This correction is count-rate dependent and must be

determined during the experiment. It is also important to establish

whether there are any impurity peaks in the particle spectrum. They can

arise from elastic impurity peaks (since I_{el} is required as well as I_{coin}

in order to determine $d\sigma_{inel}/d\sigma_{Ruth}$ – see equation 2.37) or from

coincident events. The latter are important if NaI detectors are used;

due to their poor resolution impurity or reaction γ-rays may be masked

under the $2^+ \to 0^+$ γ-ray.

The two unknowns B(E2) and Q_{2+} can be determined by using two

projectile species (Kl 70) or by varying the angle of the particle detector

(Hä 71). Both methods require an absolute calibration of the γ-ray detec-

tor efficiency. Occasionally, the B(E2) value is known to sufficient

accuracy and the two pieces of data can be used to eliminate the dependence

on $\epsilon(E_\gamma)$ as the ratio P_a/P_b (equation 2.36) is (to first order) independent

of $\epsilon(E_\gamma)$ and B(E2). Gamma-ray angular distributions following Coulomb

excitation with different projectiles are very nearly the same provided

the scattered particles are detected close to 180°. The dependence on

G can be eliminated by using a thick target (or a thick target backing).

The ratio of the two excitation probabilities (e.g. $P_{^{16}O}/P_{^4He}$) will then

be approximately independent of angular distribution effects (see equation

2.37 and Thomas et al., Th 73). However, the angular distributions of the

de-excitation γ-rays are different for different projectile scattering

angles and a correction ($\sim$2-10%) to $P_{\theta_1}/P_{\theta_2}$ has to be applied in the "two

angle" method (Th 71).

b)   Reorientation Precession Method

This method uses the original idea suggested by Breit et al.

(Br 56) for measuring quadrupole moments. As mentioned in section (1.6e)

the angular distribution of γ-rays following Coulomb excitation is sensi-

tive to Q. In a method first used at Copenhagen (Gr 73) and subsequently

further developed at Uppsala (Ha 76), the γ-rays are detected in coinci-

dence with particles observed in two surface barrier detectors placed at

90° and 127° to the beam direction. The ratio of the γ-ray yields in two

NaI detectors placed at appropriate angles to maximize the reorientation

effect can be related to Q. The results are less sensitive to contribu-

tions from higher states, but the change in the angular distribution

pattern due to the non-zero Q value is small and the measurements are

difficult. However, this type of measurement has the great value that

the sign of the interference term involving the second 2^+ state can be

determined (see equation 2.33 and references Ha 76, Fa 76).

c)   Singles Gamma-Rays

The B(E2) and Q_{2^+} values are again determined by varying the

projectile mass. The target contains several isotopes (for example natural targets have been used, Steadman et al., St 70) and the relative yields of the γ-rays from these are detected in a single Ge(Li) counter. Because particles are not detected there is no normalization to the Rutherford cross section and only the relative values of Q can be measured. The sensitivity to reorientation effect is smaller than for coincidence techniques due to the averaging over all particle scattering angles. However, thick targets and heavy projectiles (^{32}S, ^{40}Ar) can be used to compensate for the reduced sensitivity.

2.7 Particle Spectroscopy

The excitation probability can be determined directly by resolving the elastic and inelastic particle groups with a surface barrier detector or a magnetic spectrometer. This method avoids the need for coincidence electronics, and for corrections due to deorientation effects observed in γ-ray angular distributions. The excitation probability is determined absolutely from the ratio $I_{inel}/(I_{inel}+I_{el})$ from a single spectrum. There is no need for charge integration, correction for random coincidences or detector efficiency measurements. The last point is significant in B(E2, $0^+\to2^+$) measurements as particle spectroscopy is capable of yielding highly accurate (~1%) values for this quantity. However, complications may arise from impurity peaks in the region of interest. Target material enriched in one isotope always contains small amounts of other isotopes. Contaminants in the region of the elastic and the inelastic peaks can arise from target impurities or from reactions with lighter mass nuclei in the target (see chapters 3 and 4). The two basic methods used exploit the effect of varying either the projectile mass or scattering angle on the reorientation term in equation (2.31).

a) Variation of the Scattering Angle

The excitation probability is measured at several scattering angles and usually for a few bombarding energies. The variation of $F(\theta,\xi)$ and $K(\theta,\xi)$ with scattering angle is shown in figure 2.3. At forward angles $dP/d\theta$ is large and P is small. For 44MeV ^{16}O scattered from ^{112}Cd the change in P is 2.5% per degree at 90° but less than 0.1% per degree at 175°. In order to achieve the high accuracy (~1%) needed in the measurement of the excitation probability the scattering angle, therefore, has to be determined accurately at forward angles. Methods have been developed to measure this quantity to better than 0.1° (Be 70 and Bo 76). The scattering angle is sensitive to fluctuations of the beam spot position on the target and the incident beam has to be well collimated. Degraded beam components due to slit-edge scattering from beam and detector collimators produce backgrounds and adversely affect energy resolution. The background can be minimized by using 'anti-scattering' collimators (de Ca 71). Energy resolution is also affected by target uniformity, target thickness and energy straggling in the target, necessitating the use of thin targets. The problem is compounded for heavy ions due to increased energy loss and kinematic broadening, especially at forward scattering angles. Kinematic compensation is available in magnetic spectrometers of Enge or QD^3 type (En 74). If a magnet is used, however, the charge-state distribution of the scattered beam has to be determined experimentally. The distribution depends on bombarding energy, target thickness (for thin targets) and possible charge exchange in the spectrometer vacuum (Cl 69).

b) Variation of the Projectile Mass

This is the method employed in the present work to measure the quadrupole moments of Cd isotopes. The projectiles used are ^{4}He and ^{16}O.

The elastic and inelastic particle groups are resolved in an annular detector at backward angles. The advantages of this technique over method (a) are:

1) The annular detector can subtend an order of magnitude larger solid angle compared with magnetic spectrometers or with ordinary surface barrier detectors. This is facilitated by the small kinematic energy broadening of spectrum peaks at 180°.

2) The reorientation effect is a maximum at backward angles (see figure 2.3) and the variation of excitation probability with angle approaches zero as θ_{lab} approaches 180° (fig. 2.4). Therefore, the beam does not have to be well-collimated and precise angle definition is not necessary. Furthermore, the axial symmetry of the annular detector minimizes the effect of changes in beam trajectory on the mean scattering angle.

3) Maximum possible mass separation occurs at 180°, thus providing greater sensitivity for detection of impurities. This is an important point as contaminants, even of the order of $5ng/cm^2$, can significantly affect the results if they interfere with the inelastic scattering peaks. The question of possible contaminants that may affect the present results will be discussed in detail in chapter 3.

The main drawback of this method over that described in section (a) arises from the use of two projectile species. The particle spectra associated with these are different and require different methods of analysis. The systematic errors in each case will, therefore, be different, and do not cancel when the ratio of the two excitation probabilities (see equation 2.36) is taken.

These points are further discussed in the next chapter where the experimental procedures used are detailed.

CHAPTER 3.

EXPERIMENTAL PROCEDURES

As outlined in section 2.7(b), the experimental method used in the present work to determine the quadrupole moments of the first excited 2^+ states of the even-A cadmium isotopes, involves the measurement of the excitation probabilities at a number of well-defined bombarding energies with ^{4}He and ^{16}O beams. The accuracy and reliability of the information obtained from these measurements depend critically on

a) The quality of the scattered particle spectra: The inelastic peak in the spectrum is considerably smaller than the elastic peak and sits on the low energy tail of the elastic peak as shown in figure 4.1 both for ^{4}He and ^{16}O spectra. A useful criterion of spectrum quality is the ratio of the height of the inelastic peak to the minimum in the valley between the elastic and inelastic peaks. Extensive investigation showed that spectrum quality was influenced principally by detector characteristics, design of the collimation system, the uniformity of the targets and the quality of the incident beam.

b) The absence of elastic impurity peaks which could interfere with inelastic scattering from cadmium: Small amounts of such impurities ($\sim 5\,ng/cm^2$) can seriously affect the results of the present work. Therefore, the targets have to be demonstrably free of contaminant elements in the appropriate mass region.

c) A knowledge of the exact bombarding energy: The excitation probabilities are highly sensitive to small changes in beam energy. This should be determined to sufficient accuracy and checked periodically for possible variations.

In the following sections it will be shown that the above requirements for the reliable determination of quadrupole moments from particle spectroscopy have been satisfied in the present work.

3.1 Accelerator and Beam Handling System

Singly charged negative ^{4}He and ^{16}O ions are produced in a duoplasmatron negative ion source (NIS) by charge exchange in lithium vapour and hydrogen gas respectively. They are then accelerated to the appropriate bombarding energies in the ANU model EN tandem accelerator. The negative ions are accelerated toward the positively charged terminal of the tandem at potential $+V_t$. Here several electrons are stripped from each particle in passing through a carbon foil. The positively charged ions emerging from the stripper are repelled from the terminal and further accelerated to ground potential. The total energy E acquired in this process (assuming that there was no molecular break-up in the NIS exchange canal) is

$$E = (q+1)V_t + 2V_{exch} \quad , \tag{3.1}$$

where q is the charge state of the accelerated particle after stripping at the terminal and V_{exch} is the voltage at the exchange canal. Exchange voltages of 22 to 25keV and 30 to 35keV were used for ^{4}He and ^{16}O ions respectively. The Coulomb barrier in the cadmium isotopes is at about 44MeV bombarding energy for ^{16}O ions and 10MeV for ^{4}He (Be 72). The ANU EN tandem is capable of accelerating ^{4}He^{++} ions up to about 19MeV and ^{16}O^{6+} ions to 44MeV (the intensity of ^{16}O^{7+} ions is too small for reorientation effect measurements). Therefore it was not practicable to investigate the behaviour of the cross-section for inelastically scattered ^{16}O ions above the Coulomb barrier. However, this was done for ^{4}He projectiles (see section 4.5).

A schematic drawing of the beam handling system downstream from the object slits is shown in figure 3.1. Features of the various components relevant to the present experiments are:

a) The object (O) and the image (I) slits of the analyzing magnet (AM) were both set at a total separation of 1.27mm throughout the experiments. These unusually narrow slit settings were found to be necessary in order to obtain a reproducible energy calibration for the accelerator (see section 3.6).

b) A 6mm diameter aperture (C1) was placed immediately before the switching magnet (SwM) in order to intercept degraded beam scattered from the walls of the analyzing magnet vacuum chamber and the image slits.

c) The incident beam trajectory through the annular detector was defined by a single collimator (C2). The diameter of this collimator was 7mm for ^{4}He measurements and diameters of both 3 and 7mm were used for the ^{16}O measurements.

d) In order to minimize the effects of backscattering from the beam dump, the beam was collected in a Faraday cup (FC) lined with carbon anti-scattering collimators (C3 and C4) and a carbon beam stop (BS) situated approximately 4m beyond the target (T).

Collimators C1, C2 were made of thin (0.38mm) tantalum metal and the surfaces exposed to the beam were highly polished with alumina paste in order to minimize slit-edge scattering. These collimators and the object and image slits were cleaned and polished at regular intervals to remove carbon deposited by the beam. Beam focusing and intensity were considerably improved when thin (2-4μg/cm^2) carbon stripper foils were installed in the terminal of the accelerator in place of the 10-15μg/cm^2 foils used previously. Consequently less than 1% of the beam current was

|←——— 172 cm ———→|

BEAM ↓O

R = 86 cm

AM

(O)   Object slits

(AM)   Analyzing magnet

(I)   Image slits

(C1)   Tantalum collimator

(SwM)   Switching magnet

(QD)   Quadrupole doublet
          (steering)

(C2)   Tantalum collimator

(AD)   Annular detector

(T)   Target

(SC)   Scattering chamber
          25 cm radius

(C3,C4)   Carbon collimators

(FC)   Faraday cup

(BS)   Carbon beam stop

I

Cl

SwM

25°

QD

C2

AD

T   SC

C3

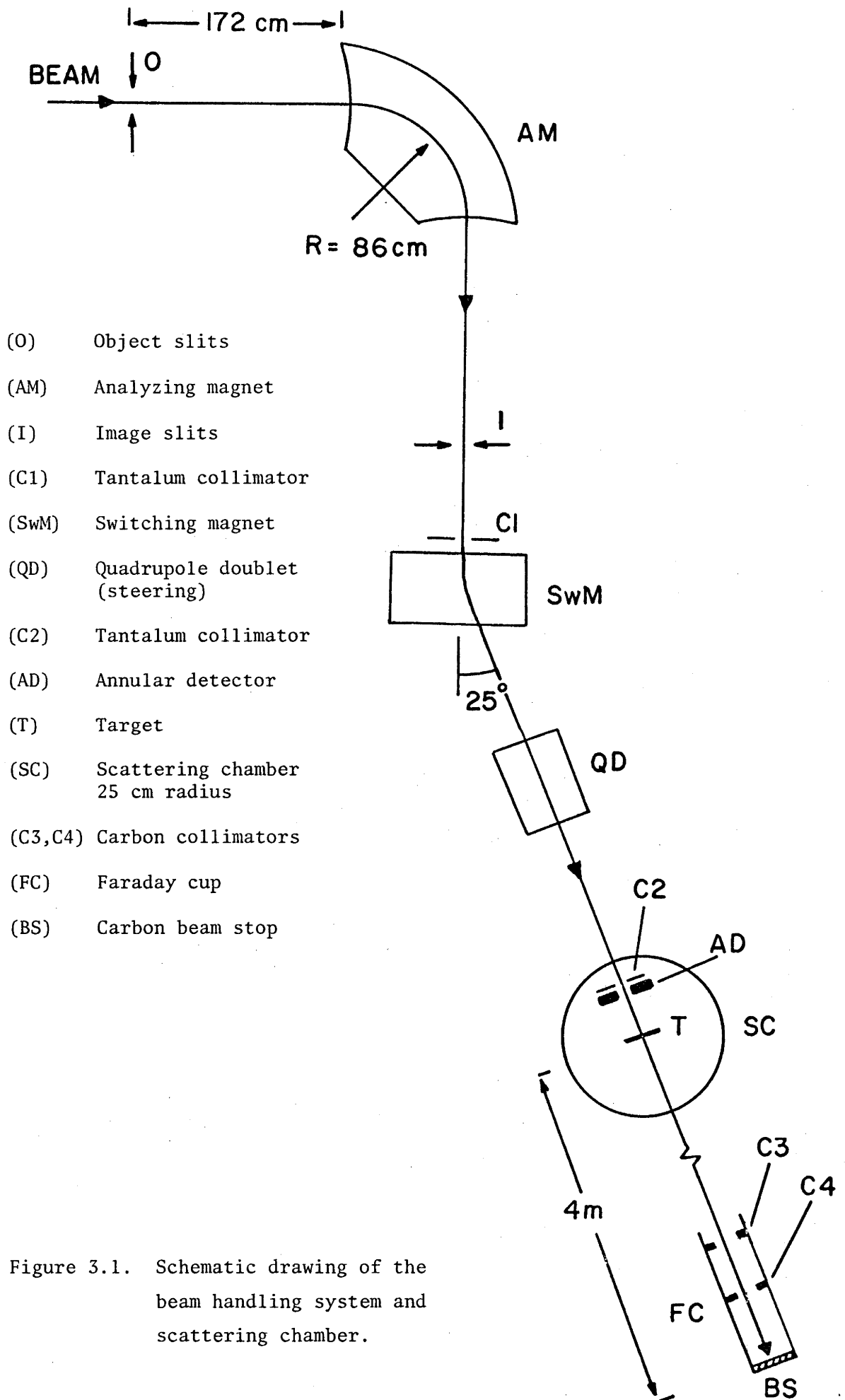C4

4m

FC

BS

Figure 3.1.   Schematic drawing of the
              beam handling system and
              scattering chamber.

intercepted by the beam defining aperture (C2) at the annular detector.

This collimator was insulated from the rest of the detector assembly and

the intercepted beam was closely monitored during the experiments. Typical

beam currents were 200-300nA on target for both $^4He^{++}$ and $^{16}O^{6+}$ ions.

Foil lifetime, for the present purposes defined as the time

interval during which the beam intensity dropped to less than half of its

initial value, was 3-4 hours for ^{16}O beams. The drop in beam intensity

was accompanied by an increase in beam intercepted at the collimator C2.

The terminal stripper assembly contains 224 carbon foils so that the high

usage rate did not result in unduly frequent tank openings for replacement.

In ^4He measurements the stripper foils lasted for several days without

noticeable deterioration.

3.2 Scattering Chamber Geometry

The scattered particles were detected near 180° with annular

silicon surface barrier detectors. This arrangement has several advantages

as discussed in chapter 2. At scattering angles near 180° the variation of

$F(\theta,\xi)$ and $K(\theta,\xi)$ with θ is slow (see fig. 2.3) and so less stringent

requirements are imposed on the definition of scattering angle than would

be the case at other angles. The axial symmetry of the detector system

minimizes the effect of changes in beam trajectory on the mean scattering

angle. Therefore, a relatively large diameter beam defining collimator

(C2 in fig. 3.1) could be used which is desirable for the reduction of

slit edge scattering. Kinematic energy broadening of spectrum peaks is

small at backward angles so that large solid angles and hence faster data

collection rates can be achieved.

A schematic drawing of the scattering chamber arrangement is

shown in figure 3.2. The beam defining collimator (C2) is the same as

that shown in figure 3.1. A 6mm thick tantalum annulus (TS) protects the

(C2)   Beam defining collimator

(CM)   Collimator mount

(TS)   Tantalum shield

(AD)   Annular surface barrier detector

(IC)   Inner collimator

(OC)   Outer collimator

(HSM) Horse-shoe magnet

(BM)   Bar magnet

(CS)   Cold shroud

(T)   Target

(d)   Detector target distance, 4.4 cm for
       ^{4}He and 6.9 cm for ^{16}O projectiles

(θ)   Angle subtended at the detector,
       θ_1=7°, θ_2=9.7° for ^{4}He projectiles
       θ_1=4.5°, θ_2=6.2° for ^{16}O projectiles
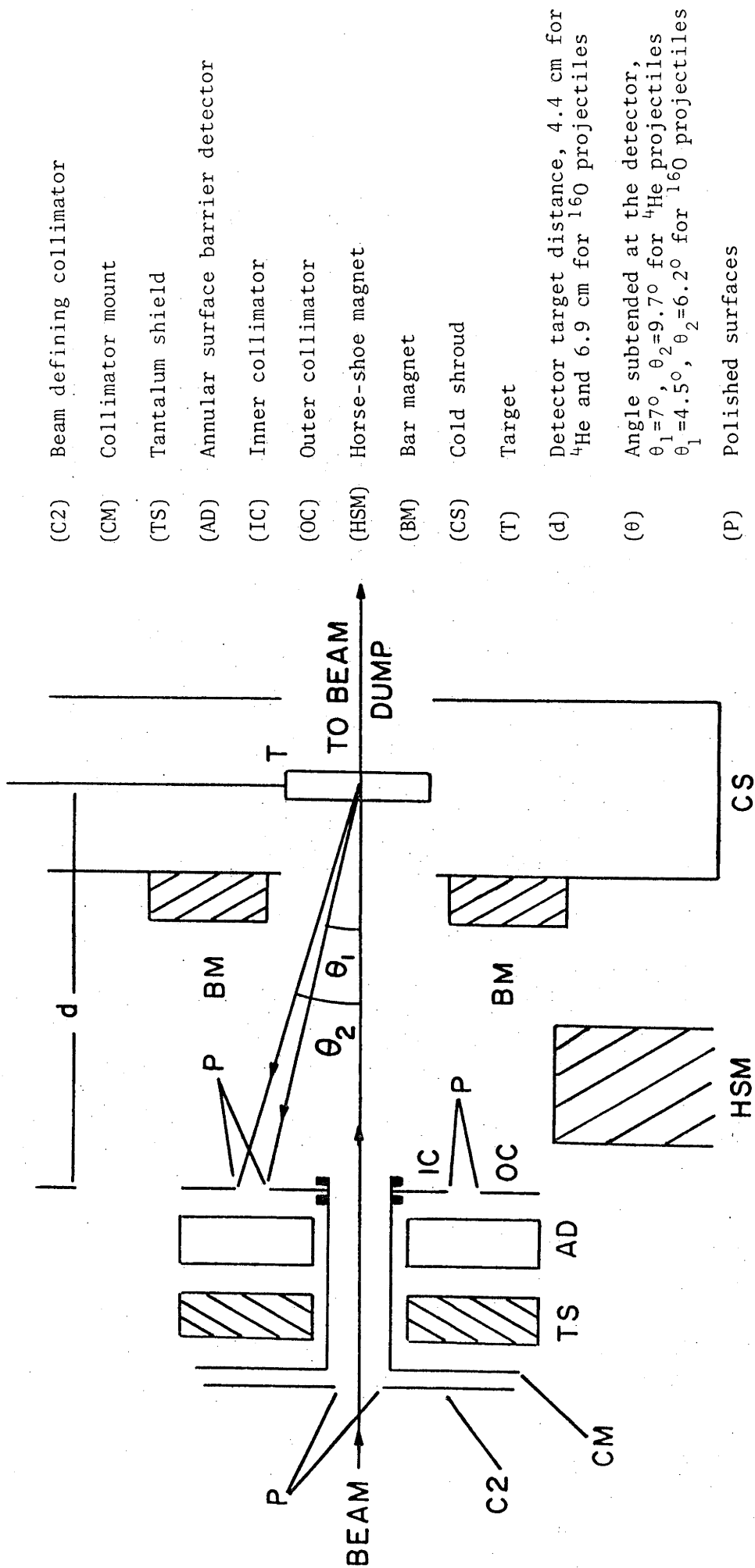
(P)   Polished surfaces

Figure 3.2.   Scattering chamber geometry.

annular detector (AD) from X-rays generated by beam intercepted at collimator C2. The detector solid angle for the back scattered beam was defined by two highly polished tantalum collimators (IC) and (OC). The target (T) was surrounded by a copper shroud (CS) cooled with liquid nitrogen to inhibit the deposition of carbon and other impurities during bombardment. Permanent bar magnets (BM) mounted on the shroud and a horse-shoe magnet (HSM) placed below the detector were used to prevent secondary electrons from the target and shroud walls streaming into the detector. The measured maximum magnetic field produced by these magnets along the incident or scattered beam path was 200 Gauss. Assuming a uniform magnetic field of this magnitude between the detector and the target the maximum deflection of the back scattered beam is less than 0.1°. Thus the electron suppression magnets have a negligible effect on the back scattered beam trajectory. During the initial measurements various other methods of electron suppression were tested. In one, the electrons were repelled from the detector by placing a negatively biased ($\sim$-2kV) annular electrode close to the detector. No significant improvement in detector resolution was observed compared to magnetic suppression which is safer and much more convenient to use. A photograph of the scattering chamber arrangement is shown in figure 3.3.

The burn marks on the target indicated that the beam was closely centred on the optical axis of the collimator mount (CM) and was largely concentrated in an area about 2mm wide. The detector-target separation (d) was 6.9cm for the ^{16}O measurements at a mean angle of 174.6° and solid angle of 17msr. For ^{4}He measurements the separation was 4.4cm at a mean angle of 171.6° and solid angle of 40msr. This geometry together with the observed beam spot size introduces a total kinematic broadening in the cadmium scattering peaks of 10keV and 35keV for ^{4}He and ^{16}O projectiles respectively.

Figure 3.3

Photograph of the scattering chamber arrangement.
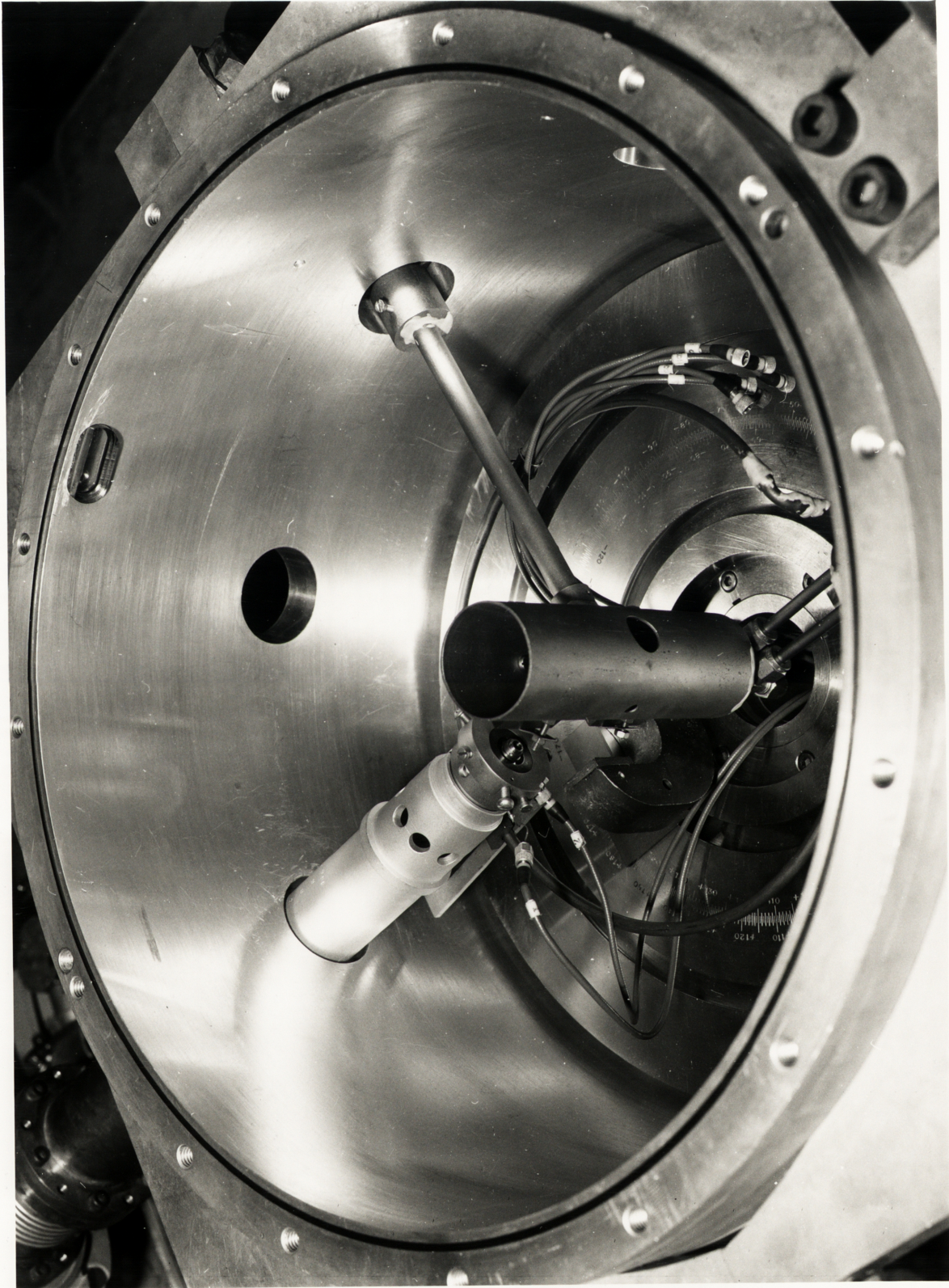
3.3 Annular Surface Barrier Detectors

Line shapes obtained with surface barrier detectors generally have low energy tails due to incomplete charge collection and non-ionising energy loss in the detector, particularly for heavy ions such as ^{16}O. The charge collection efficiency improves with increased collection fields and these can be achieved by using low resistivity detectors, over-biasing the detectors, or both. Initially, the annular detectors used were locally made (St 74). Various fabrication methods and the effect of silicon resistivity on resolution were investigated. However, all of these detectors had high room temperature leakage currents and produced large low energy tailing for ^{16}O ions. Suitable detectors were purchased from ORTEC Inc. on special order. The energy resolution and tailing obtained with these detectors was quite adequate. The nominal active area and thickness were $300mm^2$ and $100\mu m$ respectively. Collection fields were typically 10 000V/cm, and in the interests of maximum detector life the detectors were not overbiased. To achieve the best possible resolution in ^4He measurements the detectors were cooled to approximately $-40^{o}C$. However, cooling did not make a noticable difference to resolution in ^{16}O measurements. Extensive investigation showed that in ^4He particle spectra the dominant contribution to low energy tailing arises from slit-edge scattering at the collimators defining both the incident and scattered beams. For this reason a large diameter (7mm) beam defining collimator (C1 in figures 3.1 and 3.2) was used at the annular counter in ^4He experiments. In ^{16}O spectra tailing is mainly due to incomplete charge collection and non-ionising energy loss, and beam defining collimators of both 3 and 7mm were used with similar results. Typical energy resolutions obtained with these detectors were 24keV and 105keV for ^4He and ^{16}O projectiles respectively.

An exploded view of the annular detector assembly is shown in figure 3.4. The detector mount (DM) is thermally and electrically insulated from the scattering chamber with two O-rings (OR) and fits tightly into a 25cm long tube (T). The detector is held in place inside the scattering chamber by inserting tube (T) into the beam line (see fig. 3.3). This section of the beam line was optically aligned with the centre of the scattering chamber. The detector can be cooled by clamping the flexible copper arm (CA) onto the cooling ring inside the chamber (visible in the photograph in figure 3.3). The cooling ring is electrically insulated from the scattering chamber and also from the refrigerator underneath the chamber in order to minimize electrical noise from ground loops. The beam defining collimator (C1) fits onto the collimator mount (CM) and is electrically insulated with two teflon spacers (TS). The inner collimator (IC) is held on a thin walled cylindrical tube which fits over the nozzle on the beam defining collimator mount. The outer collimator (OC) and the securing end collar (EC) complete the assembly.

As a result of the measures described above and in section 3.1 and 3.2, peak to valley ratios obtained in ^{16}O spectra ranged from 10 to 45 depending on bombarding energy and the quality of individual targets. These values are comparable with those achieved elsewhere (Be 72) in similar experiments. For ^{4}He data peak to valley ratios ranging from 50 to 350 were achieved, representing an order of magnitude improvement on values reported for both semiconductor and magnetic spectrometer measurements by other workers (Be 72, Sa 69).

3.4 Targets

Target quality plays an important role in obtaining satisfactory spectra. Targets must not only be of highly uniform thickness to reduce low energy tailing but must be demonstrably free of impurities which might

Figure 3.4. An exploded view of the annular detector assembly.
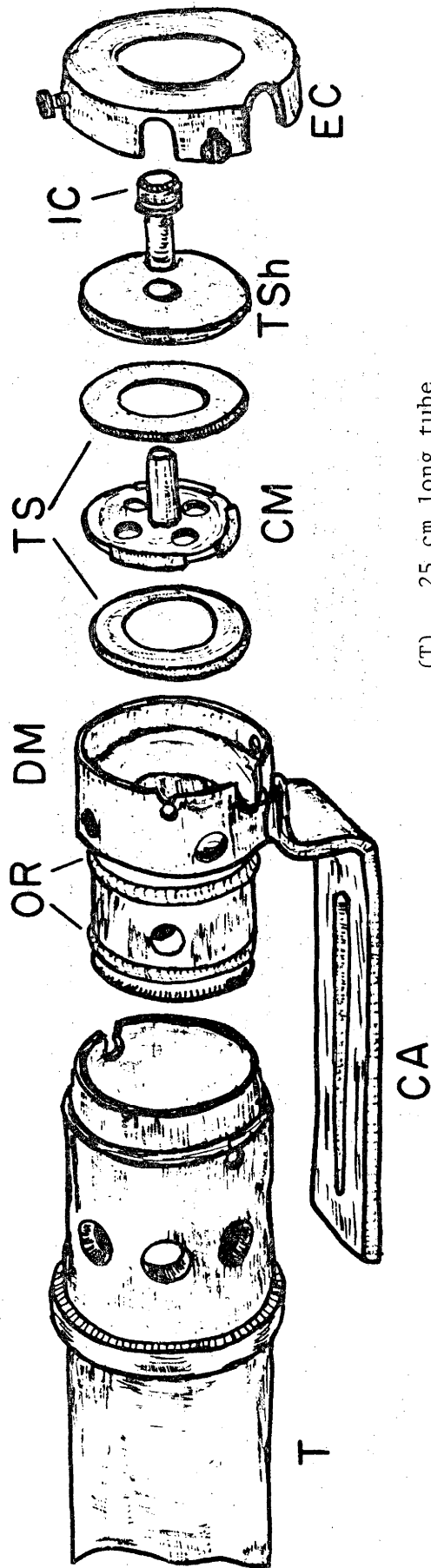
(T)   25 cm long tube

(CA) Flexible copper arm

(OR) O-rings for electrical insulation

(DM) Detector mount

(TS) Teflon spacers

(CM) Collimator mount

(IC) Inner collimator assembly

(EC) End collar for securing the outer collimator

contribute significant contaminant peaks to the spectrum in the vicinity of the cadmium elastic and inelastic peaks. Targets of acceptable uniformity were made by evaporating isotopically enriched $CdCl_2$ (obtained from Oak Ridge Separated Isotope division in oxide form) from a carbon boat in an r.f. heater onto self-supporting $10\text{-}15\mu g/cm^2$ carbon foils. The CdO was converted to $CdCl_2$ by adding a few drops of highly pure ($\sim 10^{-5}\%$) HCl acid (obtained from Merk Inc., Darmstadt).

Considerable effort was expended in keeping the evaporation chamber and carbon foil preparation process free of contaminants. Carbon foils were prepared on microscope slides coated with analytical grade glucose release agent. The vacuum chamber used for carbon deposition was disassembled, sand-blasted and de-greased prior to each evaporation and targets were handled with gloves. Similar precautions were adopted in the r.f. unit while evaporating cadmium. In addition, a cold trap was placed closed to the targets to condense vapours present in the vacuum system due either to back streaming from the diffusion pump or outgassing from the chamber walls, etc. (He 73). Furthermore, the cold trap acted as a heat shield between the hot evaporation boat and the walls of the evaporator thereby reducing outgassing. Up to 24 cadmium targets could be produced in each evaporation with thicknesses ranging from 1 to $10\mu g/cm^2$. The molecular form of cadmium chloride on the targets was checked by bombarding a target with 1.5MeV ^{4}He ions from the ANU model KN Van de Graaff (Ne 75). The relative intensity of atomic X-rays from Cd and Cl detected with a calibrated Si(Li) detector was in agreement with the assumed $CdCl_2$ composition. This information was required in order to calculate the beam energy loss in the target material.

The partial thickness of cadmium on the targets used ranged from 3 to $8\mu g/cm^2$, the thinner targets being reserved for ^{16}O measurements. Corrections to bombarding energy for target thickness were

typically 1keV and 10keV for ^{4}He and ^{16}O beams respectively.

Under bombardment, particularly with ^{16}O beams greater than
about 100nA, the CdCl$_2$ targets were found to evaporate rapidly. This
initial difficulty was overcome by evaporating onto half the target area
a layer of carbon approximately 1μg/cm^2 thick. With this protective
layer the targets could withstand ^{16}O beams of at least 250nA for long
periods without significant deterioration in thickness or uniformity.
The energy loss of the beam in the protective carbon layer was measured
by comparing spectra obtained by bombarding first the protected then the
unprotected areas of the target. This energy loss was less than 2keV
and 10keV for ^{4}He and ^{16}O beams respectively.

3.5 Target Contaminants

The contribution of contaminant peaks arising from target
impurities was thoroughly investigated. Due to incomplete isotopic
enrichment all targets contained small amounts of cadmium isotopes other
than the one of interest; the procedure for correcting spectrum intensi-
ties for contributions from these impurities is described in chapter 4.
To investigate the possible presence of impurities other than cadmium,
all the spectra obtained with both ^{4}He and ^{16}O projectiles, over the full
range of incident energies (8 to 17.5MeV and 40 to 44MeV for ^{4}He and ^{16}O
projectiles respectively) were carefully examined for any indication of
impurities which might contribute elastic scattering peaks in the region
of the cadmium 2^+ peaks. Small amounts (~ 5 ng/cm^2) of such impurities
could significantly affect the present results. The ^{4}He and ^{16}O data are
sensitive to contaminant elements which widely differ in mass and will be
considered separately. However, for a given isotope the targets used in
^{4}He and ^{16}O experiments were produced in a single evaporation at the same

time (section 3.4). Therefore, it is unlikely that individual targets used in ^{4}He and ^{16}O experiments contain significantly different amounts or different types of impurities.

a)   The ^{4}He Data

Elastic peaks from contaminants in the mass range A=65 to A=84 could interfere with cadmium 2^+ peaks. Any such impurity peaks, however, would shift, relative to the 2^+ peak, by about 70keV per MeV change in the bombarding energy. Given the resolution and peak to valley ratios obtained in the ^{4}He experiments these peaks would have been visible in some of the data taken between 8 to 12MeV bombarding energy range. The only significant impurity identified was a small amount of copper (<0.1ng/cm^2). At the lowest bombarding energies of 8 and 8.5MeV, in ^{4}He spectra, this peak interfered with the 2^+ peaks from ^{106}Cd and ^{108}Cd but it was well clear from the ^{110}Cd 2^+ peak in the 8.5MeV spectrum. The ^{106,108}Cd data at 8 and 8.5MeV bombarding energy and the ^{110}Cd 8MeV data were all excluded from the final analysis. No other impurity peaks were observed, and, owing to the excellent peak to background ratios achieved in the ^{4}He spectra, an upper limit of 0.4% (or 0.1ng/cm^2, assuming Rutherford scattering) in the worst case could be placed on the contribution of any such impurity peaks to the intensity of the cadmium 2^+ peak. In addition, representative samples of the carbon backings were bombarded with both ^{4}He and ^{16}O beams and again no indication of impurities which could contribute peaks in the region of interest was observed.

b)   The ^{16}O Data

Elastic scattering from elements with mass A-4 can interfere with inelastic scattering from ^{A}Cd. The only such stable elements are

the isotopes of Ru, Pd and Sn. For example, ^{110}Pd (natural abundance

11.8%), if present in the targets, would interfere with the ^{114}Cd 2^+

peak. However, one would expect ^{104,105,106,108}Pd to be present as

well. A ^{114}Cd-^{16}O spectrum is shown in figure 3.5, in which the expected

positions of the Pd impurity peaks are marked. If present, ^{104}Pd (11.1%

natural abundance) is less than 0.2% of the ^{114}Cd 2^+ peak. The intensity

of the ^{114}Cd "higher states" (fig. 3.5) can be calculated since their

matrix elements are known (see chapter 4). The calculated ratio =

(intensity of higher states)/(intensity of the 2^+ peak) is 3.4%; the same

ratio extracted from the spectrum in figure 3.5 is 3.2±0.2%. Therefore,

to within twice the statistical errors, an upper limit of 0.2% can be

placed on the presence of ^{105}Pd impurity relative to the 2^+ intensity.

In the approximation that elastic scattering from the contaminant is pure

Rutherford, the 0.2 % figure corresponds to an upper limit of 0.5ng/cm^2.

Similar arguments can be presented in the case of ^{106,112,116}Cd isotopes.

However, the possibility of ^{104}Pd and ^{106}Pd elastic peaks under the ^{108}Cd

and ^{110}Cd inelastic peaks cannot be excluded in this way since the other

palladium isotopes would be obscured by the cadmium peaks. However, this

possibility is rendered most unlikely by the non-observation of palladium

isotopes in the other cadmium targets. Furthermore, as stated earlier

the same batch of targets were used for both ^{4}He and ^{16}O experiments; there

is no indication of palladium contaminants in any of the ^{114}Cd-^{4}He spectra

which range in bombarding energy from 8MeV to 17.5MeV.

3.6 Accelerator Energy Calibration

A change of 1 part in 1000 in the bombarding energy produces, both

for ^{4}He and ^{16}O projectiles, a 0.5% change in the excitation probability of

the 2^+ state. Therefore, the beam energy must be accurately known. The

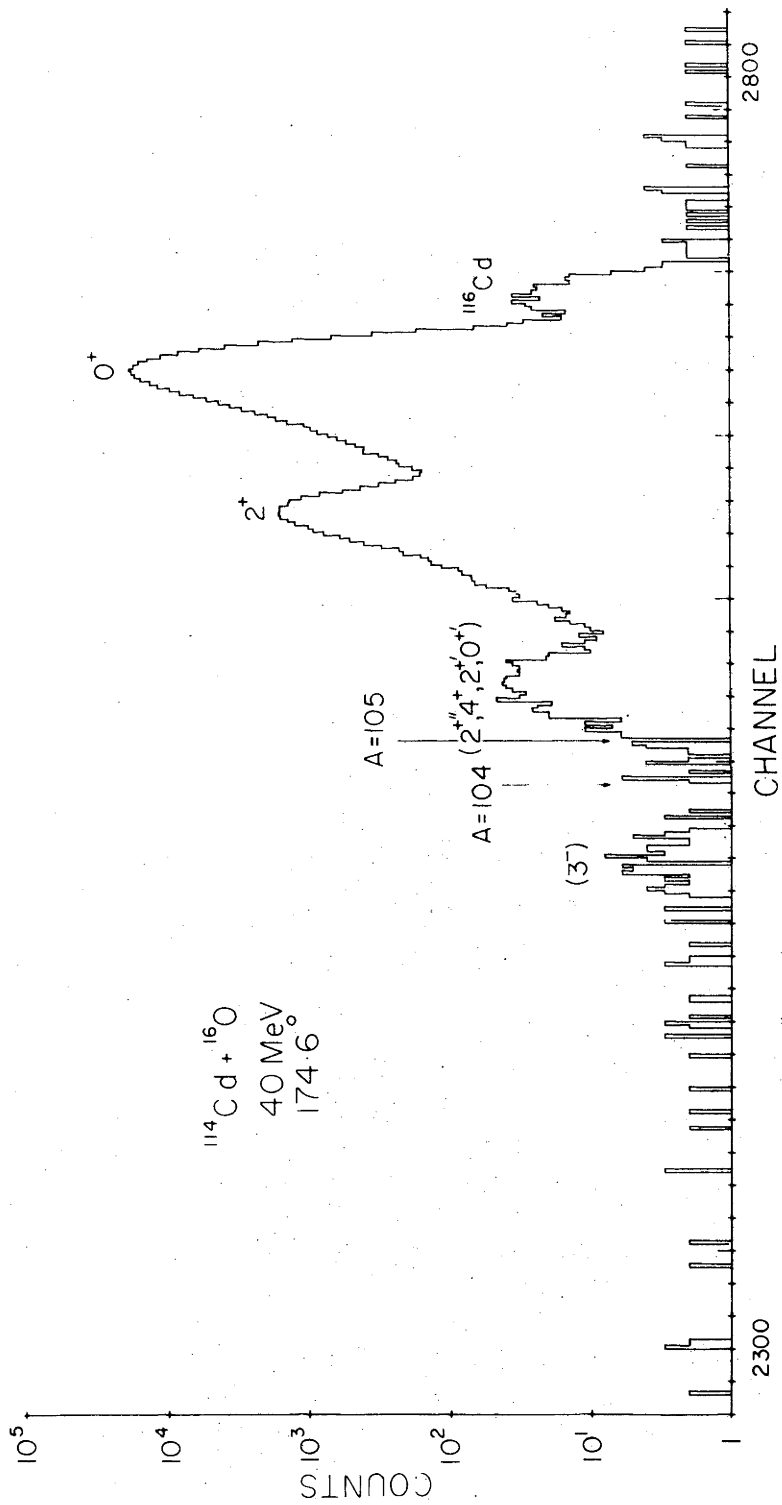previous energy calibration of the analyzing magnet was carried out mainly

Figure 3.5. Spectrum of 40MeV ^{16}O ions backscattered from ^{114}Cd. The arrows indicate the positions of ^{104}Pd and ^{105}Pd impurities. The ^{116}Cd isotopic impurity visible on the high energy side of the elastic peak is due to about 6ng/cm^2 of ^{116}Cd in the target.

through (p,n) reaction threshold measurements up to about 10MeV in proton energy (Mo 69). The analyzing magnet was recalibrated, and measurements extended to the higher fields required in the present experiments, by using the $^2H(^{16}O,n)^{17}F$ reaction threshold, and also by comparison of scattered ^4He beams with α-particle groups from a thin ^{212}Pb source. The latter method could readily be repeated and was used at regular intervals to check the constancy of energy calibration. The experimental procedures and the results of these measurements will be detailed below.

a) The Analyzing Magnet

The beam is momentum analyzed by a double focusing magnet with mass energy product (ME/q^2) of 52, radius of 86cm and maximum field of 12kg. It exhibits negligible differential hysteresis effects, as established by earlier measurements (Mo 66), and energy changes can be made reproducibly without recycling the magnet. This was confirmed during the present experiments using the second of the two above-mentioned calibration methods. Nevertheless, as a precautionary measure, the magnet was always recycled. The recycling procedure consisted of bringing the magnet to full field, allowing it to settle down, then reducing the field to zero and repeating the procedure three times before adjusting the current for the desired field without overshooting. The effects on beam energy produced by changes in the low and high energy accelerator parameters were investigated and were found to be negligible.

b) The $^2H(^{16}O,n)^{17}F$ Reaction

The well established (Fr 76 and references therein) $^2H(^{16}O,n)^{17}F$ threshold at 14528 ±5keV can be used with ^{16}O ions of various charge states to calibrate analyzing magnets at high fields. Targets can be made of

deuterated zirconium, deuterated polyethylene or heavy water ice, and the neutrons are usually detected with a BF_3 long counter (Ha 47). At 100keV above threshold, the neutrons, in the laboratory system, are emitted in a narrow cone in the forward direction with a half angle of 7° and have an energy spread from 760keV to 920keV. Therefore, a detector with relatively small active area placed close to the target can sample all of the emitted neutrons.

Initially, the neutrons were detected in a 7.6cm diameter boron loaded plastic scintillator (NE402) mounted on a photo-tube. The gain of the photomultiplier could be adjusted to provide some discrimination against gamma-rays. It was found, however, that the background flux of neutrons and gamma-rays was too high for any useful measurements to be made with this detector. Subsequently a modified long counter was used which substantially improved the detection efficiency for reaction neutrons over the background. A schematic drawing of this detector assembly is shown in figure 3.6. The centre hole (CH) for the BF_3 counter was filled with paraffin wax. Three ^3He filled (10 atmosphere pressure) proportional detectors[+] were inserted in three of the eight outer holes (OH) (Ha 47). The ^3He detectors use the reaction

$$^3He + n \rightarrow p + \,^3H + 764keV \quad , \quad (3.2)$$

for detecting the neutrons. Depending on the incident neutron energy, they are 6 to 10 times more efficient than BF_3 tubes. The boron loaded wax shielding (BLW) around the assembly considerably reduced the sensitivity of the ^3He detectors to background neutrons in the target room. Neutrons which diffuse into the counter from the sides scatter and slow down in the wax; they are then captured by ^{10}B through the reaction

$$^{10}B + n \rightarrow \,^7Li + \alpha + 2.792MeV \quad . \quad (3.3)$$

_____

[+] Texlium detectors were purchased from Texas Nuclear Corporation.

TEXLIUM He^3 DETECTOR

(ONE OF THREE)

BLW   PW   CH   PW   BLW

8
HOLES

MC

PA   AMP   ADC   COMP

(BLW)   Boron loaded wax

(PW)   Paraffin wax

(OH)   Outer holes (8)

(CH)   Centre hole for BF$_3$ counter
        filled with paraffin wax

(MC)   Metal can

(PA)   Preamp Ortec model 121

(AMP)   Amplifier

(ADC)   Canberra model 8060

(COMP)   IBM 1800 computer
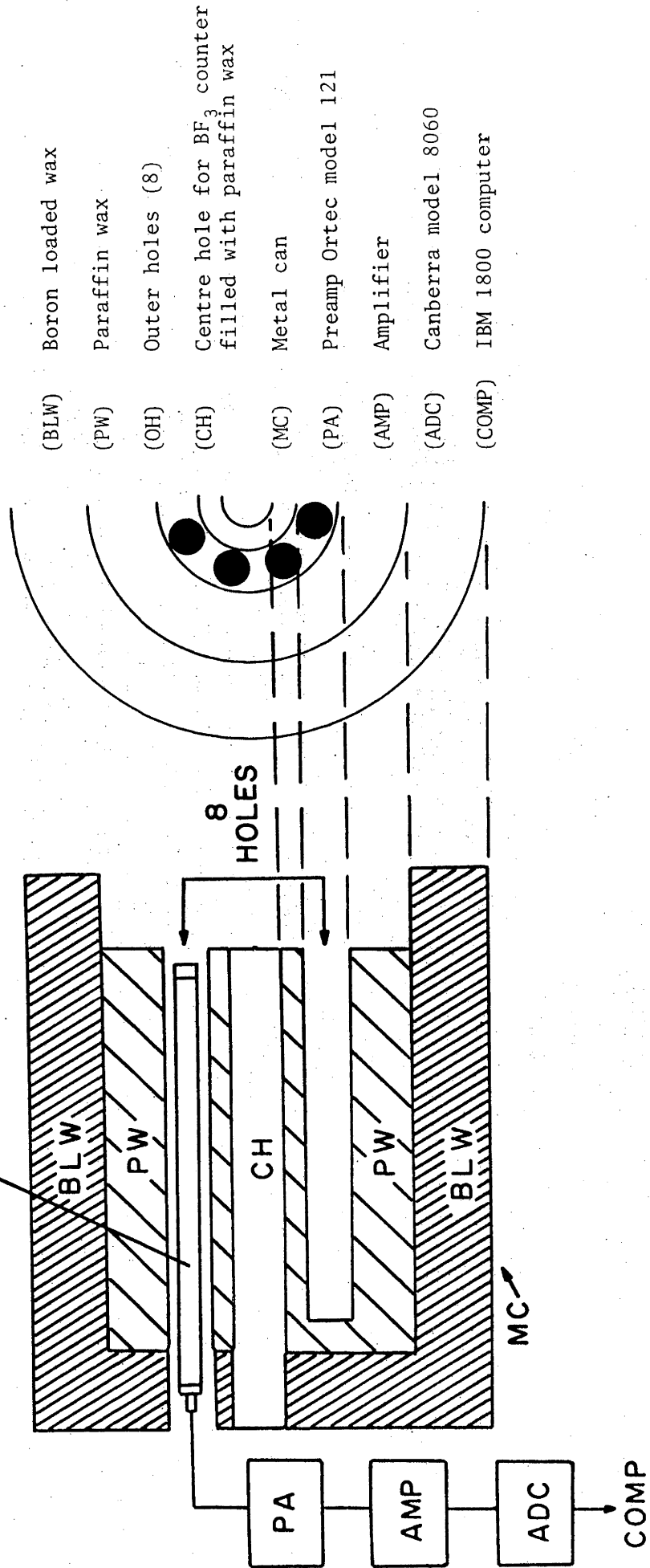
Figure 3.6.   The modified long counter assembly.

FULL ENERGY PEAK: BOTH
PROTON AND TRITON
COMPLETELY STOPPED
IN GAS

$He^3 + n \longrightarrow p + H^3 + (764keV)$

COMPLETE WALL
ABSORPTION   WALL
OF PROTON   EFFECTS

COUNTS

CHANNEL
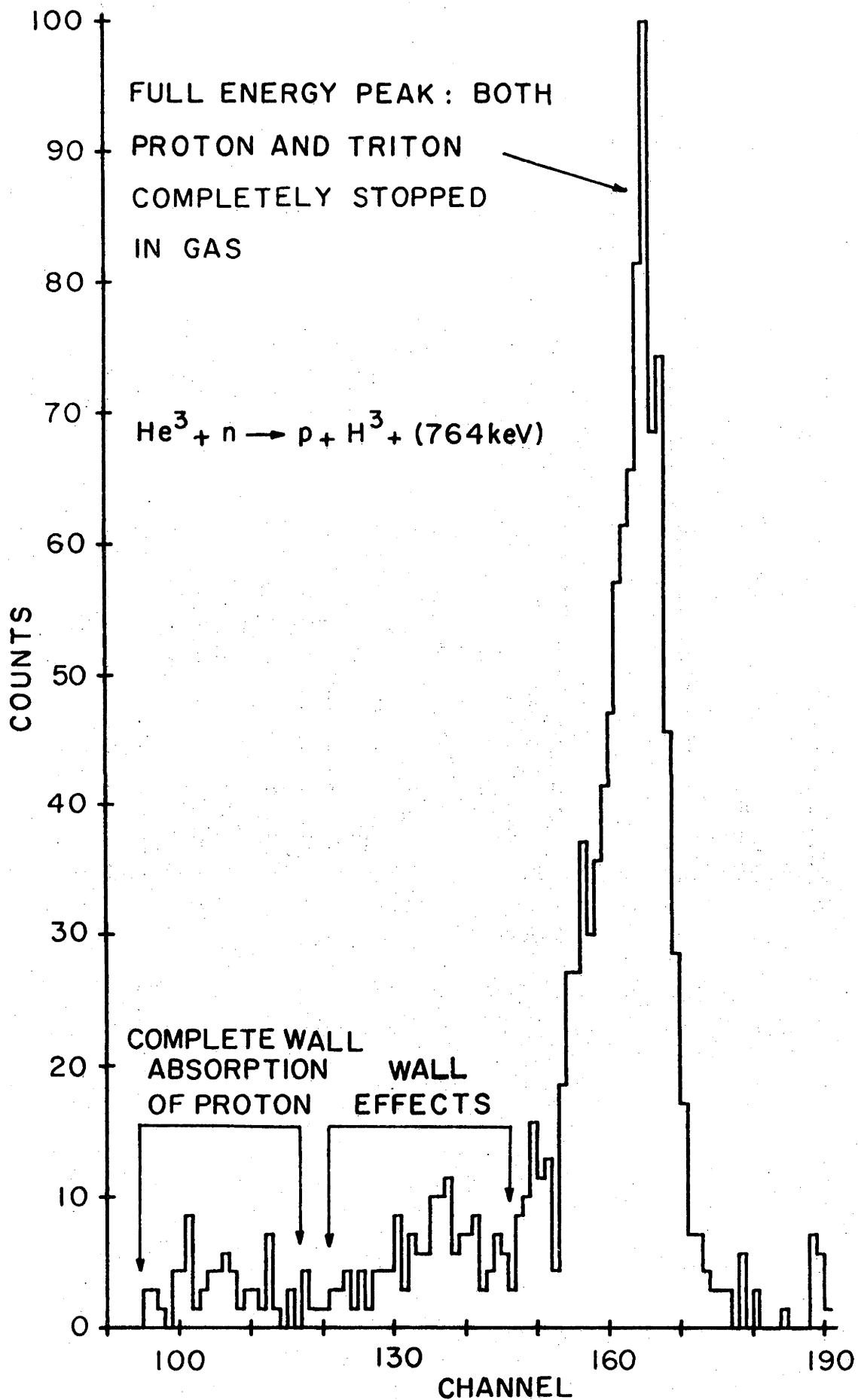
Figure 3.7.   A neutron spectrum from one of the three
(10 atmosphere pressure) ^3He filled proportional
detectors.

(VI)	Heavy water vapour inlet
(SS)	Sliding seal
(PC)	Perspex volatile-target chamber
(N)	Nozzle
(AF)	Negatively biased aluminum foil
(CTB)	Copper target backing
(CS)	Cold shroud
(LN)	Liquid nitrogen reservoir
(BW)	Boron loaded wax block
(CS)	Cadmium metal shield
(LC)	Long counter

Figure 3.8.   The volatile-target chamber and the long counter arrangement.

A typical neutron spectrum from the $^2H(^{16}O,n)^{17}F$ reaction obtained with

one of the ^3He detectors is shown in figure 3.7.

A schematic drawing of the vacuum chamber is shown in figure
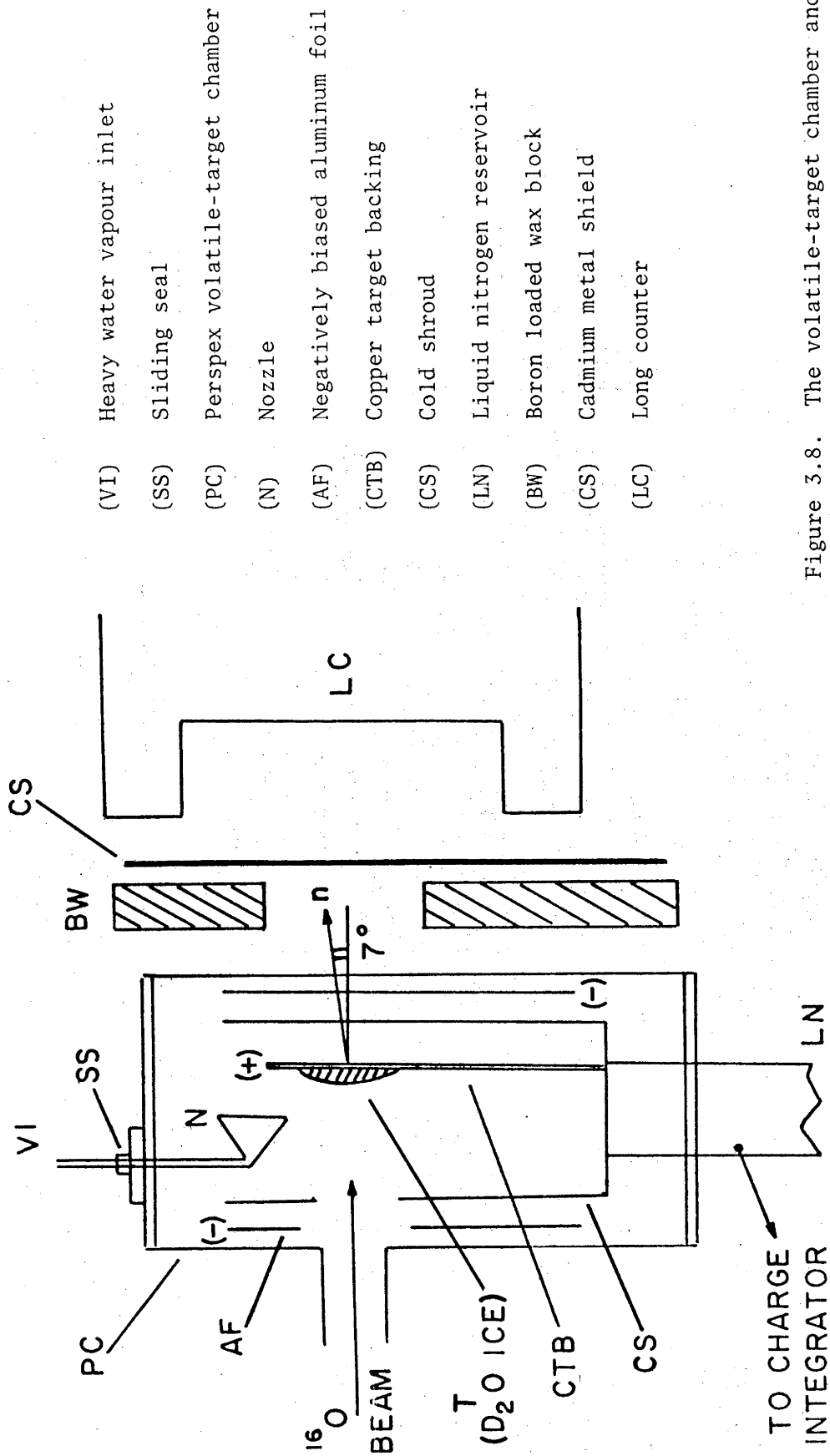
3.8. The target (T) consisted of a thick (~0.2mm) slab of heavy water

ice condensed onto a copper backing (CTB) cooled with liquid nitrogen.

Targets were made in vacuum by lowering a nozzle (N) over the target

area and letting D_2O vapour condense on the cold backing. The target

was frequently scraped under vacuum to remove carbon or other impurity

build-up and then renewed. A cold shroud (CS) surrounding the target

also helped reduce condensation on the target. Additional details of

the volatile-target chamber can be found in reference Op 71. The neutron

detector was shielded from stray neutrons moving along the beam direction

by a 6cm thick block of boron loaded wax (BW) and a sheet of cadmium

metal (CS). The cross-section for slow (<1eV) neutron capture in ^{113}Cd

is large (10^2-10^4 barns, Hu 58). Any slow neutrons which managed to

diffuse out of the boron loaded wax block were thus further attenuated

in the cadmium shield.

The gas stripper in the terminal of the accelerator is no longer

available and carbon foils are used instead. The low terminal voltages

(2.9-3.6MV) required in the calibration experiment resulted in poor beam

intensity and short (<1hr) stripper foil lifetimes. The time required to

complete a threshold yield curve under these circumstances was greater

than the foil lifetime. Consequently, charge integration was unreliable

because it depended on beam intensity. To improve charge integration, an

aluminum foil (AF) was placed inside the perspex target chamber (PC) and

vegatively biased to suppress secondary electron emission from the target.

Target electron suppression for heavy ion beams requires higher voltages

than used for light projectiles such as protons. Figure 3.9 shows the

Figure 3.9. Variation in the target beam current
with the bias voltage on the aluminum
suppressor foil.
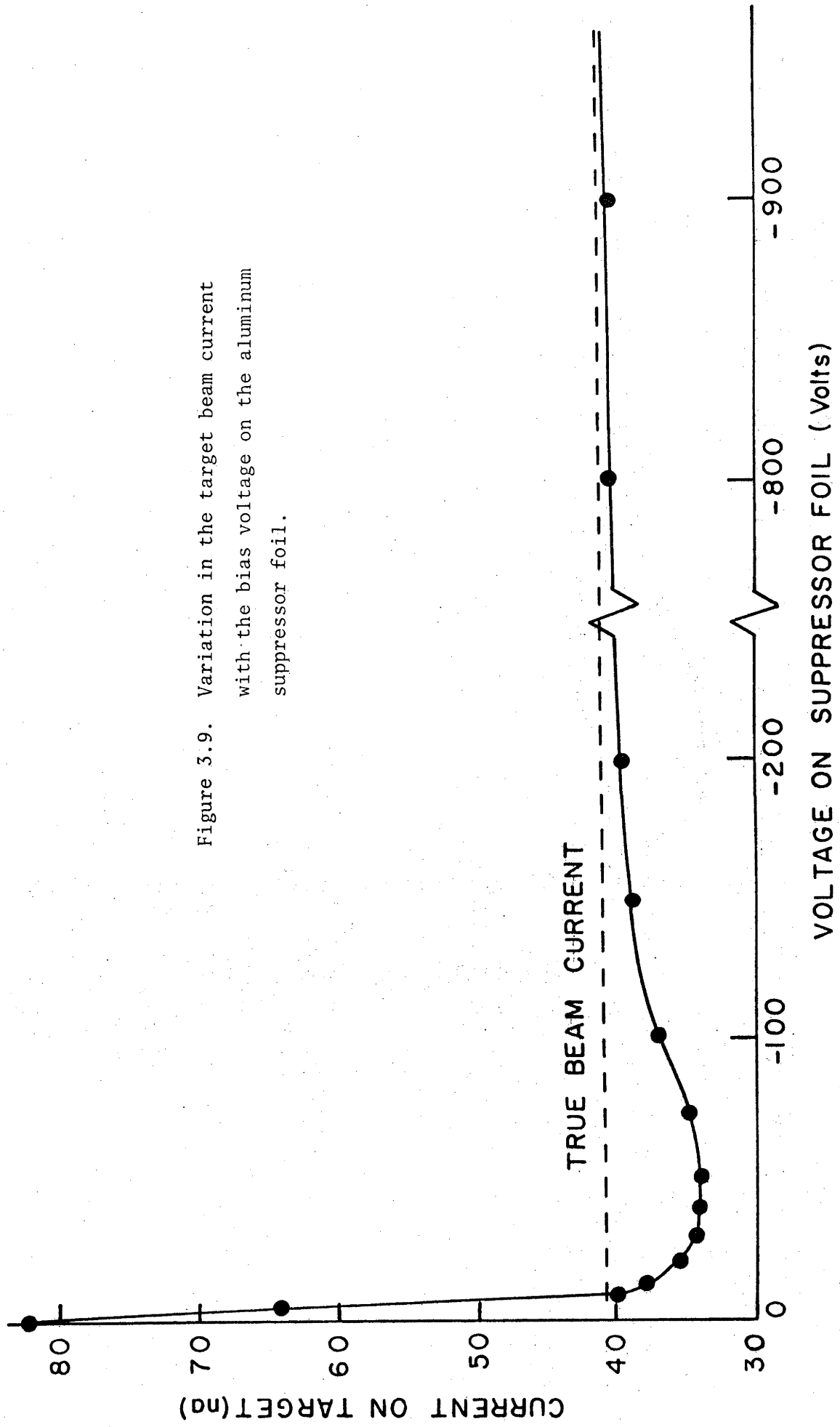
results of biasing the aluminum foil. As the bias is increased beyond
-50V fewer electrons escape from the target; consequently the number of
secondary electrons knocked out of the chamber walls and attracted back
to the target decreases. This phenomenon explains why the registered
target current can drop below the "true" value (Lo 65). Improved charge
collection did somewhat improve reproducibility, but the main problem of
low beam intensity was overcome when thin carbon stripper foils were used
in the terminal (see section 3.1).

Representative threshold yield curves from the $^2H(^{16}O,n)^{17}F$
reaction obtained with $^{16}O^{3+}$ and $^{16}O^{4+}$ beams are shown in figures 3.10
and 3.11. The energy dependence of the total neutron yield Y just above
threshold is given by:

$$Y \propto (E_{beam} - E_{th})^{(2\ell+1)/2} \quad , \qquad (3.4)$$

where ℓ is the orbital angular momentum of the emitted neutron. Since
neutrons near threshold have low velocity, centrifugal barrier effects
make the $\ell=0$ case the most probable. Integrating over energy in equation
3.4 for a target of finite thickness yields

$$Y \propto (E_{beam} - E_{th})^{3/2} \equiv \Delta E^{3/2} \quad . \qquad (3.5)$$

Therefore, a plot of (yield-background)$^{2/3}$ versus the beam energy E_{beam}
should be a straight line with intercept at the threshold energy E_{th}.
The background level was determined from a fit to the counts observed
below the threshold. The 3/2 power law is strictly true only for s-wave
neutrons and if there are no strong resonances near the threshold. The
good fits obtained (figures 3.10, 3.11) indicate that these requirements
were satisfied. Small corrections such as the Lewis effect or the effect
of beam energy spread were ignored in the analysis (Ma 66).

The negative ion source with the particular mixture of source
gas used (5% CO_2 and 95% H_2) produces two distinct oxygen beams. The
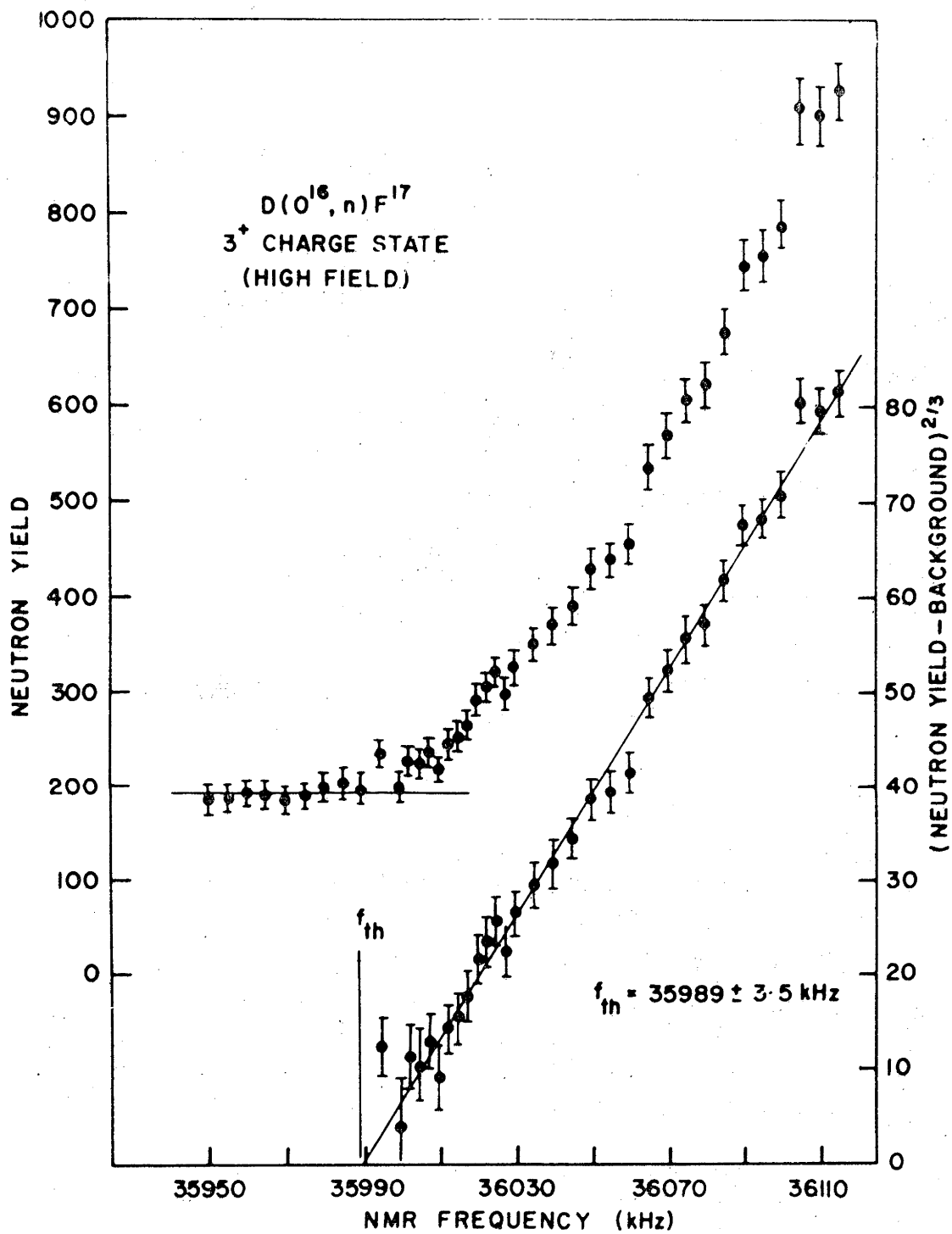
Figure 3.10. The $^2H(^{16}O,n)^{17}F$ neutron yield near threshold for an $^{16}O^{3+}$ beam. The 2/3-power of the net yield has been extrapolated to determine the threshold frequency.
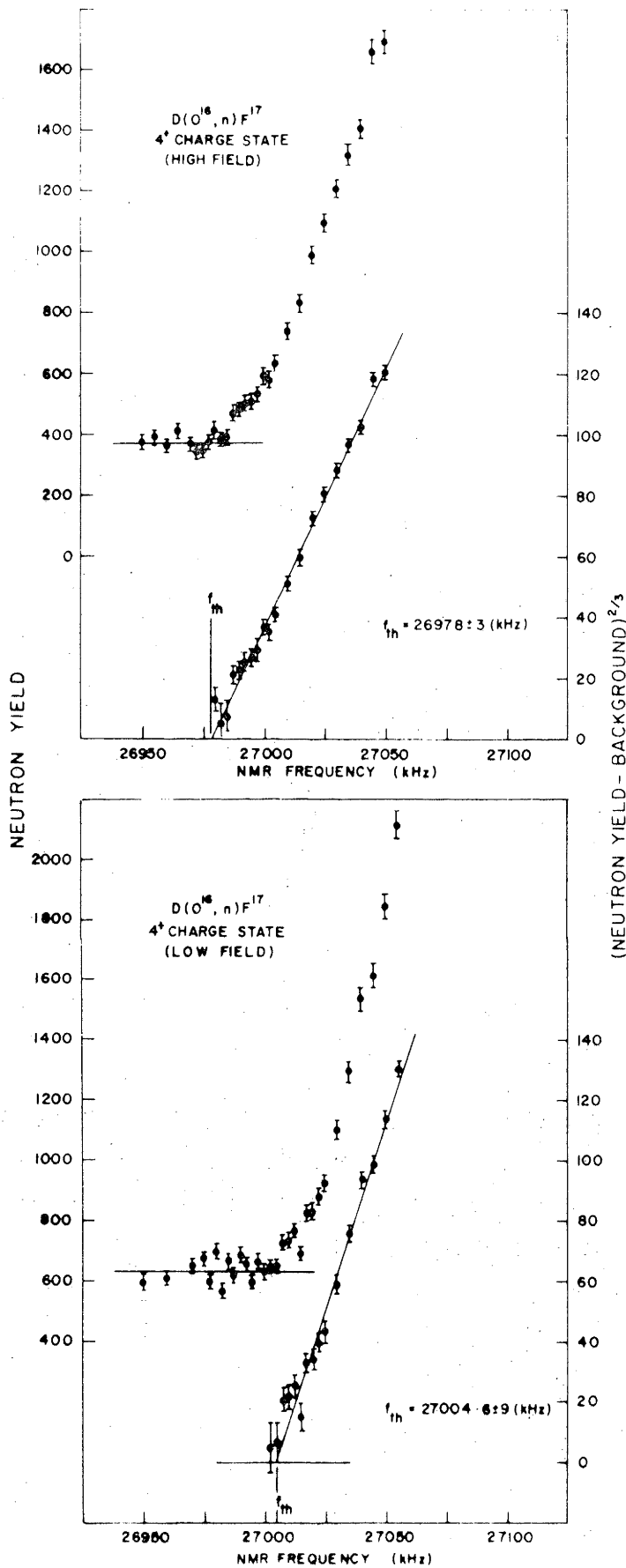
Figure 3.11. The $^2H(^{16}O,n)^{17}F$ neutron yield near threshold for $^{16}O^{4+}$ beams. The high and low field labels refer to the $20°$ magnet immediately in front of the ion source. The extrapolated 2/3-power of the net yield for the two cases indicate threshold frequencies which differ by about 25keV.

nature of these beams is uncertain. However, there is some evidence

which suggests that they are due to the breakup of (OX^{1^+}) molecules in

the gas exchange canal of the ion source, where X refers to the unknown

atom or a combination of atoms (see equation 3.1). The threshold yield

curves obtained with these two beams are shown in figure 3.11. The low

field beam (the field at the 20° magnet just after the ion source)

threshold was found to be about 25keV higher than the high field beam

measurement. These results are reproducible and were repeated several

times with altered machine parameters with similar outcome. Care was

taken, therefore, to use the same oxygen beam (high field) during the

reorientation measurements as was used for the final calibration of the

magnet.

c) Comparison of Back Scattered ^{4}He Beams with ^{212}Pb α-Sources

The availability of α-sources with accurately known energies

provides a convenient method for calibrating analyzing magnets. The

method consists of comparing the energy of scattered ^{4}He beams with

α-particle groups from a thin ^{212}Pb α-source. The experimental geometry

used in the present work is ideal for such measurements in that kinematic

energy variation with angle is minimal at angles close to 180°. Further-

more, the energy of the ^{4}He beams used in the reorientation measurements

can be directly determined during the experiment.

The calibration was performed by scattering ^{4}He beams from

targets of gold and aluminum. The gold target consisted of a thin layer

of gold ($\sim$5μg/cm^2) evaporated onto a carbon backing. The thickness of

the gold layer was determined from the Rutherford cross-section, as the

beam energy was below the Coulomb barrier. The aluminum target was a

self-supporting (10-15μg/cm^2) aluminum foil with a thin layer of ^{58}Ni

TABLE 3.1

A list of error estimates for the ^{4}He-beam/α-source comparison calibration of the analyzing magnet. The energy of the ^{212}Pb α line is 8785.0±0.08keV (Wa 64) and the mean scattering angle was 174.6$^{\text{o}}$.

Source of Uncertainty	Gold Target	Aluminum Target
A 6mm error in target-detector separation affects the calculated energy of the backscattered particle by:	± 0.5keV	± 2keV
Correction for target thickness	± 0.2keV	± 1keV
Peak centroid error	± 0.5keV	± 1keV
Calibration standard	± 0.08keV	± 0.08keV
Total Uncertainty	< ± 1keV	< ± 3keV

on one side; the aluminum thickness was determined from the shift in the ^{58}Ni elastic scattering peak, obtained by rotating the target through 180°. Nickel was used because it has a small coefficient of diffusion into aluminum, so that erroneous thickness measurements due to a diffuse region of nickel are avoided.

For a given target the nominal beam energy was chosen such that the elastic scattering peak overlapped with an α-line from the source. This procedure effectively eliminates the need for any corrections due to nonlinearities in the ADC. The beam intensity was kept small (~20nA) in order to avoid gain changes due to count rate effects, and the gain was monitored with a pulser. The accuracy of this method can be gauged from a list of error estimates given in table 3.1 for a typical measurement with both gold and aluminum targets.

d) Summary of Calibration Results

The relation between the calibration constant k of the analyzing magnet and the beam energy E is

$$k = (ME/f^2q^2) \left[1 + E/2Mc^2 \right] keV.u/Mhz^2 \quad , \tag{3.6}$$

where E is in keV, the N.M.R. frequency f is in Mhz and the mass of the particle M is the atomic mass less q electron masses expressed in a.m.u. The calibration constants obtained are shown in figure 3.12. Each point represents the average for several measurements. The errors shown include the uncertainty in calibration standards, the estimated uncertainty in the determination of the thresholds in the ^{16}O-^{2}H reaction, and the errors indicated in table 3.1 for the ^{4}He-beam/α-source measurements. The mean value of k is 19.957 ± 0.005, where the uncertainty was determined from the scatter of the data points.
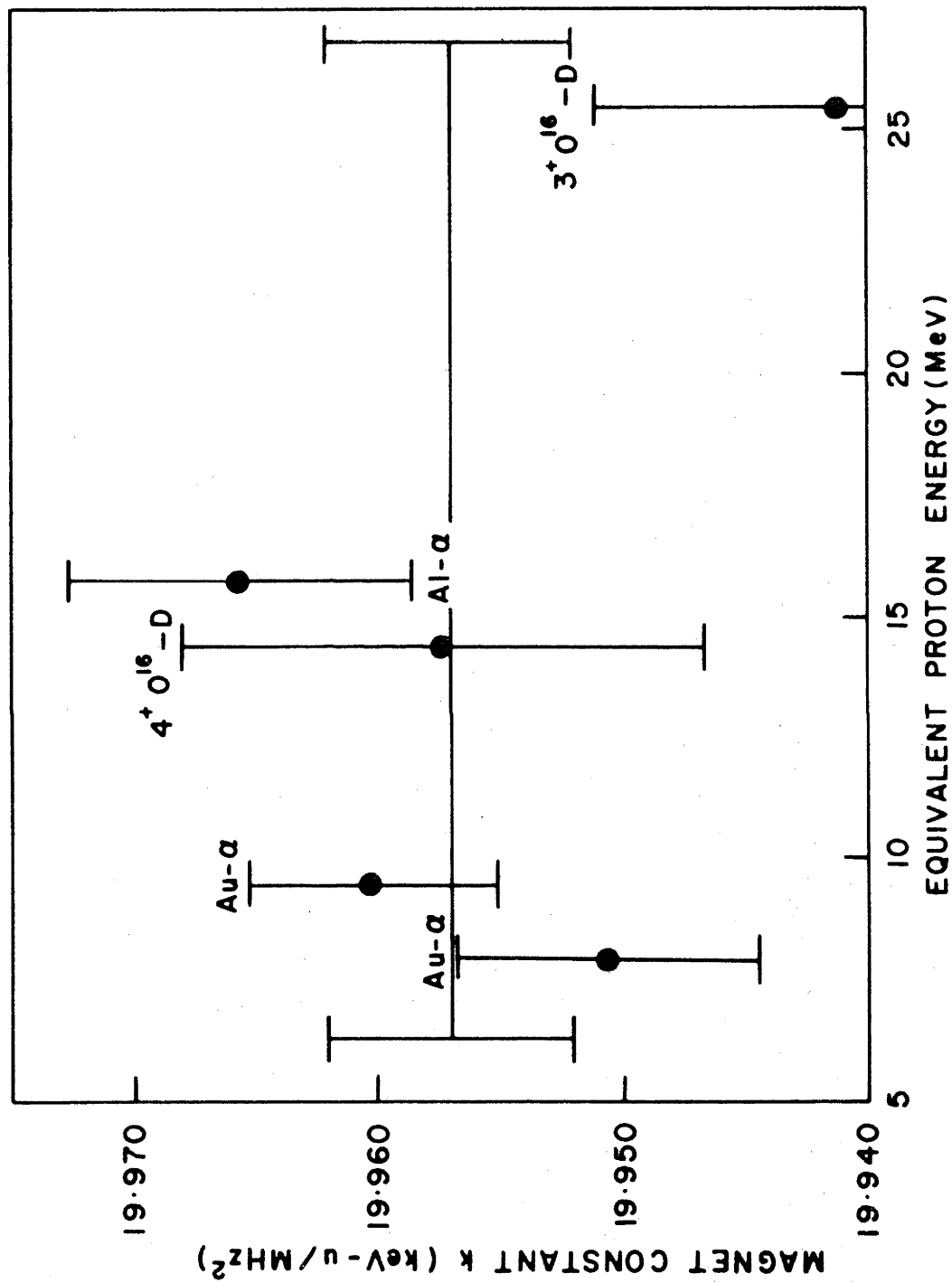
Figure 3.12. Magnet calibration constant k as a function of equivalent proton energy. The mean value and the standard deviation of k are indicated by the horizontal line and by the error bars at each end of the line.

From the calibration measurements outlined in sections (b) and (c) uncertainties assigned to the beam energy were 4keV for an 8MeV ^{4}He beam and 20keV for a 40MeV ^{16}O beam. The bombarding energy was corrected for energy loss in the CdCl$_2$ target material and in its protective carbon layer. It will be seen that these corrections, discussed earlier in section 3.4, were less than the uncertainty in accelerator energy calibration.

3.7 Electronics

As only one detector was involved and only relative intensities were required, the electronic equipment was very simple. It consisted of a preamplifier (Ortec model 109A or 125), amplifier (Tennelec TC125BLR), and an ADC (Canberra 8060). The data were collected in an on-line IBM 1800 computer and stored on magnetic disks. In the ^{4}He data high count rates due to scattering from the carbon backing produced pulse pile-up which can be seen (fig. 4.1, chapter 4) as a flat "background" on the high energy side of the cadmium elastic peak. Lower than optimum time constants were used in the amplifier to minimize pile up. No additional pile-up rejection circuitry was used to reduce this background as such devices were found to distort spectral line shapes and in any case errors in the ratio of peak intensities due to pulse pile-up were small compared with statistical uncertainties (see chapter 4).

CHAPTER 4.

DATA REDUCTION AND ANALYSIS

The extraction of quadrupole moments from the data, obtained

using the methods described in chapter 3, requires the comparison of

excitation probabilities for ^{4}He and ^{16}O projectiles (see section 2.7b).

The experimentally determined Coulomb excitation probability R_{exp} of the

2^+ state is defined as

$$R_{exp} = (d\sigma/d\Omega)_{2^+}^{lab} / \left((d\sigma/d\Omega)_{2^+}^{lab} + (d\sigma/d\Omega)_{0^+}^{lab} \right) \quad . \qquad (4.1)$$

Surface-barrier-detector spectral-line-shapes for ^{4}He and ^{16}O projectiles

are quite different (fig. 4.1). Systematic errors associated with deter-

mining the elastic and inelastic cross sections from these spectra will,

therefore, also be different. Elucidation of the systematic errors

ultimately depends on accumulating sufficient statistics on the behaviour

of R_{exp} for different analysis procedures. Several methods were devised

for extracting the elastic and inelastic cross sections from the two sets

of data with the aim of determining the sensitivity of R_{exp} to these

procedures. They are described below.

4.1 Analytic Lineshapes

The lineshapes of both ^{4}He and ^{16}O spectrum peaks are non-

symmetric (fig. 4.1). The high energy profiles in both can be matched

closely with a Gaussian function. In ^{4}He spectra the low energy side of

the lineshape initially has a Gaussian form down to about 5% of the peak

height, after which, it evolves into a complex shape. In a logarithmic

plot the tail appears curved and smoothly merges into the background

(see fig. 4.1). The observed curvature in the logarithmic plot indicates

that the tail profile can be analytically reproduced, in general, as an

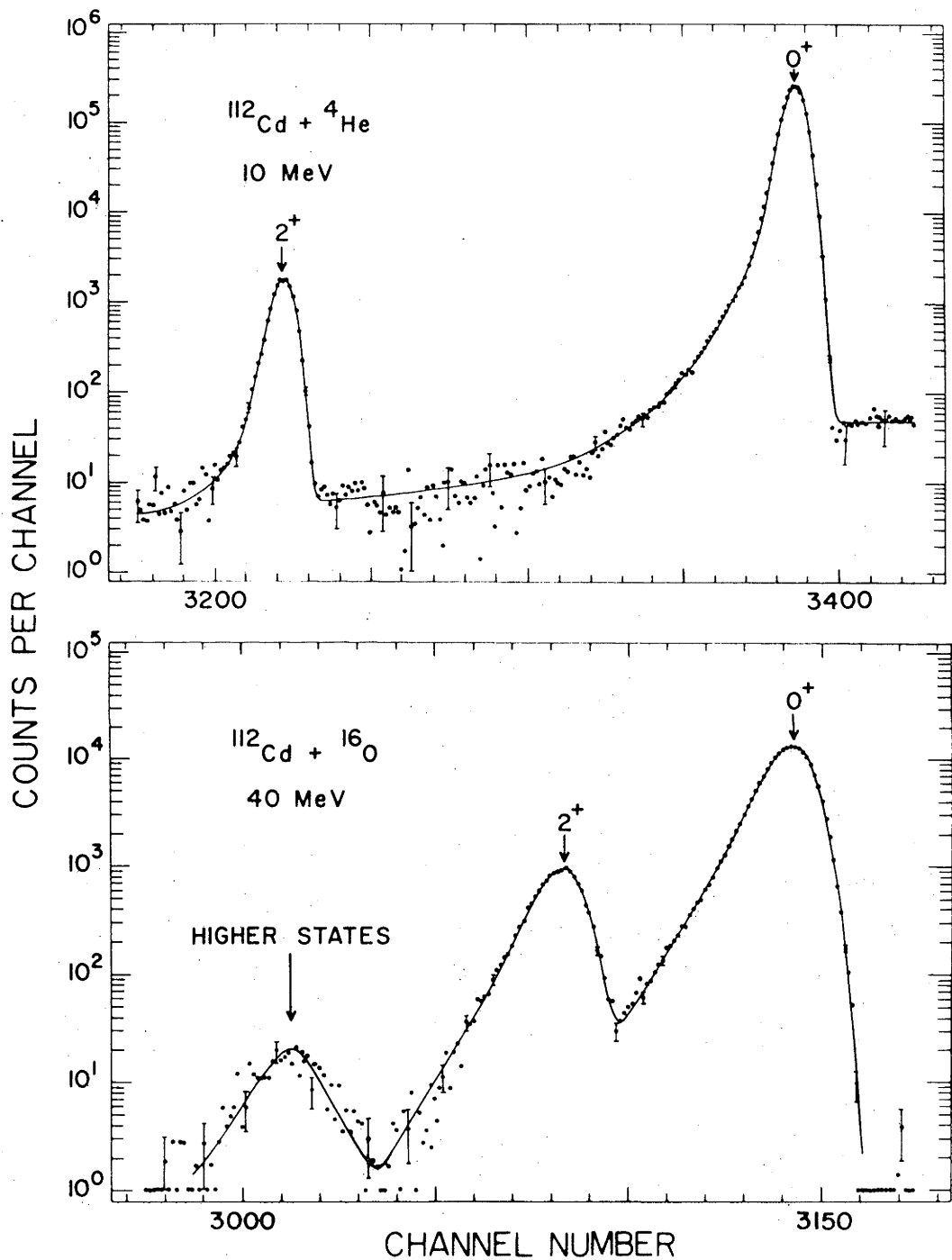Figure 4.1. Spectra of 10MeV ^{4}He and 40MeV ^{16}O ions scattered from ^{112}Cd for θ_{lab}=171.6° and 174.6° respectively. Contributions from other isotopes have been subtracted from the data. The full curves are least-squares fits to the data.

exponential function with a polynomial argument of the form

$$\exp(-|aZ + bZ^2 + \ldots |) \quad . \tag{4.2}$$

For a given channel x, $Z = (x-x_p)$, where x_p is the number of the channel containing maximum counts. It was found, however, that the tail profile in ^{4}He spectra could be reproduced satisfactorily with a simpler function:

$$\exp(-|Z|^{a_5}) \quad , \tag{4.3}$$

where a_5 is a variable.

In contrast to ^{4}He spectra, the low energy tail in ^{16}O line-shapes can be matched quite well with an exponential function

$$\exp(-a|Z|) \quad , \tag{4.4}$$

which appears as a straight line in a logarithmic plot; see, for example, the low energy tail of the ^{112}Cd 2^+ peak visible in the ^{16}O spectrum shown in figure 4.1. It is not clear, however, that this tail shape provides an accurate representation of that portion of the elastic lineshape which lies below the 2^+ peak. To investigate this point an elastic ^{16}O line-shape was obtained from an enriched ^{118}Sn target. The first excited stated of ^{118}Sn is sufficiently high to reveal the shape of that part of the elastic tail not visible in cadmium spectra. A fit to the tin line-shape is shown in figure 4.2. The tail was fitted with the exponential function given in equation 4.4. The good fit obtained lends credence to the assumed analytic shape; similar results have been obtained by other workers (see, for example, Berant et al., Be 72).

To unfold the elastic and the inelastic peaks in ^{16}O spectra a computer program was constructed incorporating a Gaussian function for the high energy side and a skewed Gaussian with an exponential tail for
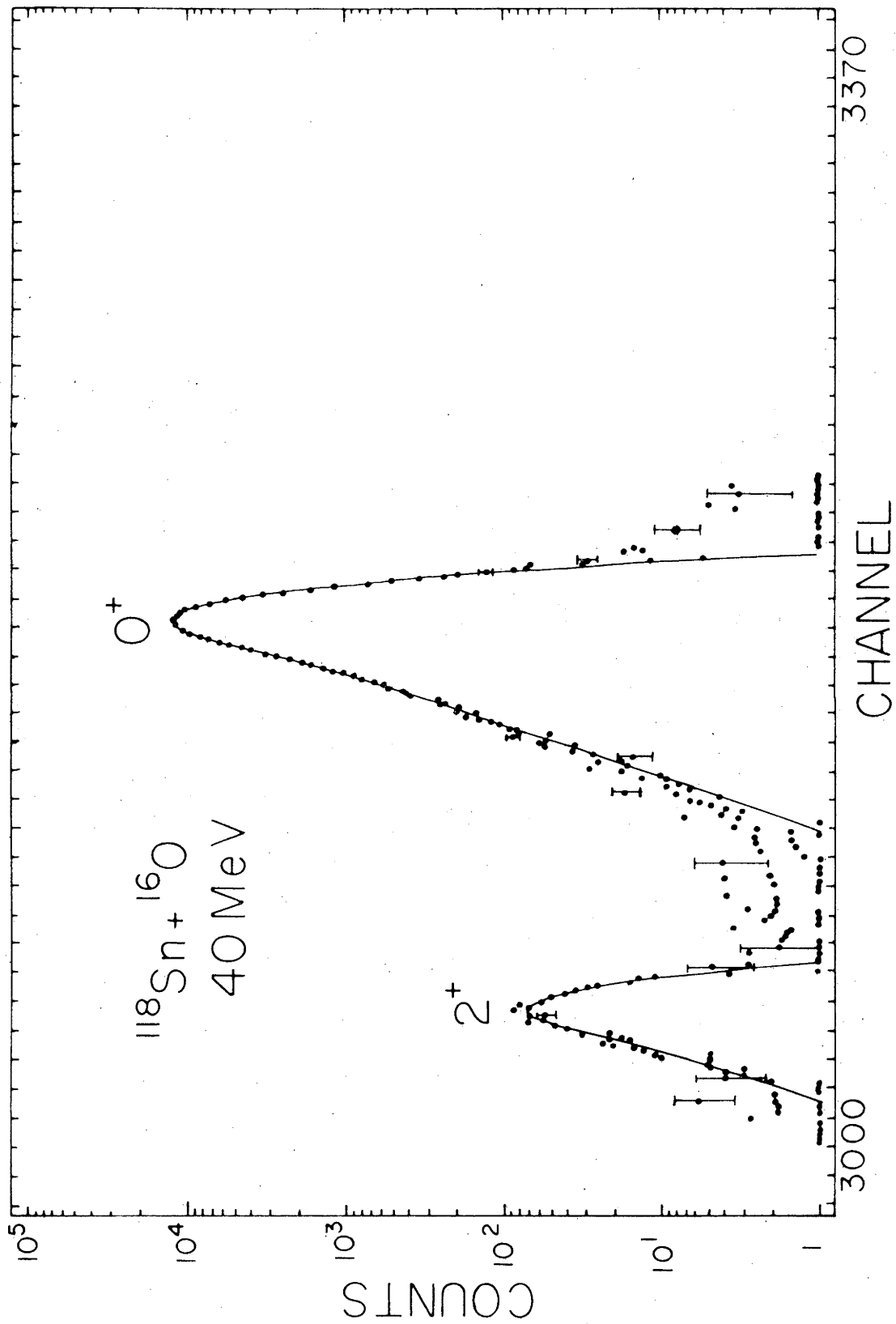
Figure 4.2.   Spectrum of 40MeV ^{16}O ions backscattered from an enriched ^{118}Sn target. The solid line represents a fit to the spectrum.

the low energy side. With the inclusion of an additional parameter, a_5, as in equation (4.3), ^{4}He lineshapes could be reproduced as well. The latter were useful, in particular, for subtracting isotopic impurities (section 4.4) and also for comparison with other methods of determining R_{exp} from ^{4}He spectra (see section 4.2). The analytic function used had the explicit form

$$S(x-x_p) = \exp\left(-(x-x_p)^2/a_1^2\right) \quad \text{for } x \geqslant x_p \quad , \tag{4.5}$$

$$= \exp\left(-(x-x_p)^2/a_2^2\right) + a_3 \exp\left(-a_4 (x-x_p)^{a_5}\right)$$

$$\left[1 - \exp\left(-(x-x_p)^2/a_3^2\right)\right] \text{ for } x < x_p \quad . \tag{4.6}$$

The spectrum was then represented by a sum over the number of peaks p:

$$I(x) = \sum_p A_p S(x-x_p) \quad . \tag{4.7}$$

Here a_1 and a_2 represent the high energy and low energy half-peak widths, repectively, at a distance of $A_p e^{-1}$ from the maximum of the peak. Parameters a_3 and a_4 govern the amplitude and decay rate of the tail and a_5 was set equal to 1 for ^{16}O spectra.

The nonlinear least squares fitting program uses the Levenberg-Marquardt algorithm (Le 44, Be 69) and requires the derivatives of the function I with respect to each of the variable parameters a_i, x_p and A_i. The program has provision to fit three peaks with 11 simultaneously variable parameters. It was found that an initial rough fit to the spectrum peaks with the various parameters entered manually and the results monitored on a display speeded the computer fit considerably.

In the ^{4}He spectra, an exponential background term of the form $\exp(a-bx)$ was included in addition to function I. The parameters a and b were determined by a fit to the background counts on either side of the

2^+ peak and outside the range of the low energy tails of both the elastic

and inelastic peaks. The pile-up region visible on the high energy side

of the elastic peak in ^{4}He spectra was simulated by assuming that it was

due to a roughly constant level of noise. The contribution to the spectrum

at channel x_n as a result of the simultaneous detection of elastically

scattered alphas from cadmium and from the "noise" region can be repre-

sented by: (constant) x $\sum x_i x_j$, where the summation is over the noise

region (channels x_j) and the cadmium elastic peak (channel x_i) up to

channel x_n. The assumption of constant noise level (i.e. $x_j \sim$ constant)

is reasonable in order to reproduce the pile-up region under and

immediately (~100keV) to the right of the elastic peak. The pile-up at

channel x_n is then given by

$$P(x_n) = N \sum_{i=m}^{n-1} x_i \quad , \qquad (4.8)$$

where x_m is some convenient starting point, about halfway between the

elastic and 2^+ peaks. The magnitude of N was determined by a fit to the

pile-up region visible on the high energy side of the elastic peak. The

pile-up pulses under the elastic and inelastic peaks were estimated to

be less than 0.2% of their peak areas in the worst case and their contri-

bution is therefore negligible. The pile-up term $P(x_n)$ (equation 4.8)

for the worst case encountered is shown in figure 4.3 together with a fit

to the background. A complete fit to the same spectrum is also shown in

this figure. Additional methods of analysis of ^{4}He and ^{16}O spectra will

be considered separately below.

4.2 The ^{4}He Data

The 2^+ peak, which is typically less than 1% of the elastic

intensity, is well resolved and sits on an almost flat background. There-

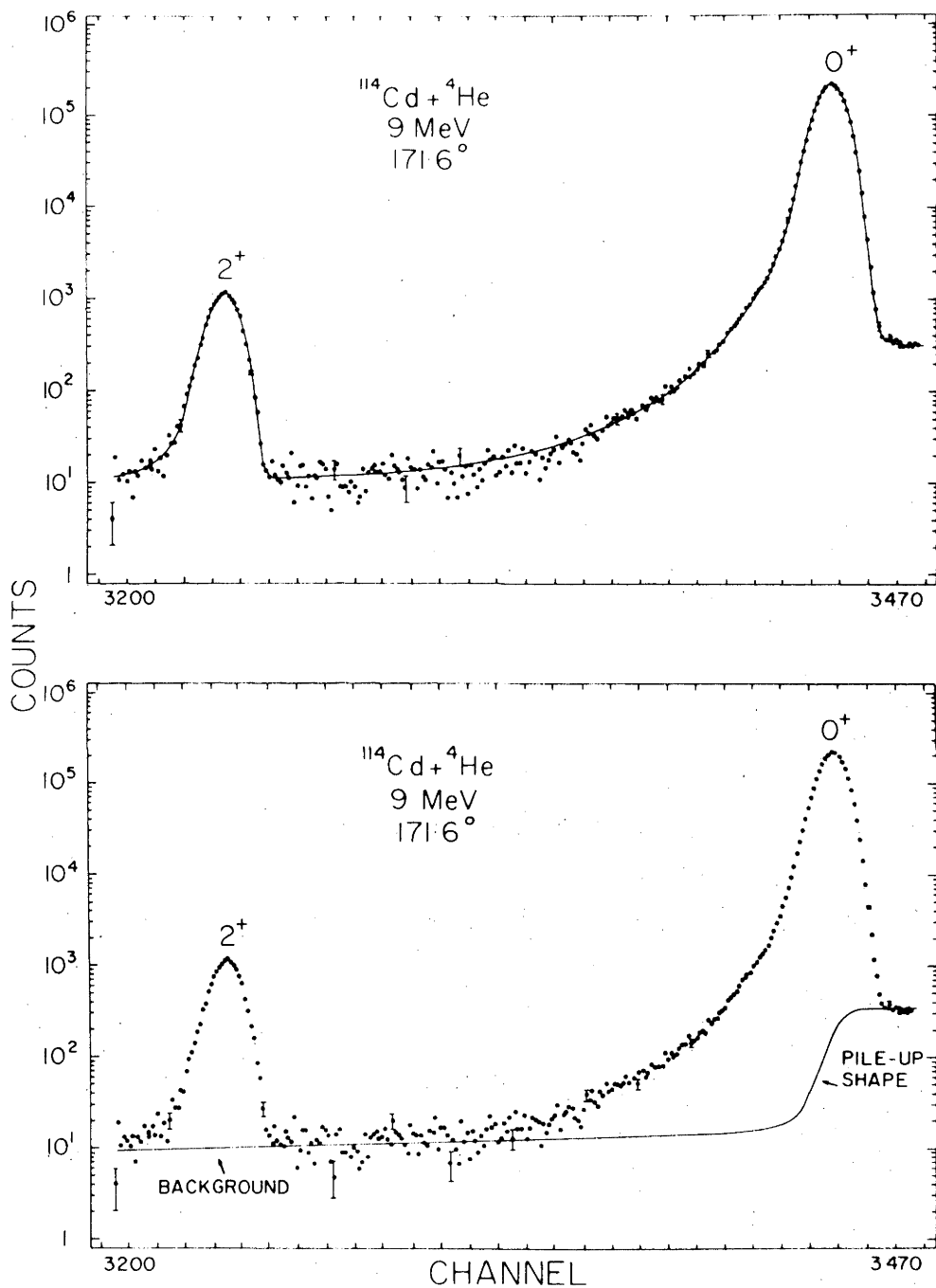fore, linear background subtraction, by fitting a straight line to the

Figure 4.3. Spectra of 9MeV ^{4}He ions backscattered from ^{114}Cd.
A fit to the whole spectrum as well as the background
and pile-up components of the analytic lineshape are
shown.

background counts on either side of the 2^+ peak, can be used to obtain

the number of counts in the 2^+ peak. The elastic peak area was extracted,

in a similar manner by summing over the same number of channels, relative

to its centroid, as used for the 2^+ peak. The ^{4}He spectra were also

analyzed using analytic lineshapes as described in section 4.1. In most

of these the curvature of the low energy tail could be accurately reproduced.

In others the tail curvature was non-uniform and the data oscillate round

the best fit line (see figures 4.1, 4.3, 4.4 and 4.5). However, for all

of the ^{4}He data the agreement between the results obtained with analytic

lineshape fits and those obtained by the linear background subtraction

method was better than 0.5%. The systematic uncertainty in R_{exp} arising

from the fitting procedure was therefore taken to be 0.5%.

4.3   The ^{16}O Data

The relative number of counts in the overlapping elastic and

inelastic peaks in the ^{16}O data was extracted using two methods. The

basic problem lies in determining the shape and magnitude of the elastic

peak tail extending under the inelastic peak to sufficient accuracy that

the 2^+ peak area can be determined to better than about 1% (including

the statistical error). For the worst case encountered the number of

counts in the elastic tail beneath the inelastic peak is less than 4%

of the counts in the inelastic peak. The 2^+ yield can therefore be

determined to about 1% if the unfolding procedure is accurate to within

20%. For most of the data, however, the tail contribution is about 2.5%.

The peaks were unfolded using the analytic shape given in

equations 4.5 and 4.6 with parameter a_5 = 1. Excellent fits were obtained

(e.g. see figures 4.1 and 4.4). The tin lineshape (see section 4.1 and

fig. 4.2) was also used, with only the peak positions x_p and heights A_p
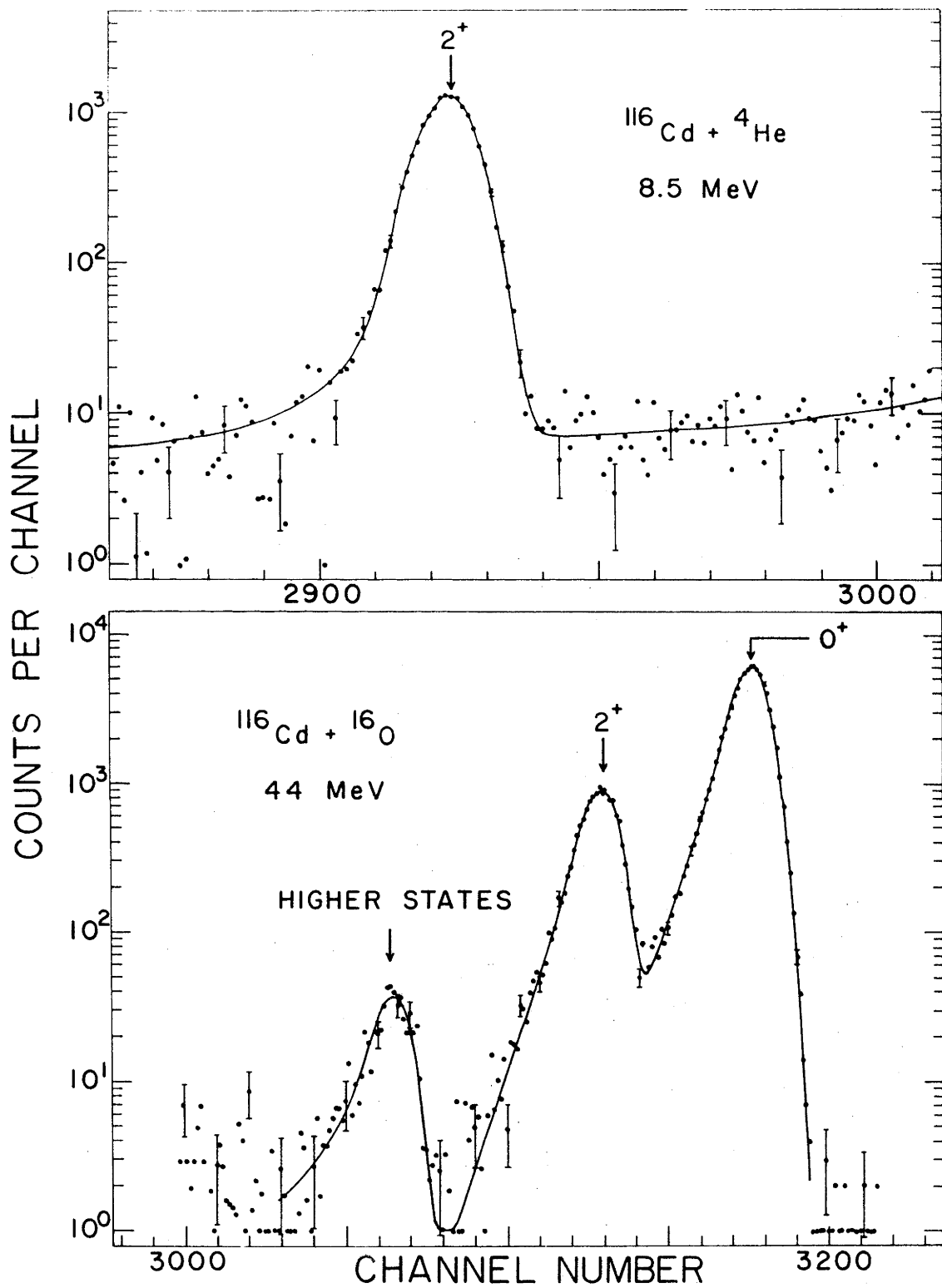
Figure 4.4. Spectra of 8.5MeV ^{4}He and 44MeV ^{16}O ions scattered from ^{116}Cd for θ_{lab}=171.6° and 174.6°, respectively. Contributions from other isotopes have been subtracted from the data. The lines through the data points show least-squares fits to the spectra.

Figure 4.5. Spectrum of 9MeV ^{4}He projectiles backscattered from ^{108}Cd. The low energy tail of the elastic peak "oscillates" about the fitted lineshape.

being allowed to vary in the fitting procedure. A typical fit obtained

in this way is shown in figure 4.6. The fit is not as good as that

obtained with the analytic lineshape where the tail and width parameters

(equations 4.5, 4.6) are also variable; this is due to the difference in

thickness and uniformity between the tin and cadmium targets used. However,

the two unfolding procedures always gave the same value for R_{exp} to within

0.5%.

As an additional check of the overall reliability of the fitting

procedure, R_{exp} was extracted using the experimental data points (as opposed

to the analytic fit) except in the region of overlap, where the fitted line-

shape was used. The two methods agreed to within about 0.1%. Furthermore,

in several cases spectra obtained at the same bombarding energy but

differing in peak-to-valley ratio by factors of two were analyzed. The

agreement was within the statistical error of 0.8%. A systematic uncer-

tainty of 0.8% was therefore conservatively assigned to the extraction of

excitation probabilities from the ^{16}O spectra.

4.4   Isotopic Contaminants

The isotopic enrichment of the target material, for all of the

cadmium isotopes studies, is listed in table 4.1. The elastic lineshape

obtained from the main isotope was used in conjunction with the supplier's

assay to subtract both the elastic and inelastic isotopic contaminants.

Initially the inelastic cross sections were calculated using the first

order perturbation theory formulae (see chapter 2). The B(E2) values were

obtained from the compilation of Christy and Häusser (Ch 72). It was

found, however, that 15-20% differences could occur between the first

order theory and the results from the de Boer-Winther program (Wi 66).

Subsequently this program was used to calculate the inelastic cross
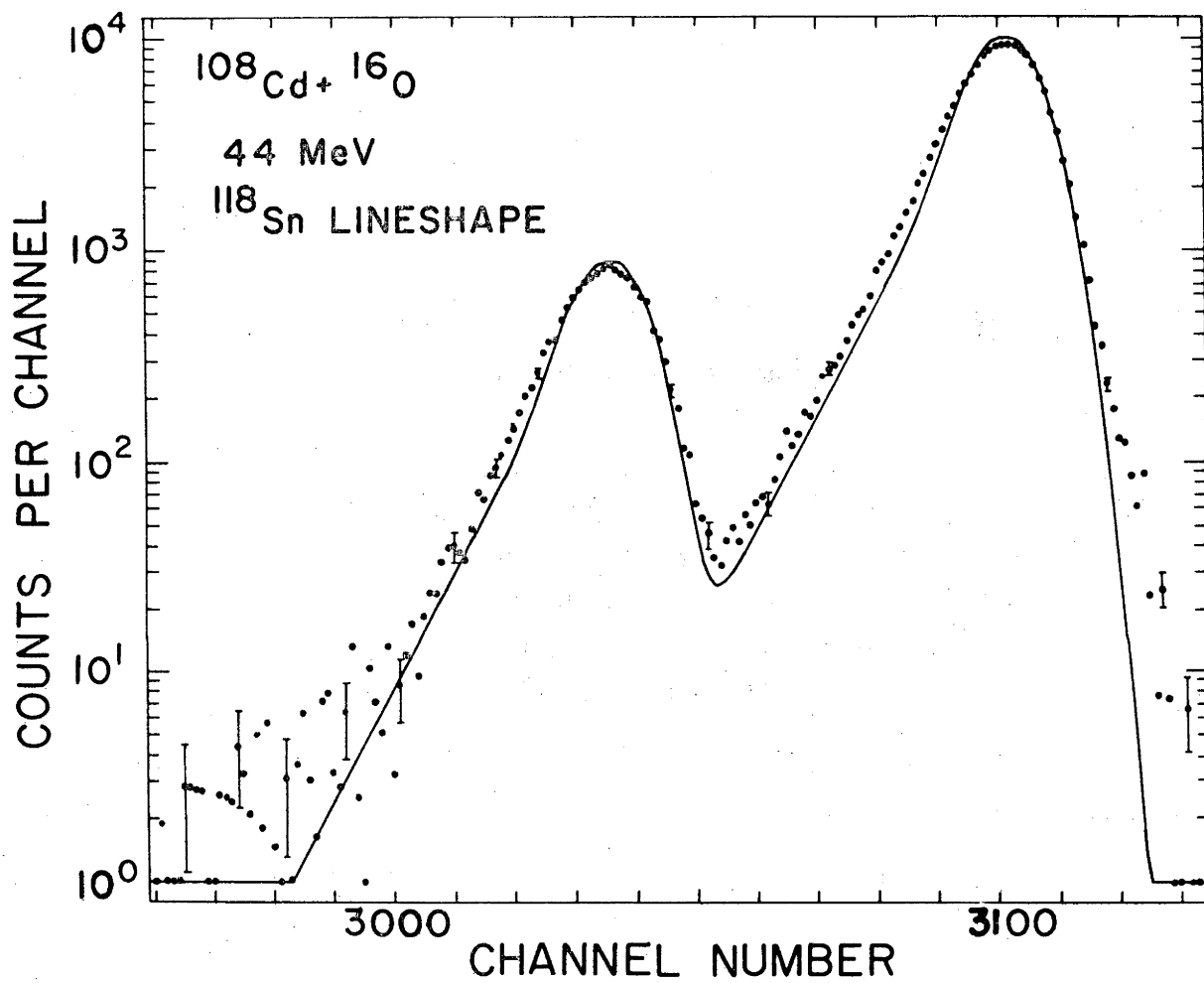
Figure 4.6. Spectrum of 44MeV ^{16}O ions backscattered from ^{108}Cd.
The full curve shows a fit to the data using the
lineshape obtained from an enriched ^{118}Sn target;
only the peak positions and heights were allowed
to vary in the fitting procedure.

Table 4.1. Isotopic compositions of the cadmium targets used in the present work. The material was obtained from Oak Ridge Separated Isotopes Division.

Target / Impurity	106	108	110	112	114	116
106	82.33±0.10	0.57±0.03	<0.01	0.04±0.02	<0.02	<0.02
108	0.82±0.01	73.68±0.20	<0.01	0.03±0.02	<0.02	<0.02
110	2.93±0.03	5.63±0.05	97.20±0.05	0.20±0.02	0.10±0.02	0.18±0.01
111	2.64±0.02	4.10±0.05	1.04±0.05	0.59±0.02	0.12±0.02	0.20±0.01
112	3.68±0.03	6.58±0.05	0.90±0.05	96.97±0.08	0.32±0.02	0.46±0.01
113	1.72±0.02	2.67±0.04	0.27±0.02	1.26±0.03	0.47±0.03	0.56±0.01
114	3.85±0.03	5.33±0.05	0.49±0.02	0.80±0.03	98.80±0.08	4.30±0.05
116	2.01±0.02	1.44±0.03	0.09±0.02	0.11±0.02	0.18±0.02	94.30±0.06

sections. These were then parametrized in terms of the bombarding energy over the energy interval of interest. The matrix elements for the inelastic transitions in the isotopes ^{111}Cd and ^{113}Cd were obtained from Nuclear Data Sheets (Ra 71, Ra 71a) and are shown in figure 4.7 together with the low-lying level scheme for these isotopes. The contributions of impurity isotopes were subtracted according to the following recipe.

The total number of counts C in a given spectrum due to scattering from the cadmium isotopes can easily be determined by summing over the appropriate region. In ^{16}O spectra there is no significant background; in ^{4}He spectra C was determined after subtracting the background and the contribution from pile-up pulses (see fig. 4.3). The number of counts C can be expressed as

$$C = k \times \sum_i f_{OR}(i) \times \left[\sum_j (d\sigma_j/d\Omega)_{gs \to j} \right]_i \quad , \quad (4.9)$$

where j is the index of levels included for each isotope and i is the index of the isotopes present in the spectrum. The cross sections $(d\sigma_j/d\Omega)_{gs \to j}$ from ground state (gs) to level j were calculated as explained above. The normalization constant k can be determined from equation (4.9) knowing the fraction f_{OR} of each impurity (here OR refers to the Oak Ridge assay). The elastic peak from the main isotope was then fitted with an analytic line-shape. The number of counts in each channel of this lineshape was divided by the total number of counts in the fitted peak giving

(Elastic lineshape)/(number of counts in it)

$$\equiv \text{Lineshape with unit area (ULS)} \quad . \quad (4.10)$$

If the inelastic cross section for the main isotope was zero, the number of counts in each channel of the elastic peak (ELP) would have been

$$(ELP) = (ULS) \times k \times f_{OR}^{MI} \times \left[\sum_j (d\sigma_j/d\Omega)_{gs \to j} \right]_{MI} \quad , \quad (4.11)$$

0	-0.068	-0.424	-0.51	-0.25
-0.068	0	0	0	0
0.424	0	0	0	0
-0.51	0	0	0	0
0.25	0	0	0	0

$$
\begin{array}{lll}
5 & \underline{\quad 0.754 \quad} & 3/2^{+} \\
4 & \underline{\qquad\qquad} & 5/2^{+} \\
  & 0.62 & \\
\end{array}
$$

$$
\begin{array}{lll}
3 & \underline{\quad 0.342 \quad} & 3/2^{+} \\
2 & \underline{\qquad\qquad} & 5/2^{+} \\
  & 0.245 & \\
\end{array}
$$

$$
\begin{array}{lll}
1 & \underline{\quad\quad 0 \quad\quad} & 1/2^{+} \\
\end{array}
$$

^{111}Cd
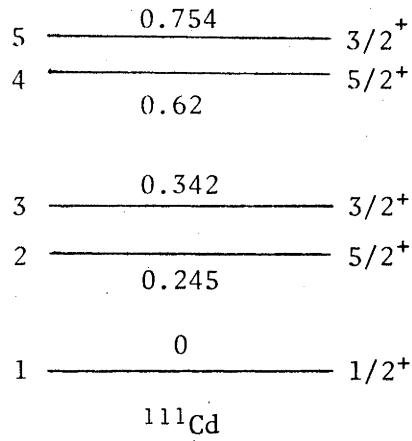
0	-0.469	-0.78	-0.42
0.469	0	0	0
-0.78	0	0	0
0.42	0	0	0

$$
\begin{array}{lll}
4 & \underline{\quad 0.675 \quad} & 3/2^{+} \\
3 & \underline{\qquad\qquad} & 5/2^{+} \\
  & 0.584 & \\
\end{array}
$$

$$
\begin{array}{lll}
2 & \underline{\quad 0.299 \quad} & 3/2^{+} \\
\end{array}
$$

$$
\begin{array}{lll}
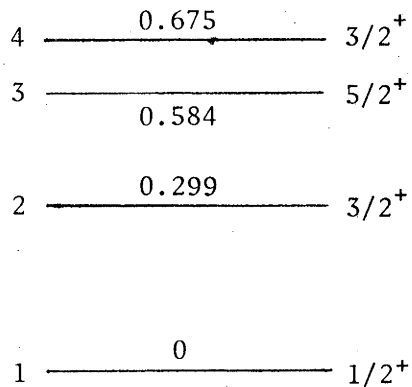1 & \underline{\quad\quad 0 \quad\quad} & 1/2^{+} \\
\end{array}
$$

Figure 4.7. The energy levels and reduced matrix elements used in the subtraction of odd-mass cadmium isotopic impurities from the data.

where MI refers to the main isotope. The lineshape and magnitude of each impurity peak j for a given isotope i is then

$$(\text{ELP}) \times f_{OR}^i \times (1/f_{OR}^{MI}) \times (d\sigma_j/d\Omega)_{gs \to j} \ / \left[\sum_j (d\sigma_j/d\Omega)_{gs \to j} \right]_i \ . \quad (4.12)$$

Equations (4.9) through (4.12) form the basis for subtracting each elastic and inelastic cadmium impurity peak from the spectra. The procedure followed was

a) The elastic lineshape of the main isotope was determined by a fit to the raw spectrum. In some cases this lineshape was distorted due to the effect of impurity peaks under the elastic peak. Therefore, this initial fit is only a first approximation to the proper lineshape.

b) The impurities were subtracted from the raw spectrum with a computer program utilizing equations (4.9) through (4.12). The subtraction process was visually monitored on a display screen and for those impurities which were resolved from the main elastic peak, the residual spectrum, after subtraction, was checked for any systematic trend. In all cases the sum of the residual counts was always within the errors quoted by Oak Ridge. An example is shown in figure 4.8, with the spectrum elevated on a pedestal of 100 counts.

c) The residual spectrum was again fitted with an analytic lineshape and step b) repeated until the last fitted lineshape did not differ, within statistical errors, from the previous one.

In all cases where the impurity isotopes could be resolved the supplier's assay was found to be in very good agreement with our data. An example is shown in figure 4.9 for ^{106}Cd, where most of the contaminant isotopes are resolved from the ^{106}Cd elastic peak. The good agreement lends confidence to the subtraction of impurities which are not resolved, e.g. in
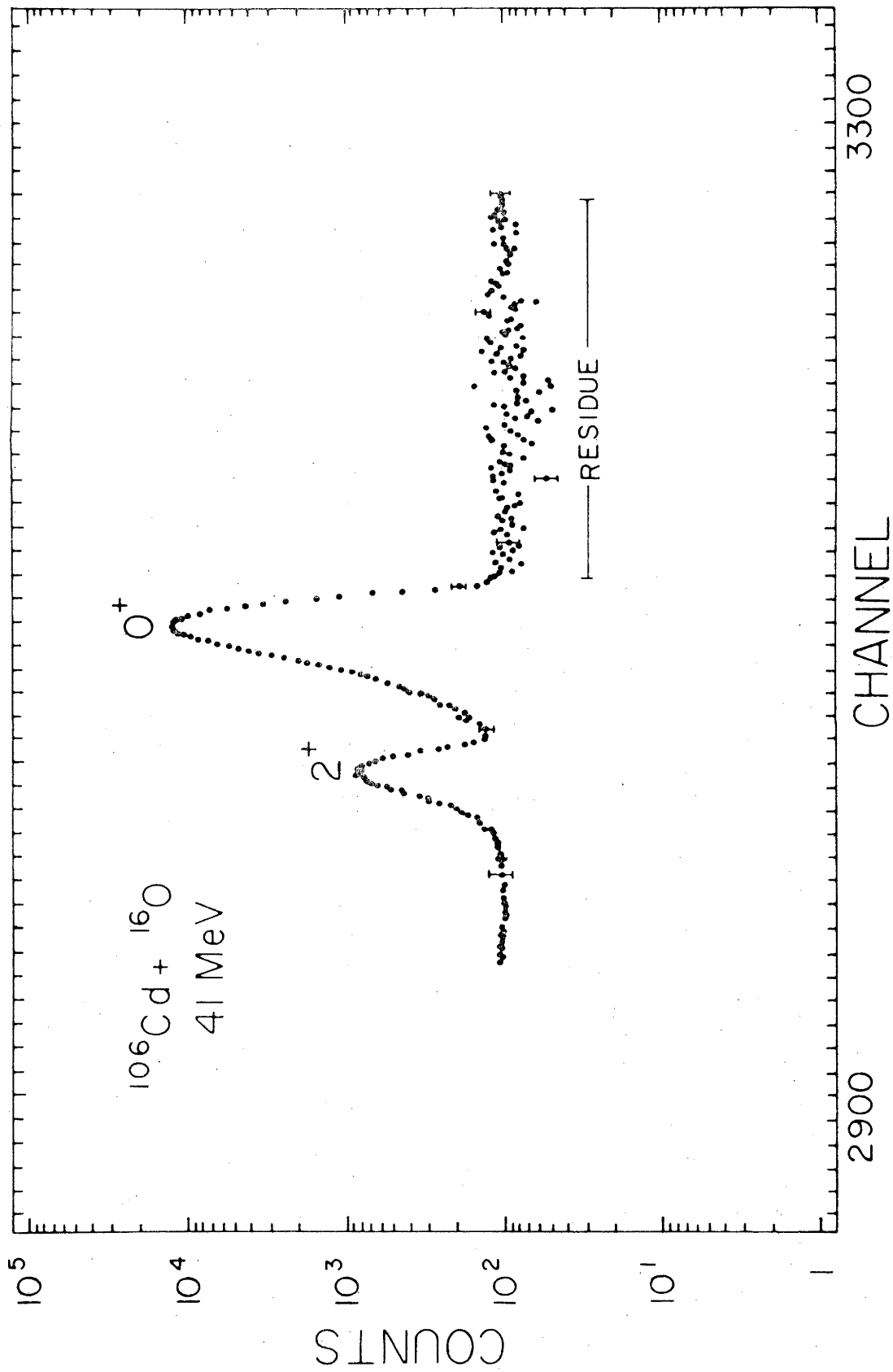
Figure 4.8. Spectrum of 41MeV ^{16}O ions backscattered from ^{106}Cd. The spectrum has been elevated on a pedestal of 100 counts. The residual counts after the subtraction of isotopic impurities show no systematic trend.
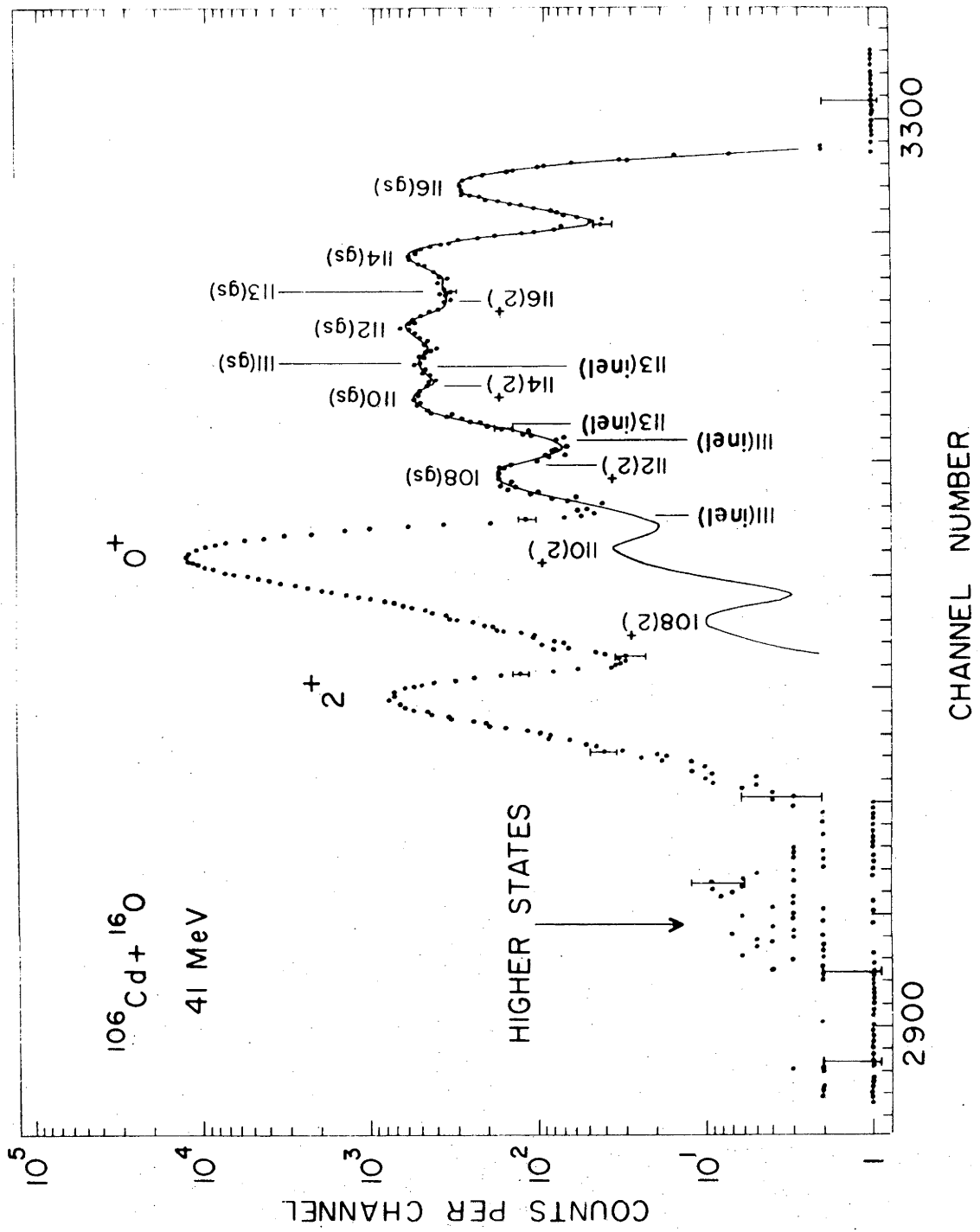
Figure 4.9.

Spectrum of 44MeV ^{16}O ions back-scattered from ^{106}Cd. The full curve shows contribution from isotopic contaminants calculated assuming the abundances given by the supplier of the target material.

Figure 4.10. Spectrum of 44MeV ^{16}O ions backscattered from ^{116}Cd. The full curve shows contributions from isotopic contaminants calculated assuming the abundances given by the supplier of the target material.

Figure 4.11. Spectra of 10MeV and 9.5MeV ^{4}He ions backscattered from ^{106}Cd and ^{112}Cd respectively. The full curves show the contributions from isotopic contaminants calculated assuming the abundances given by the supplier of the target material.

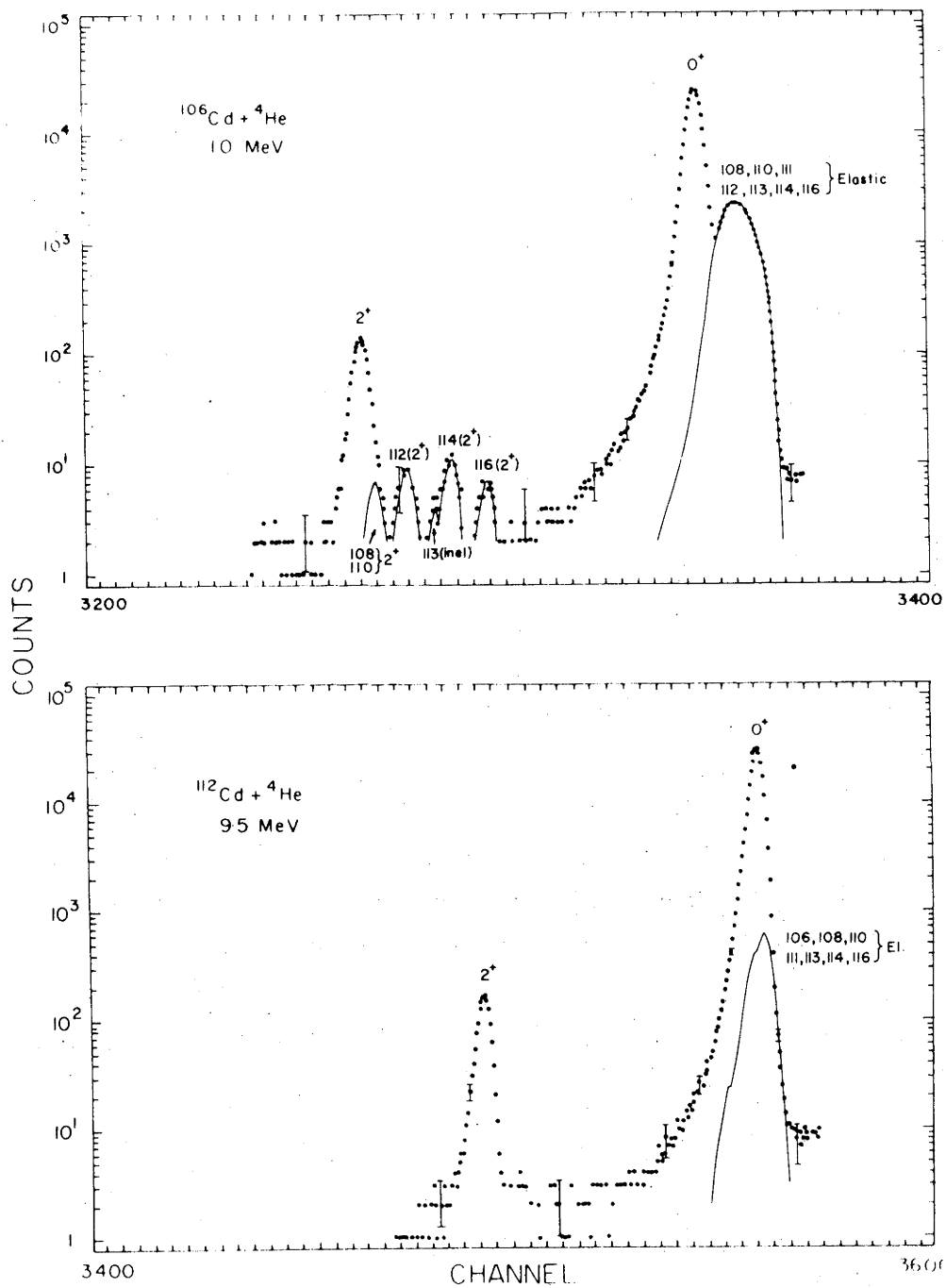^{116}Cd + ^{16}O data where ^{112,113,114}Cd elastic impurities interfere with the ^{116}Cd inelastic peak (see fig. 4.10). In this case an additional uncertainty of 0.2% was included in the extracted excitation probability corresponding to the isotopic analysis error quoted by the suppliers (table 4.1). Examples of ^{4}He spectra treated in a similar manner are shown in figure 4.11.

4.5 Safe Bombarding Energy

Coulomb-nuclear interference effects can severely distort the results of reorientation experiments carried out at too high a bombarding energy. The quadrupole moment obtained diverges rapidly from the true value if data obtained at energies above the barrier are included in the analysis. The maximum safe bombarding energy may be defined as the energy at which the nuclear contribution is no greater than 1% of the total cross section. The Coulomb barrier in ^{114}Cd has been studied extensively with ^{4}He projectiles, because of discrepancies among the various measurements of the B(E2, $0^+ \rightarrow 2^+$) value in ^{114}Cd. Some of these differences were attributed to the use of too high bombarding energies. A list of these experiments in which the Coulomb barrier was investigated in ^{114}Cd and also in the other cadmium isotopes is given in table 4.2 together with the results obtained.

In the present work, ^{4}He spectra were obtained for ^{114}Cd at energies up to 14MeV. The results for the variation of the elastic and inelastic cross sections with bombarding energy are shown in figure 4.12. The elastic cross section was normalized to the integrated charge and is expected to be accurate to only within ±5%. Nevertheless the sum of the elastic and inelastic cross sections relative to Rutherford is constant up to about 10MeV. Beyond this energy the relative cross section drops

Table 4.2. A list of experiments in which the Coulomb barrier in the cadmium isotopes have been determined for backscattered ^{4}He projectiles.

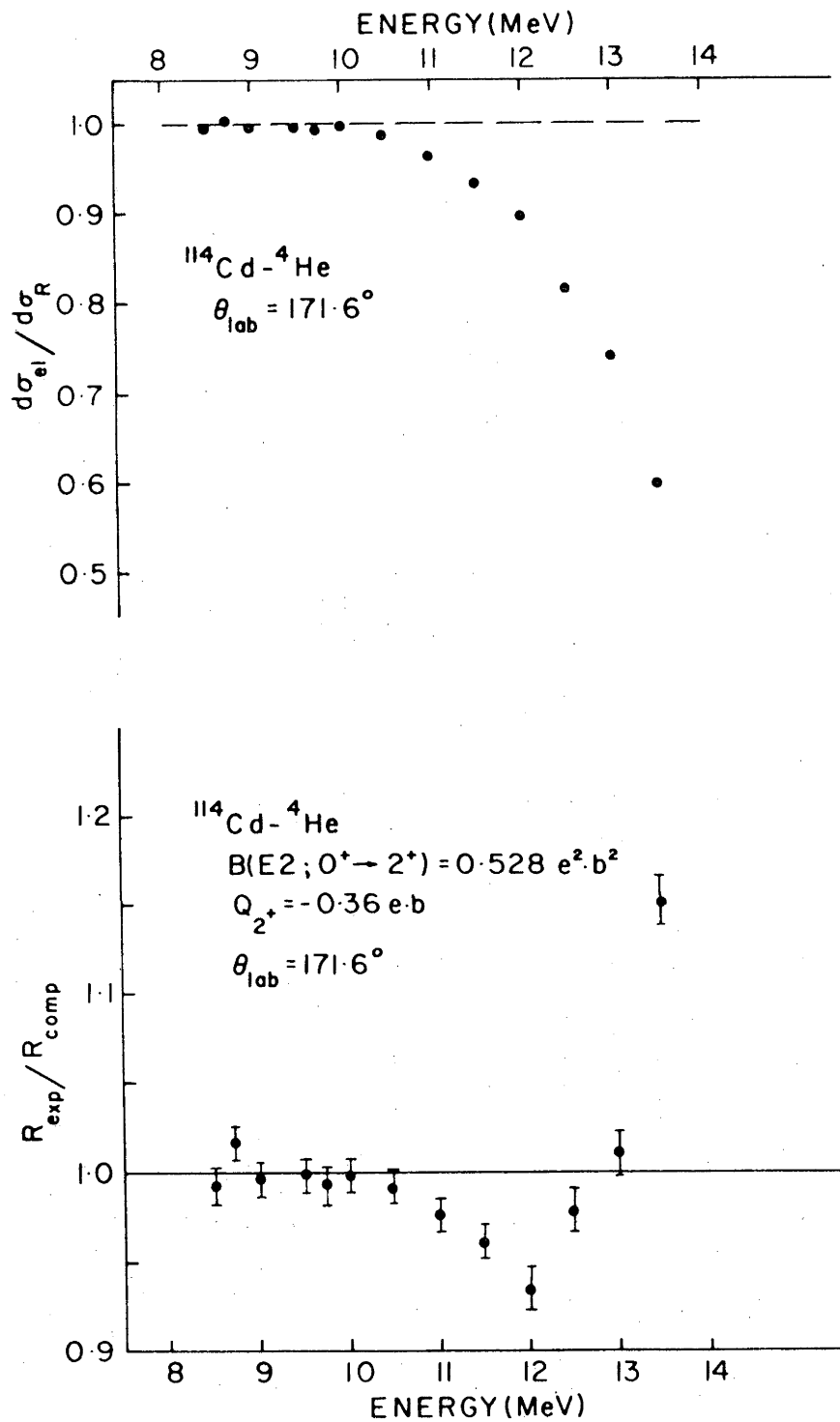| Experimenters	Nucleus	B(E2; $0^+ \rightarrow 2^+$) ($e^2.b^2$)	Q_{2^+} (e.b)	Barrier Energy for ^{4}He projectiles
B. Wakefield et al. (Wa 70)	^{114}Cd	0.534±0.011 0.547±0.013	0 (assumed) -0.623	≥10MeV
R. J. Pryor et al. (Pr 70)	^{114}Cd	0.558±0.14	-0.43 (assumed)	<10MeV
Z. Berant et al. (Be 72)	^{114}Cd	0.513±0.005	-0.28±0.09	>10MeV
D Werdecker et al. (We 73)	^{112}Cd ^{116}Cd	0.486±0.008 0.533±0.008	- -	>10MeV
Present work	^{114}Cd	0.528±0.004	-0.36±0.08	>10MeV

Figure 4.12. The ratio of the elastic to Rutherford cross section and the ratio of R_{exp} to R_{comp} for ^{4}He ions backscattered from ^{114}Cd as a function of ^{4}He bombarding energy.

rapidly due to the effect of nuclear forces. The behaviour of the 2^+ cross section is more relevant in determining the barrier energy as R_{exp}/R_{comp} is independent of any external normalizations. Furthermore, R_{exp}/R_{comp} is used directly to determine Q_{2^+}. Here R_{comp} refers to the calculated excitation probability assuming a pure Coulomb interaction. The present results for ^{114}Cd (fig. 4.12) are in agreement with those of Berant et al. (Be 72) and the excitation probability deviates by less than 1% from the pure Coulomb value for bombarding energies below 10.5MeV. Recently, similar results have also been obtained by Werdecker et al. (We 73). The behaviour of the 2^+ cross section above the barrier for ^{16}O projectiles could not be studied with the EN tandem (see section 3.1); however, in agreement with Berant et al. (Be 72), no evidence was found of deviation from pure Coulomb excitation below 44MeV bombarding energy.

The general features of the inelastic excitation probability, or of the double ratio R_{exp}/R_{comp}, above the Coulomb barrier, can be understood qualitatively by approximating the nuclear potential with an optical model potential. The total inelastic scattering amplitude expressed in terms of first order perturbation theory is (Vi 72)

$$a_T = i(a_C + a_R) + a_I \quad , \tag{4.13}$$

where a_C is the Coulomb excitation amplitude and a_R and a_I represent the real and imaginary amplitudes of the optical model potential respectively. The total cross section (assuming all a's to be real) is

$$\sigma_{2^+} \propto |a_T|^2 = (a_C + a_R)^2 + a_I^2 \quad . \tag{4.14}$$

The computed excitation probability $R_{comp} = (\sigma_{2^+}/\sigma_{0^+})_{comp}$, where $\sigma_{2^+}^{comp}$ is simply a_C^2. Therefore the double ratio R_{exp}/R_{comp} can be expressed in terms of amplitudes a as

$$R_{exp}/R_{comp} \propto \left[(1 + \frac{a_R}{a_C})^2 + (\frac{a_I}{a_C})^2 \right] (\sigma_{0^+}^{exp}/\sigma_{0^+}^{comp})^{-1} \quad , \qquad (4.15)$$

where $\sigma_{0^+}^{comp}$ is the Rutherford cross section. It should be noted that a_R and a_C have opposite signs because the Coulomb force is repulsive whereas the nuclear force is attractive. The variation of $\sigma_{0^+}^{exp}/\sigma_{0^+}^{comp}$ with bombarding energy is shown in figure 4.12. At bombarding energies below the barrier a_C dominates and $R_{exp}/R_{comp} = 1$. Above the barrier a_R changes faster than a_C and at some energy the first term will be zero. This accounts for the minimum observed in R_{exp}/R_{comp} at about 11.5MeV (fig. 4.12). At still higher energies nuclear absorption dominates and the inelastic cross section drops rapidly; however, $\sigma_0^{comp}/\sigma_0^{exp}$ is rising even faster and the overall effect is a rise in R_{exp}/R_{comp}. Detailed numerical calculations (see, for example, Broglia et al., Br 72) are in agreement with the gross features outlined above.

4.6 Procedures for Extracting the B(E2) and Q_{2^+} Values from the Data

Excitation probabilities derived from the data are listed in table 4.3. The quoted errors are a combination of the statistical uncertainty, the uncertainty arising in subtracting isotopic impurities, and uncertainties due to the possible presence of impurities below the background level in the ^{4}He spectra. The latter were estimated to be within twice the statistical error of the counts in the background region.

The data were analyzed with the de Boer-Winther multiple Coulomb excitation (MCE) code (Wi 66). The energy levels and E2 matrix elements included in the calculations are given in figure 4.13. The matrix elements are based on B(E2) values, branching and mixing ratios reported by Milner et al. (Mi 69), McGowan et al. (McGo 65) and Grabowski et al. (Gr 73). Computed excitation probabilities $R_{comp}^{(Q)}$ for a given projectile were parametrized in terms of the B(E2) and Q_{2^+} as (see section 2.5)

Table 4.3. Excitation probabilities for ^{16}O and ^{4}He projectiles in the cadmium isotopes. The effective bombarding energies E_{16_O} and $E_{4_{He}}$ have been corrected for target thickness effects as described in the text.

Isotope	E_{16_O} (MeV)	$10^2 \; R_{exp}(^{16}O)$	$E_{4_{He}}$ (MeV)	$10^3 \; R_{exp}(^4He)$
^{106}Cd	40.032	5.138±0.041	9.016	3.193±0.027
	40.022	5.146±0.043	9.522	4.159±0.037
	40.030	5.230±0.043	9.293	3.637±0.036
	41.030	5.691±0.047	9.993	5.354±0.046
	42.029	6.448±0.052		
	43.029	7.227±0.055		
	44.029	8.083±0.063		
^{108}Cd	40.033	5.523±0.046	8.994	3.287±0.028
	40.034	5.387±0.041	9.244	3.804±0.035
	41.031	6.068±0.049	9.494	4.347±0.039
	42.032	6.666±0.054	9.744	4.997±0.043
	43.031	7.409±0.062	9.869	5.267±0.049
	44.031	8.226±0.069	9.994	5.565±0.046
^{110}Cd	40.030	5.542±0.043	8.499	2.394±0.020
	41.026	6.326±0.051	8.794	2.894±0.024
	42.025	6.920±0.056	8.794	2.904±0.059
	43.031	7.743±0.063	9.084	3.479±0.029
	44.030	8.538±0.068	9.488	4.315±0.037
^{112}Cd	40.034	6.736±0.057	8.012	2.143±0.019
	41.035	7.593±0.064	8.512	3.026±0.026
	42.034	8.311±0.070	9.018	4.130±0.036
	43.037	9.202±0.074	9.524	5.486±0.046
	43.034	9.335±0.079	9.748	6.204±0.083
	44.034	10.273±0.087	9.995	7.014±0.058
	44.036	10.252±0.105		
^{114}Cd	40.024	8.335±0.060	8.511	3.912±0.033
	41.028	9.264±0.067	8.747	4.613±0.039
	42.027	10.260±0.075	9.017	5.266±0.046
	43.025	11.202±0.100	9.524	6.872±0.054
			9.747	7.624±0.061
			9.995	8.639±0.070
			9.995	8.553±0.075
^{116}Cd	40.025	9.264±0.081	8.511	4.477±0.036
	41.025	10.272±0.094	9.017	5.978±0.049
	41.022	10.282±0.093	9.523	7.762±0.064
	42.024	11.043±0.101	9.747	8.413±0.071
	43.025	12.213±0.112	9.994	9.279±0.076
	44.025	13.447±0.123		

$$\begin{matrix} 0 & M_{12} & 0 & -0.19 \\ M_{12} & M_{22} & -1.05 & \pm 0.32 \\ 0 & -1.05 & 0 & 0 \\ -0.19 & \pm 0.32 & 0 & 0 \end{matrix}$$

```
4 ——————— 1.718 ——————— 2 +'

3 ——————— 1.490 ——————— 4+




2 ——————— 0.633 ——————— 2+




1 ———————    0    ——————— 0+
              106Cd
```
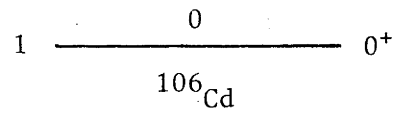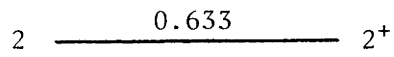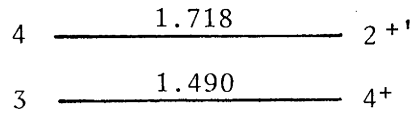
$$\begin{matrix} 0 & M_{12} & 0 & -0.17 \\ M_{12} & M_{22} & -1.06 & \pm 0.53 \\ 0 & -1.06 & 0 & 0 \\ -0.17 & \pm 0.53 & 0 & 0 \end{matrix}$$

```
4 ———————— 1.603 ———————— 2 +'
3 ————————————————————— 4+
           1.503



2 ———————— 0.633 ———————— 2+



1 ————————    0    ———————— 0+
              108Cd
```
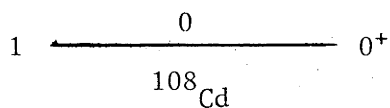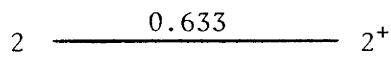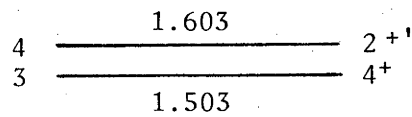
Figure 4.13. The energy levels and reduced electric quadrupole matrix elements used in the analysis.

$$
\begin{matrix}
0 & M_{12} & -0.15 & 0 \\
M_{12} & M_{22} & \pm 0.71 & -1.13 \\
-0.15 & \pm 0.71 & 0 & 0 \\
0 & -1.13 & 0 & 0
\end{matrix}
$$

4	1.542	4^+
3		$2^{+\prime}$
	1.476	

| 2 | 0.658 | 2^+ |

| 1 | 0 | 0^+ |

^{110}Cd

$$
\begin{matrix}
0 & M_{12} & -0.103 & 0 & -0.07 \\
M_{12} & M_{22} & \pm 0.54 & -1.31 & \pm 0.039 \\
-0.103 & \pm 0.54 & 0 & 0 & 0 \\
0 & -1.31 & 0 & 0 & 0 \\
-0.07 & \pm 0.039 & 0 & 0 & 0
\end{matrix}
$$

5	1.468	$2^{+\prime\prime}$
4		4^+
3	1.413	$2^{+\prime}$
	1.312	

| 2 | 0.617 | 2^+ |

| 1 | 0 | 0^+ |

^{112}Cd

$$\begin{array}{ccccccc}
0 & M_{12} & 0 & -0.098 & 0 & 0 & -0.09 \\
M_{12} & M_{22} & -0.31 & \pm0.637 & -1.38 & -0.31 & \pm0.016 \\
0 & -0.31 & 0 & 0 & 0 & 0 & 0 \\
-0.098 & \pm0.637 & 0 & 0 & 0 & 0 & 0 \\
0 & -1.38 & 0 & 0 & 0 & 0 & 0 \\
0 & -0.31 & 0 & 0 & 0 & 0 & 0 \\
-0.09 & \pm0.016 & 0 & 0 & 0 & 0 & 0
\end{array}$$

Level diagram for ^{114}Cd:

7 — 1.363 — $2^{+\prime\prime}$
6 — 1.305 — $0^{+\prime\prime}$
5 — — 4^{+}
4 — 1.282 — $2^{+\prime}$
3 — 1.208 —
— 1.133 — $0^{+\prime}$

2 — 0.558 — 2^{+}

1 — 0 — 0^{+}

^{114}Cd

$$\begin{array}{ccccc}
0 & M_{12} & -0.137 & 0 & 0 \\
M_{12} & M_{22} & \pm0.604 & -1.32 & -0.31 \\
-0.137 & \pm0.604 & 0 & 0 & 0 \\
0 & -1.32 & 0 & 0 & 0 \\
0 & -0.31 & 0 & 0 & 0
\end{array}$$

Level diagram for ^{116}Cd:

5 — — $0^{+\prime}$
4 — — 4^{+}
3 — — $2^{+\prime}$

2 — — 2^{+}

1 — — 0^{+}

^{116}Cd

$$R_{comp}^{(Q)} = f(E)B(E2)(1 + \rho(E)Q_{2^+}) \quad , \tag{4.15}$$

where $f(E)$ and $\rho(E)$ are polynomial functions of the bombarding energy E. A cubic polynomial was sufficiently accurate to reproduce f and a linear form was used for ρ. With this parametrization $R_{comp}^{(Q)}$ could be reproduced to better than 0.1% in the energy range used. The function $f(E)$ was obtained from the MCE code for a given B(E2; $0^+ \rightarrow 2^+$) value and with $Q_{2^+}=0$. Then $\rho(E)$ was determined using the same B(E2) value and for a given Q_{2^+}. If these B(E2) and Q_{2^+} values differed significantly from the ones obtained after a fit to the experimental data, $f(E)$ and $\rho(E)$ were recomputed using the B(E2) and Q_{2^+} values obtained from the fit. Equation (4.15) forms the basis for determining the B(E2) and Q_{2^+} values from a least squares fit to the experimental data. The basic equations used in a computer program (Ke 75), written for this purpose, are given below. It is convenient to rewrite equation (4.15) in the form

$$R_{comp} = a_1 X_1(E) + a_2 X_2(E) \quad , \tag{4.15a}$$

where $a_1 = B(E2)$, $a_2 = B(E2) \times Q_{2^+}$ and $X_1 = f$, $X_2 = f \times \rho$. The sum of the squares of the weighted differences between the experimental and computed excitation probabilities is

$$\chi^2 = \sum_i (1/\sigma_i^2)(R_{comp}^i - R_{exp}^i)^2 \quad , \tag{4.16}$$

where $\sigma_i^2 = R_{exp}^i$ (assuming statistical weighting) and i enumerates the experimental points both for ^{4}He and ^{16}O projectiles. The optimum values of parameters a_1 and a_2 are determined for

$$\delta\chi^2/\delta a_k = 0 \quad , \quad \text{with } k=1,2 \quad . \tag{4.17}$$

The result can be expressed as two simultaneous equations with $k=1$ and 2

$$\sum_i (\frac{1}{\sigma_i^2} R_{exp}^i X_k(E_i)) = \sum_{j=1}^{2} a_j \sum_i (\frac{1}{\sigma_i^2} X_j(E_i)X_k(E_i)) \quad , \tag{4.18}$$

or identically as

$$\beta_k = \sum_{j=1}^{2} (a_j \alpha_{jk}) \quad , \qquad (4.18a)$$

where β_k and a_j are elements of (2x1) row matrices and α_{jk} form a (2x2) square symmetric matrix. The coefficients a_j can be obtained by inverting the α matrix; i.e.,

$$a = \beta\alpha^{-1} \quad . \qquad (4.19)$$

The statistical uncertainties in coefficients a_j can be estimated from the relation (Be 69)

$$\sigma^2_{a_j} = (\alpha^{-1})_{jj} \quad . \qquad (4.20)$$

For the present problem, the uncertainty in the B(E2) value will be

$$\Delta\big(B(E2)\big) = \sqrt{\big((\alpha^{-1})_{11}\big)} \quad , \qquad (4.21)$$

and the uncertainty in Q_{2+}

$$\Delta Q_{2+} = Q_{2+} \left[\left(\frac{\Delta\big(B(E2)\big)}{B(E2)} \right)^2 + \left(\frac{(\alpha^{-1})_{22}}{B(E2) \times Q_{2+}} \right)^2 \right]^{\frac{1}{2}} \quad . \qquad (4.22)$$

The results obtained with this procedure are shown in figure 4.14 where R_{exp}/R_{comp} has been plotted versus the bombarding energy for both ^{4}He and ^{16}O projectiles.

4.7 Interference from Higher States

There is a significant contribution to the excitation probability of the first 2^+ state from higher $2^{+'}$ states. Furthermore, the computed excitation probability is sensitive to the sign of the product $<0^+ \| M(E2) \| 2^{+'}><2^{+'} \| M(E2) \| 2^+><2^+ \| M(E2) \| 0^+>$, which is a second order interference term arising from the excitation of the 2^+ state through an intermediate $2^{+'}$ level (see chapter 2). In the cadmium isotopes the magnitudes of the first two matrix elements are known from previous work

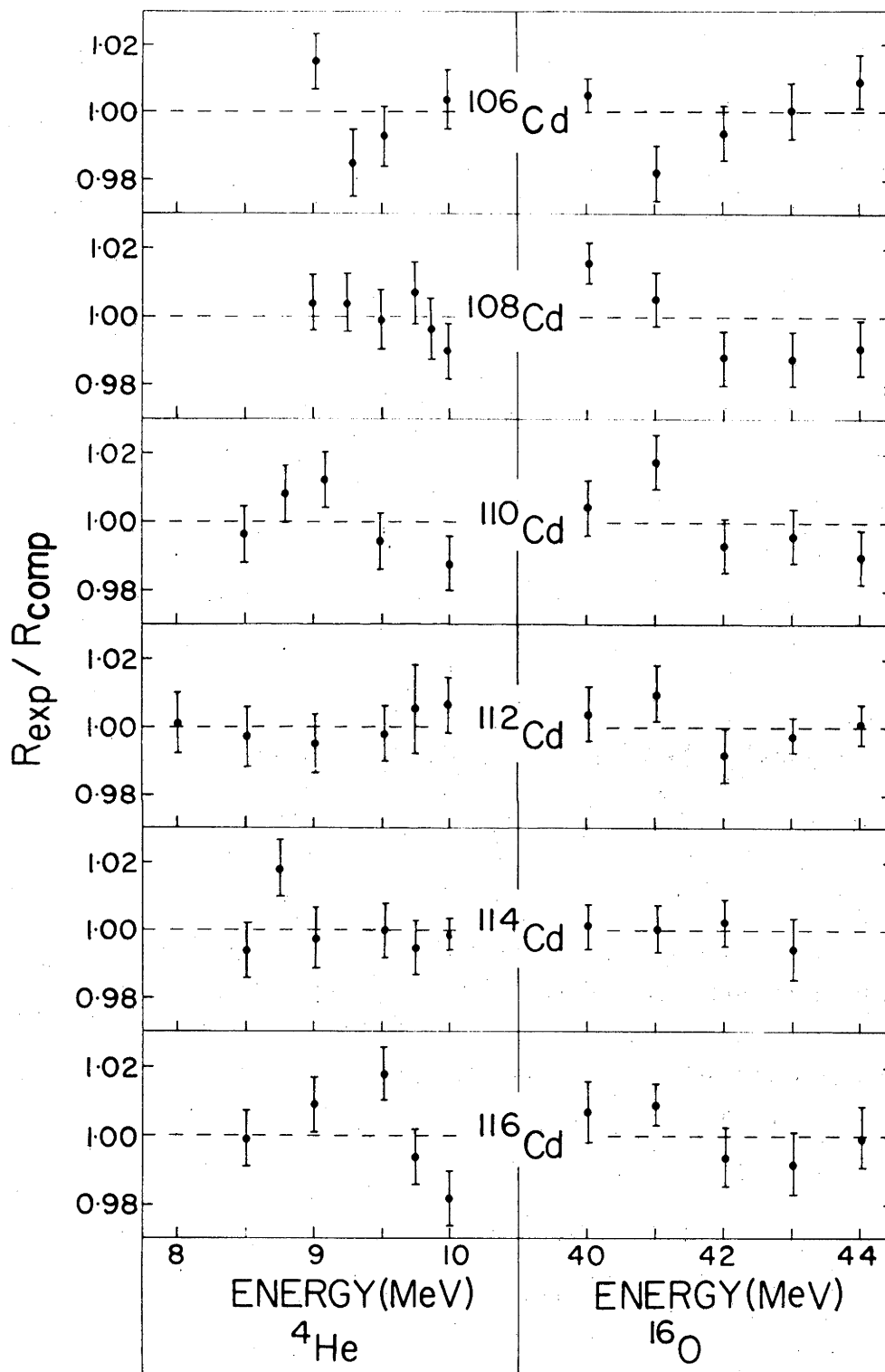Figure 4.14. The ratio R_{exp}/R_{comp} of the measured to computed excitation probabilities is plotted against bombarding energy of the ^{4}He and ^{16}O projectiles. The error bars shown represent a combination of the statistical uncertainty, the uncertainty arising in subtracting isotopic impurities, and uncertainties due to the possible presence of other impurities in the ^{4}He spectra.

(Mi 69); the relative sign of the three matrix elements, however, is not. Nevertheless, substantial evidence, model dependent as well as model independent, has now been accumulated indicating that the $2^{+'}$ interference in mass A~100 region is constructive. Some of this evidence is listed below:

a)   The triaxial rotor model of Davydov and Chaban (Is 69) and the pairing plus quadrupole model in the vibrational limit (Ku 69), predict constructive interference if $Q_{2^+} < 0$ and destructive interference for $Q_{2^+} > 0$.

b)   Tamura (Ta 68) has performed a coupled channels analysis of (p,p') data in A~100 region. In ^{112}Cd the fit to the angular distribution clearly favours constructive interference from the $2^{+'}$ state. Similar results have been obtained from electron scattering data on ^{114}Cd (Gi 76).

c)   There are two model independent determinations of the sign of the interference term in A~100 region. Larsen et al. (La 72) measured the quadrupole moment of ^{114}Cd using slow (~50MeV) sulphur projectiles. Under these conditions the effect of the interference term is minimized and the value of Q_{2^+} is less dependent on the sign chosen for the interference term. The agreement of their results with those of Berant et al. (Be 72) is much better assuming constructive $2^{+'}$ interference. In a recent reorientation precession experiment (see section 2.6b), Fahlander et al. (Fa 76) were able to determine the sign of the interference term in ^{102}Ru directly. Similar results have also been obtained in ^{108,110}Pd (Ha 76), confirming that, in this mass region, interference from $2^{+'}$ states is constructive.

4.8   Results

The values obtained for B(E2) and Q_{2^+} in the present work are

listed in table 4.4 for both positive (constructive) and negative

(destructive) interference from higher 2^+ states. There are two such

higher 2^+ levels known in ^{112}Cd and ^{114}Cd (see fig. 4.13) and the signs

of the interference terms were combined to yield the extreme values of

Q_{2^+}. However, it was found that the $2^{+''}$ states have a negligible effect

on the computed excitation probability $R_{comp}^{(Q)}$ and therefore do not affect

the B(E2) or Q_{2^+} values. The matrix elements for the $2^{+''} \rightarrow 2^+$ transitions

used in the analysis of the present data (see fig. 4.13) differ from those

adopted in earlier work (St 70, Be 72, Es 76). The difference arises

because of the previous ambiguities in the matrix elements for the $2^{+''} \rightarrow 2^+$

transitions. These were obtained from the work of Milner et al. (Mi 69),

who could not determine unique E2/M1 mixing ratios and therefore quoted

two equally likely B(E2; $2^{+''} \rightarrow 2^+$) values. In a γ-γ angular correlation

experiment Grabowski and Robinson (Gr 73) were able to assign unique

mixing ratios. The corresponding B(E2; $2^{+''} \rightarrow 2^+$) values in contrast to

those previously preferred in the analysis of reorientation effect

measurements, are small. A similar situation arises in ^{106}Cd, this time

with an ambiguity in the $2^{+'} \rightarrow 2^+$ matrix element. Again, the value deter-

mined by Grabowski and Robinson (Gr 73) is different from that adopted

previously (Ha 74). The results for Q_{2^+} listed in table 4.4 for

^{106,112,114}Cd were obtained with the revised values of the matrix elements

discussed above.

As stated above the B(E2; $2^{+''} \rightarrow 2^+$) values reported by Grabowski

et al. (Gr 73) in ^{112,114}Cd are small and the inclusion of $2^{+''}$ states in

the analysis of reorientation effect measurements alters $R_{comp}^{(Q)}$ by less

than 0.02%. Therefore, if $2^{+''}$ states exist in the other Cd isotopes,

with similar matrix elements, the present results for Q_{2^+} will not be

affected. The possible presence of $2^{+''}$ states or of any others previously

Table 4.4. The B(E2; $0^+ \rightarrow 2^+$), Q_{2^+} and normalized χ^2 values obtained in the present experiment both for constructive (+) and destructive (-) interference from the higher 2^+ states. Only the statistical errors were used in the calculation of χ^2. The number of data points used in the fit is denoted by n.

Isotope	Interference term	B(E2; $0^+ \rightarrow 2^+$) ($e^2.b^2$)	Q_{2^+} (e.b)	$\chi^2/(n-2)$	n
^{106}Cd	+	0.384±0.004	-0.28±0.08	1.7	11
	-	0.383±0.004	-0.12±0.08	2.0	11
^{108}Cd	+	0.407±0.004	-0.45±0.08	2.0	12
	-	0.405±0.004	-0.20±0.08	1.5	12
^{110}Cd	+	0.427±0.004	-0.36±0.08	1.5	11
	-	0.425±0.004	-0.04±0.08	1.1	11
^{112}Cd	+	0.484±0.004	-0.39±0.08	0.5	13
	-	0.482±0.004	-0.19±0.08	0.5	13
^{114}Cd	+	0.528±0.004	-0.36±0.08	0.7	11
	-	0.527±0.004	-0.16±0.08	0.7	11
^{116}Cd	+	0.532±0.004	-0.42±0.08	1.7	11
	-	0.531±0.004	-0.17±0.08	1.5	11

undetected in ^{106,108,110,116}Cd was investigated with 17.5MeV ^{4}He pro-

jectiles (Sp 76). The experimental geometry was similar to that used

for $Q_{2^{+}}$ measurements below the Coulomb barrier (see chapter 3). The

(α,α') reaction is known to preferentially populate collective states

(Ho 71); it is states such as these which are most likely to influence

the population of the 2^{+} state through higher order multiple Coulomb

excitation processes. The results of the (α,α') experiment are displayed

in a composite diagram in figure 4.15 (see also fig. 5.6). An inspection

of this diagram shows that there are no significantly populated additional

levels in the region of the 2 phonon triplet other than those already

known. The relative paucity of levels in ^{106}Cd and ^{108}Cd is thus confirmed.

A striking feature of the spectra in figure 5.6 is the strong population

of a level roughly at 2MeV excitation in all of the cadmium isotopes.

Inelastic scattering experiments with protons, α-particles and electrons

favour a 3^{-} spin assignment to these levels (Gi 76); the results, however,

are not conclusive (see, for example, Gill et al., Gi 74). If these are

3^{-} states they contribute to the excitation of the 2^{+} state through an

interference term of the form $<0^{+}||E3||3^{-}><3^{-}||E1||2^{+}><0^{+}||E2||2^{+}>$. The

effect of this term in ^{114}Cd was investigated, assuming $B(E3;0^{+}\rightarrow3^{-})$ =

0.09 $e^{2}.b^{3}$ (McG 65, Gi 74). The $B(E1; 3^{-}\rightarrow2^{+})$ value was assumed to be

0.1 W.u., which is an upper limit (for example, typical values of similar

E1 matrix elements in Pd isotopes are $\sim10^{-4}$ W.u., Ro 69). The contribution

of the 3^{-} interference term to $R_{comp}^{(Q)}$ is then less than 0.01% and therefore

it does not significantly affect the determination of $Q_{2^{+}}$ or $B(E2)$ values.

If the $3^{-}\rightarrow2^{+}$ decay has significant E3 component (~0.09 $e^{2}.b^{3}$) the contri-

bution to $R_{comp}^{(Q)}$ is less than 0.2% which is again negligible.

In a recent electron scattering experiment Gillespie et al. (Gi 76)

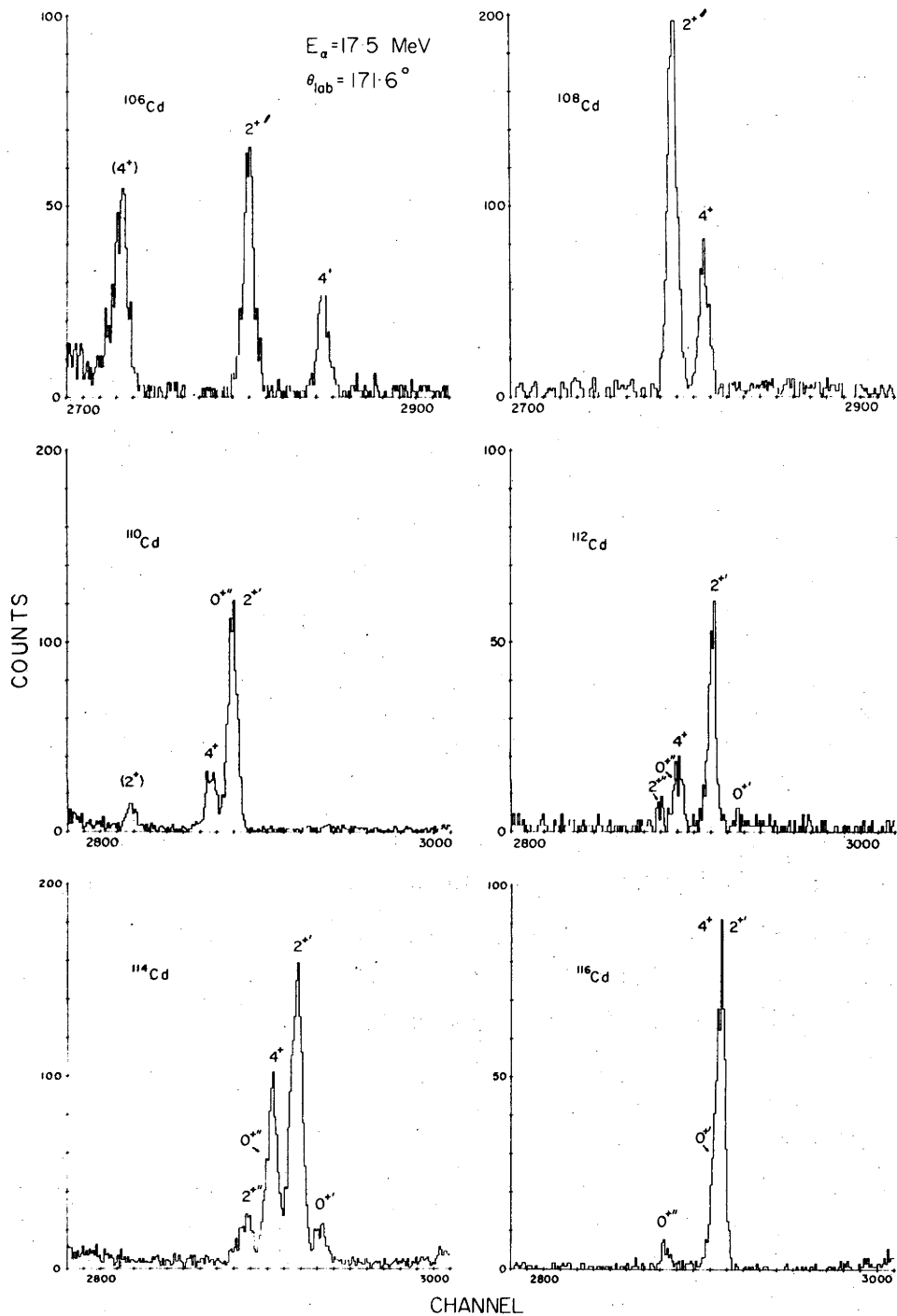determined the $B(E2; 0^{+}\rightarrow2^{+'})$ value in ^{114}Cd. However, the statistical

Figure 4.15.   Spectra of 17.5MeV ^{4}He ions scattered from the even-mass
cadmium isotopes at θ_{lab}=171.6°.   Only the two phonon region
is shown for each isotope.   Contributions from impurity
isotopes have been subtracted from the data.

accuracy of their data was poor and the contribution of the unresolved 4^+ and $0^{+'}$ levels at 1.282 and 1.305MeV, respectively, had to be subtracted from the data. Their result is about 3.4 times smaller than the B(E2; $0^+ \rightarrow 2^{+'}$) value determined by Milner et al. (Mi 69). A corresponding change in this matrix element, in the analysis of the present ^{114}Cd data, reduces the extracted quadrupole moment $|Q_{2^+}|$ by about 0.04 e.b. This would be a large change if it were confirmed, with possible implications in the other cadmium isotopes. It is possible to check this value, roughly, using the present ^{4}He data. At 10.5MeV bombarding energy the $2^{+'}$ state is clearly visible above the background level (fig. 4.16) and is well separated from likely elastic impurity peaks such as Fe, Cu or Zn. Any elastic impurity peaks under the $2^{+'}$ peak would have been visible in the data taken at bombarding energies up to 17.5MeV. The ratio $\sigma_{2^{+'}}/\sigma_{2^+}$ obtained from the 10.5MeV data is 0.63±0.2%. The same ratio calculated with the MCE code is 0.47% or 0.16% using the $0^+ \rightarrow 2^{+'}$ matrix elements reported by Milner et al. or by Gillespie et al. respectively. Clearly the present data are not in agreement with the small value of B(E2; $0^+ \rightarrow 2^{+'}$) claimed by Gillespie et al.

The B(E2) and Q_{2^+} values given in table 4.4 were corrected for small effects due to virtual excitation of the giant dipole resonance, quantal effects, atomic screening and vacuum polarization (Hä 74). Each of these affects R_{exp} by $\leq 1\%$. In figure 4.17 the magnitude of these processes, the contribution from higher 2^+ states and the effect of the non-zero quadrupole moment are shown as a relative change in the excitation probability ($\Delta R/R\%$) for both ^{4}He and ^{16}O projectiles and a ^{114}Cd target. The effect of higher 2^+ states and Q_{2^+} can readily be obtained from the MCE code, the others were determined as outlined below.
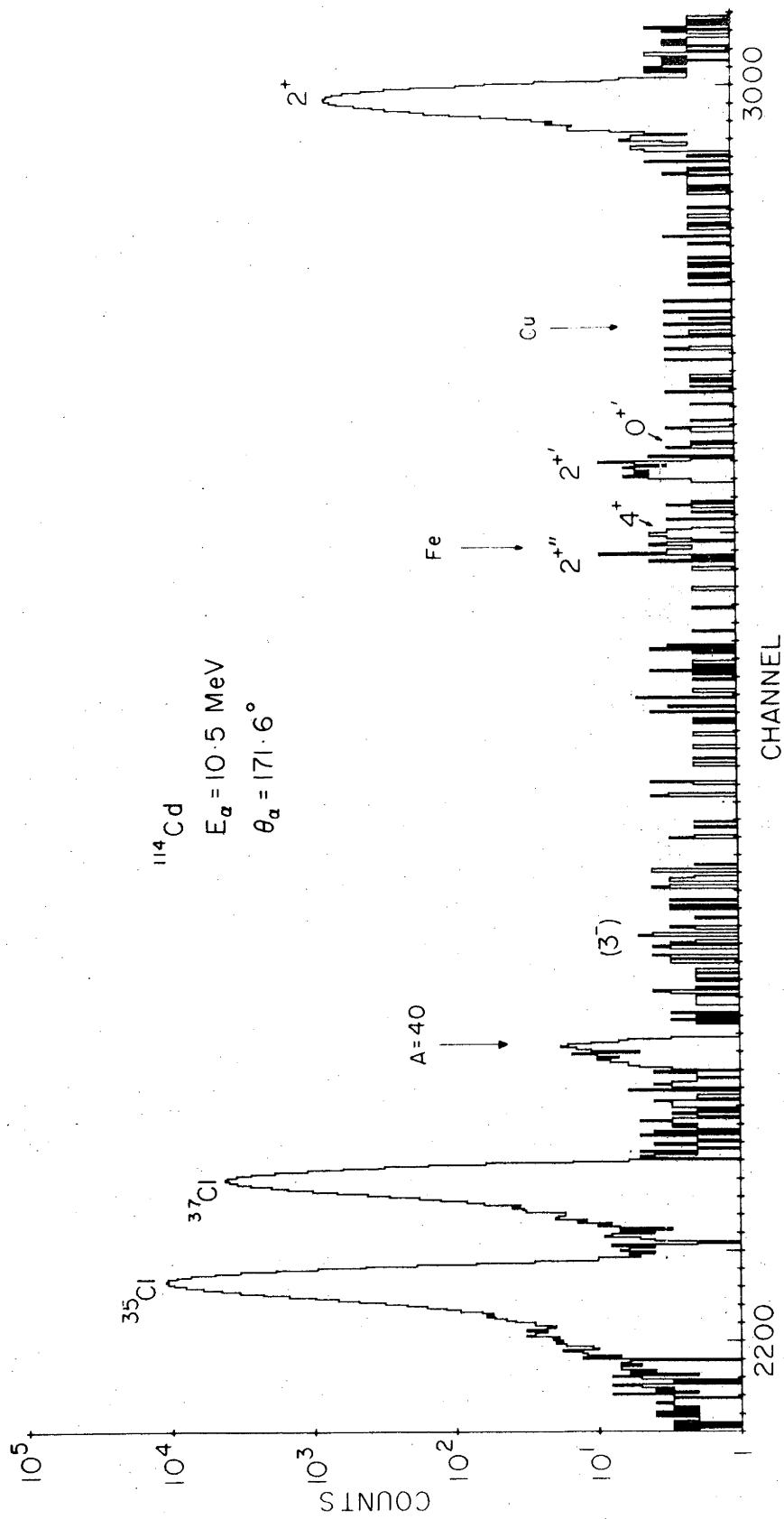
Figure 4.16. Spectrum of 10.5MeV ^{4}He ions backscattered from ^{114}Cd. The $2^{+'}$ state is clearly visible and is well separated from common target impurities such as Fe and Cu.

4.9 Dipole Polarization

The relative displacement of the neutron and proton fluids in an adiabatic collision where $\tau_{coll} \gtrsim \tau_{nuc}$ leads to the dipole polarization of the nucleus (see chapter 2). In Coulomb excitation the cross section for low-lying states can therefore be influenced by virtual transitions via the giant dipole resonance (GDR). The GDR itself is at high excitation energy (~16MeV in Cd) and will not be excited. The additional potential energy due to polarization can be estimated (de Bo 68, Al 75) and is proportional to the polarizability P, the square of the electric field of the projectile **E**, and to the square of the nuclear radius R in the field direction. The latter parameter is obtained by assuming that the nuclear surface can be described in terms of quadrupole deformations. The polarizability is estimated from the minus two moment σ_{-2} of the photoabsorption cross section (Le 57)

$$\sigma_{-2} \equiv \int \sigma(E)(dE/E^2) = \frac{4\pi^2}{\hbar c} \, P \sim 3.5 k A^{5/3} \mu b/MeV \quad ; \qquad (4.23)$$

for nuclei with Z~50, k~1 (see, for example, Hä 73 and the references therein). The dipole polarization potential can be included in the inter-action Hamiltonian (equation 2.9); for E2 excitation the result is

$$H_e(t) = \frac{4\pi e}{5} \, Z \sum_{1\mu} (-1)^\kappa \frac{1}{r^3} \, M(E2,-\mu) Y_{2\mu}(\theta,\xi) \left(1-0.0056k \, \frac{A_2}{Z_2^2} \, E_{cm} \, \frac{a}{r_p(t)}\right) , (4.24)$$

where 2a is the closest distance of approach. The additional term in the brackets was incorporated into the MCE code (Ke 75). The change in $R_{comp}^{(Q)}$ amounts to ~0.2% and ~0.8% for ^{4}He and ^{16}O projectiles respectively (fig. 4.17) and corresponds to a reduction in $|Q_{2^+}|$ of about 0.05 e.b.

4.10 Quantal Corrections

As outlined in chapter 2, the semiclassical derivation of Coulomb

excitation cross sections is expected to be quite accurate provided $\eta \gg 1$ and parameters ξ, χ, etc., are symmetrized with respect to incoming and outgoing velocities. For the ^{4}He and ^{16}O energies used in the present work $\eta \sim 10$ and ~ 40, respectively, and significant corrections to $R_{comp}^{(Q)}$ may be expected.

Full quantal calculations have been performed by Smilansky (Sm 68), Alder and Pauli (Al 69), and Alder, Roesel and Morf (Al 72). In the latter reference quantal corrections to both first order and second order excitation probabilities are tabulated in a convenient form. Corrections to first order are small, since they are largely accounted for by symmetrization, and vary as $1/\eta^2$. The leading second order terms are due to the quadrupole moment effect and the influence of $2^{+'}$ states. The second order corrections are proportional to $1/\eta$ and can be large. Semiclassically the excitation probability of the 2^+ state can be written as (see chapter 2)

$$R_{0^+ \to 2^+} = (\chi_{0 \to 2}^{(2)})^2 \, P_2(\theta, \xi) \left(1 + x(0,2,2) \, C(\xi, 0, \theta)\right.$$

$$\left. + x(0,2',2) \, C(\xi_1, \xi_2, \theta) + \text{terms } O(x^2)\right) \quad , \quad (4.25)$$

where

$$x(I_i, I_Z, I_f) = \chi_{i \to Z}^{(2)} \, \chi_{Z \to f}^{(2)} / \chi_{i \to f}^{(2)} \quad . \quad (4.26)$$

The second term in equation (4.25) is due to non-zero Q_{2^+} and the third term accounts for $2^{+'}$ interference; the influence of higher terms is relatively small and they were neglected. The adiabaticity parameters ξ in equation (4.25) are defined in the diagram below

$$\xi = \xi_1 + \xi_2 \quad , \quad \xi_2 < 0 \quad .$$
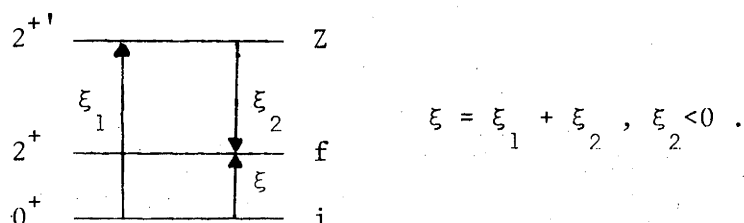
Typically $\xi_1 = 0.78$, $\xi_2 = -0.44$ for ^{4}He and $\xi_1 = 0.63$, $\xi_2 = -0.34$ for ^{16}O projectiles in the present experiments. Corrections to parameters C for $\eta \neq \infty$ are tabulated in Alder (Al 72). It turns out that there is less than 2% difference in the correction factor $C(\xi_1,\xi_2,\eta,\theta)/C(\xi_1,\xi_2,\infty,\theta)$ for the Q_{2^+} term and the $2^{+'}$ interference term. Therefore both terms can be corrected for quantal effects simultaneously. Equation (4.25) can be written as

$$R_{0^+ \to 2^+} = f(E)B(E2)(1 - \rho Q_{2^+}) \quad , \tag{4.27}$$

where $f(E)$ and $\rho(E)$ contain all orders of perturbation - the dominant ones being the Q_{2^+} and $2^{+'}$ terms (fig. 4.17). Therefore, approximately,

$$f \propto P_2 \quad ,$$

and

$$\rho \propto x(0,2,2)C(\xi,0,\theta) + x(0,2',2)C(\xi_1,\xi_2,\theta) \quad ;$$

the appropriate corrections were applied to ρ and f. For the first order correction the η dependence can be parametrized as

$$f(\eta) = f(\infty) - e(\theta,\xi)/\eta^2 \quad , \tag{4.28}$$

where e is the correction term and is independent of η. For given η and η_0, equation (4.28) gives

$$\frac{f(\eta)}{f(\infty)} = 1 + \left(\frac{\eta_0}{\eta}\right)^2 \left(\frac{f(\eta_0)}{f(\infty)} - 1\right) \quad , \tag{4.29}$$

where $f(\eta_0)/f(\infty)$ is tabulated in Alder (Al 72) for $\eta_0 = 4$ and 8, and η is the Sommerfeld parameter corresponding to the experimental conditions used. The first order correction amounts to about 0.3% and 0.02% in f for ^{4}He and ^{16}O projectiles respectively. Similarly the η dependence of ρ is given by

$$\frac{\rho(\eta)}{\rho(\infty)} = 1 + \frac{\eta_0}{\eta} \left(\frac{\rho(\eta_0)}{\rho(\infty)} - 1 \right) \quad . \tag{4.30}$$

Using equations (4.29) and (4.30) and the tables in Alder (Al 72), parameters f and ρ were corrected for quantal effects. Corrections to the excitation probability for ^{4}He and ^{16}O projectiles are shown in figure 4.17 and are nearly of the same magnitude. This is because the energy/nucleon in the centre of mass system is nearly the same for both ^{4}He and ^{16}O projectiles. Corrections to Q_{2^+} for quantal effects are therefore negligible and a small correction to the B(E2) value results.

4.11 Atomic Screening

The excitation probabilities calculated with the MCE program assume that the Coulomb field of the target is due to a naked charge of magnitude Z_2e. However, the target nucleus is surrounded by a cloud of electrons which dilute the electric field. The presence of electrons modifies the classical Rutherford trajectory so that the closest distance of approach is smaller for a screened atom, i.e., the effective bombarding energy is higher. Saladin (Sa 69) has suggested a way of accounting for this using the formula

$$\Delta E_{CM} = +Z_1 (32.65 \; Z_2^{7/5} - 40 \; Z_2^{2/5}) \; eV \quad . \tag{4.31}$$

which is based on corrections to α decay energy differences between a bare nucleus and an atom (see I. Pearlman et al., Pe 57). The collision with the target nucleus takes place inside the atomic electron cloud, therefore ΔE is approximately independent of the bombarding energy. This correction amounts to about 15keV for ^{4}He and 66keV for ^{16}O projectiles in the laboratory system. The correction to the excitation probability is nearly the same for ^{4}He and ^{16}O projectiles and amounts to 0.8 and 0.7% respectively. Thus Q_{2^+} is unaffected by this correction.
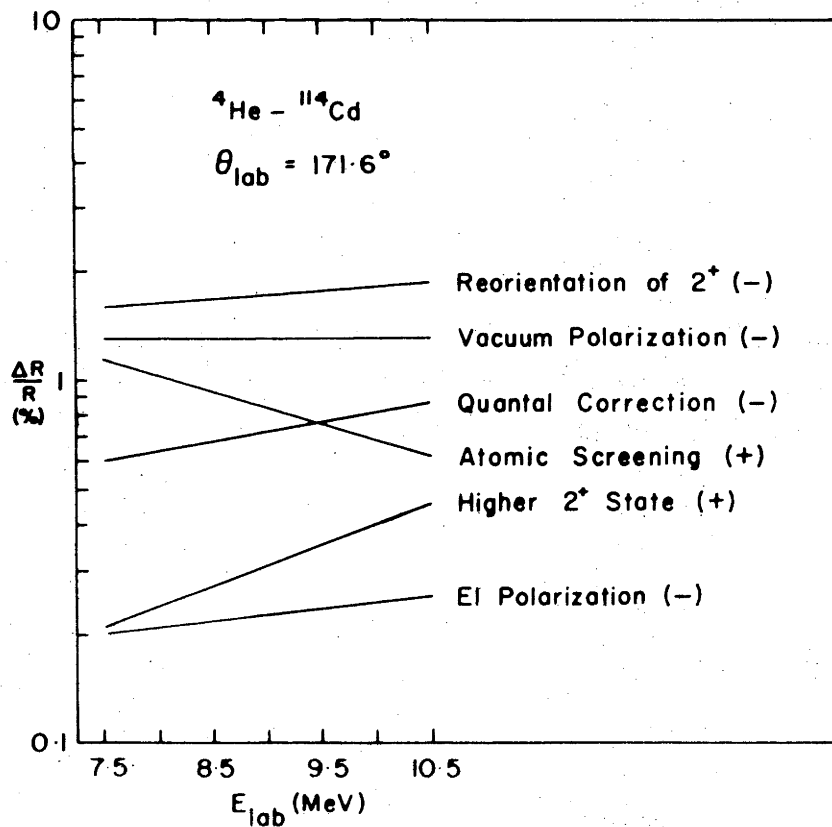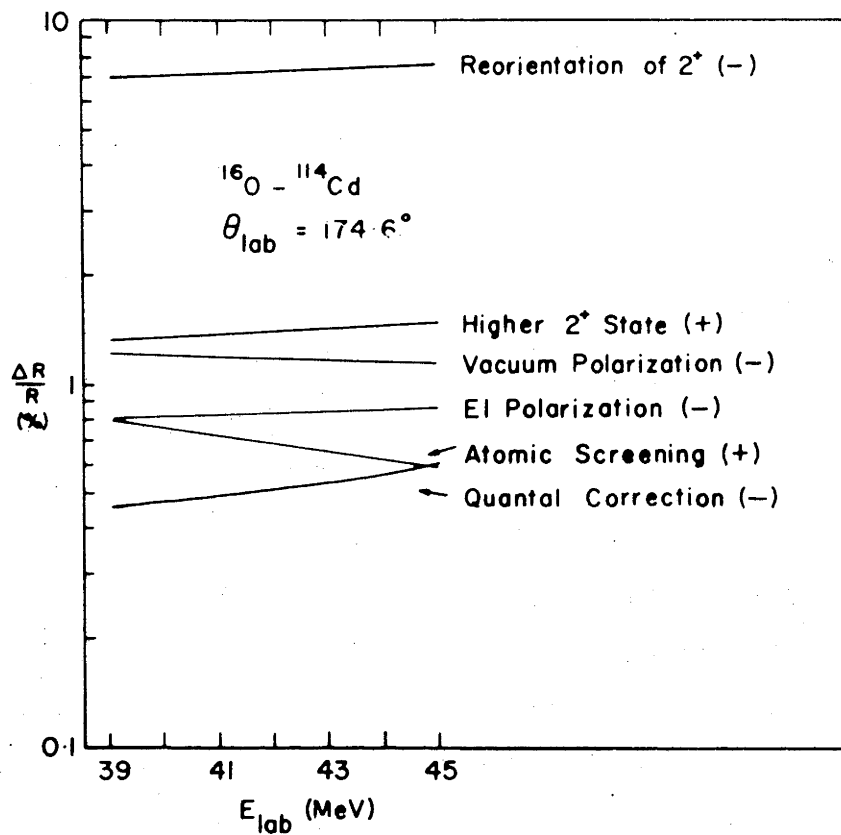
Figure 4.17. Energy dependence of ΔR/R for ^{4}He and ^{16}O ions backscattered from ^{114}Cd. The energy ranges shown correspond to those used in the present work.

4.12 Vacuum Polarization

During a collision between two ions the potential energy of the system is altered due to an extra induced charge corresponding to a polarization of the vacuum. The Coulomb repulsion between the two charges is increased, corresponding to a decrease in the effective bombarding energy (Ue 35). The additional induced potential is

$$\Delta V_{vac}(r) = \frac{e^2}{2\pi\hbar c} \frac{Z_1 Z_2 e^2}{r} v(r/\lambda_c) \quad , \qquad (4.32)$$

where $\lambda_c = \hbar/mc = 386.17$ fm. is the Compton wavelength of the electron, and

$$v(r/\lambda_c) = \int_0^1 (2x^2(1-\frac{1}{3}x^2)/(1-v^2)) \exp\left(-2r/(1-x^2)^{\frac{1}{2}}\lambda_c\right) \quad . \quad (4.33)$$

This integral can be evaluated numerically (Ca 69), and for the present experimental conditions results in a decrease of about 25keV and 120keV in ^{4}He and ^{16}O bombarding energies. The corresponding change in the excitation probability (fig. 4.17) is nearly the same for both ^{4}He and ^{16}O projectiles and does not affect the Q_{2^+} value.

Small additional corrections may result from relativistic effects (Al 75) or bremsstrahlung (Al 56). The effective bombarding energy is changed by less than 1 keV for each of these effects and they have been ignored.

4.13 Summary of Main Sources of Error

The net effect of all the corrections discussed in sections 4.9 to 4.12 amounts to about 1.7% and 2.4% for ^{4}He and ^{16}O projectiles respectively. In the present experiments only the giant dipole resonance correction significantly affects $|Q_{2^+}|$, reducing it by about 0.05 e.b.

The quoted errors in the B(E2) and Q_{2+} values in table 4.4 arise from the quadratic combination of the errors due to beam-energy and target-thickness uncertainties, and statistical and systematic errors in intensity extraction as outlined in this chapter. The main components are listed below

Errors in the B(E2) value:

a)	Accelerator energy calibration	0.0012 $e^2.b^2$
b)	Data analysis and contaminants	0.0025 $e^2.b^2$
c)	Statistical errors	0.003 $e^2.b^2$
	The total is	0.004 $e^2.b^2$

Errors in the Q_{2+} value:

|		
a)	Data analysis and contaminants	0.03 e.b
b)	Subtraction of the ^{16}O elastic tail contribution to the 2^+ peak	0.06 e.b
c)	Statistical errors	0.04 e.b
	The total is	0.08 e.b

CHAPTER 5.

DISCUSSION OF RESULTS AND CONCLUSION

This chapter contains a discussion of the results presented
in chapter 4. The (B(E2; $0^+ \rightarrow 2^+$) and Q_{2^+} values obtained for the even-A
stable cadmium isotopes are compared with the results of previous expe-
riments and with theoretical calculations. Initially, the experimental
situation in each of the isotopes is discussed. For reference the
present and previous results are summarized in figure 5.1. In this
diagram and in what follows the $2^{+'}$ interference term is always assumed
to be constructive (see section 4.7 for the evidence in support of this)
and only the most negative values of Q_{2^+} are considered.

5.1 Comparison of Present and Previous Experimental Results

For meaningful comparison of various experimental results, it
is essential to note whether corrections due to vacuum polarization,
quantal effects, atomic screening, and E1 polarization have been made.
In the present work, the fractional change in the excitation probability
due to vacuum polarization, quantal and screening corrections are roughly
the same for ^{4}He and ^{16}O projectiles; therefore they do not affect the
Q_{2^+} value. The E1 polarization lowers $|Q_{2^+}|$ by about 0.05 e.b (it
should be noted that the E1 correction has not been applied to any of
the previous measurements of Q_{2^+} in the cadmium isotopes). The quantal
and atomic screening corrections are of about equal magnitude but opposite
in sign (see fig. 4.17), therefore applying both corrections results in
negligible change in the B(E2) value. The only significant correction
to the B(E2) value arises from the vacuum polarization correction, which
increases it by about 1%.

Figure 5.1.

Variation of Q_{2^+} across the cadmium isotopes. The experimental points are taken from the survey of Christy and Häusser (Ch 72) (open circles), the recent work of Hall et al. (Ha 74, Ha 75) (triangles), and the present work (closed circles). The theoretical calculations are by Sorensen (So 73) (dashed line) and Sips (Si 71) (full line). For the present data, the statistical errors are approximately half the total errors shown.
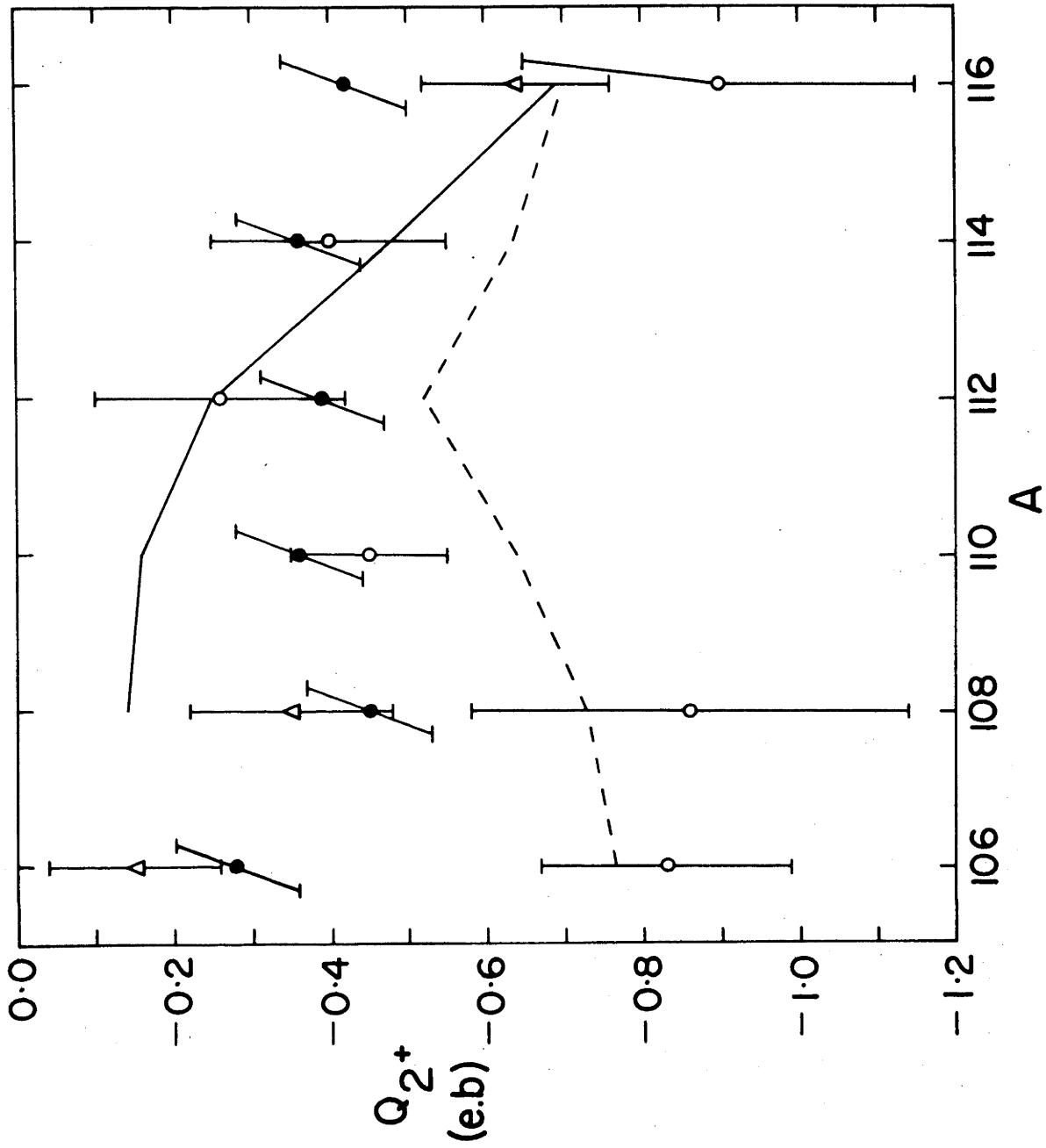
In the following discussion, data which were taken at too high a bombarding energy or did not include corrections for vacuum deorientation (section 2.6) will be excluded (Ch 72). For the sake of convenience the results of Steadman et al. (St 70), and those of Kleinfeld et al. (Kl 70), for ^{106}Cd and ^{114}Cd, will be referred to as "the Rutgers data". The results of Hall et al. (Ha 74, Ha 75) for ^{106}Cd, ^{108}Cd, and ^{116}Cd will be referred to as "the Liverpool data". A list of present and previous measurements of B(E2; $0^+ \rightarrow 2^+$) and Q_{2^+} is given in table 5.1.

The Nuclei ^{106}Cd and ^{108}Cd

There are three previous measurements of Q_{2^+} in ^{106}Cd and two in ^{108}Cd. The initial measurement was made by the Rutgers group using a natural cadmium target (see section 2.6). The de-excitation γ-rays from ^{106}Cd and ^{108}Cd were not resolved and an average value Q_{2^+} = -0.84±0.28 e.b was obtained. This implies that both the ^{106}Cd and ^{108}Cd values for $|Q_{2^+}|$ are large. In a subsequent experiment at Rutgers, Kleinfeld et al. (Kl 70) remeasured Q_{2^+} in ^{106}Cd using an enriched target and a particle-γ coincidence method (section 2.6); their result is Q_{2^+} = -0.83±0.16 e.b. From these two Rutgers measurements the Q_{2^+} for ^{108}Cd can be extracted as = -0.9±0.6 e.b, which is not very precise.

In contrast to the above measurements, which resulted in large $|Q_{2^+}|$ values for ^{106,108}Cd, the Liverpool group have recently remeasured Q_{2^+} for ^{106,108}Cd using a particle-γ coincidence method which does not require the absolute efficiency of the γ-ray detector (see section 2.6) and find the comparatively small values tabulated in table 5.1. The present results are in fair agreement with the Liverpool ones and do not support the large values reported by the Rutgers group. In comparing previous data with the present result for ^{106}Cd, however, it should be

noted that the $2^+ \rightarrow 2^{+'}$ matrix element used differs from that

previously preferred (see section 4.8). Omitting the E1 polarization

correction, and using the previous value of $M_{2^+ \rightarrow 2^{+'}}$ for ^{106}Cd, the

present results for ^{106,108}Cd would be -0.37 e.b and -0.50 e.b respec-

tively, which are still somewhat larger in magnitude than the Liverpool

results. It is interesting to note that the ratio $Q_{2^+}(^{106}\text{Cd})/Q_{2^+}(^{108}\text{Cd})$

is 1.6±0.5 for the present data and 2.3±1.6 for the Liverpool data.

The Nucleus ^{110}Cd

There are three previous measurements of Q_{2^+} in this nucleus.

In this case the Rutgers result, in contrast to those for ^{106} ^{108}Cd, is

small (table 5.1). The second measurement is by Harper et al. (Ha 71)

at Liverpool. They use an experimental method which differs from that

employed in the ^{106,108}Cd measurements, in that the absolute efficiency

of the γ-ray detector, and thus the B(E2; $0^+ \rightarrow 2^+$) as well as the Q_{2^+} value,

could be determined. The third measurement, by Berant et al. (Be 72),

employs an experimental method which is similar to that used in the

present work. However, they do not apply E1 or vacuum polarization

corrections. Applying these, their value for Q_{2^+} is -0.37 e.b, which is

in good agreement with the present results. The vacuum polarization

correction increases the B(E2) value by only about 1%. It can be seen

that the B(E2) value determined by Berant et al. (table 5.1) agrees well

with the present result. The values for B(E2) and $|Q_{2^+}|$ reported by

Harper et al. are somewhat larger than the present results; however,

the overall agreement between all the measurements is good (table 5.1).

The Nucleus ^{112}Cd

The two previous measurements of Q_{2^+} in this nucleus are by

the Rutgers group and by Häusser et al. (Hä 71). The Rutgers value is small in magnitude compared with the present one (table 5.1). Häusser et al. used a surface barrier detector at 70°, an annular counter, and an array of six NaI detectors in a particle-γ coincidence, two-angle measurement. The giant-dipole and quantal corrections were considered by Häusser et al. but not applied; the errors in Q_{2^+} were increased to account for the uncertainty in the results due to effects of such corrections. The Q_{2^+} value derived from this measurement is in good agreement with the present result. It should be noted, however, that the $(2^+ \rightarrow 2^{+''})$ matrix elements used in the analysis of the present data differ from those used earlier (see section 4.8). This results in a small decrease (0.02 e.b) in $|Q_{2^+}|$ but does not affect the B(E2) value.

The Nucleus ^{114}Cd

The measurements in this nucleus are too numerous to discuss individually; they are listed in table 5.1. The result of Saladin et al. (Sa 69), Q_{2^+} = -0.68±0.09 e.b, is large in magnitude compared with the rest of the data. However, as shown by Berant et al. (Be 72), Saladin's forward angle ^{16}O data (see section 2.7 for an account of the experimental method used) are in disagreement with the ^{4}He data of Berant et al., who conclude that the difficulty lies in Saladin's forward angle ^{16}O data. Interesting experimental methods employed to measure Q_{2^+} in ^{114}Cd include that of Andreyev et al. (An 70), who were able to simultaneously accelerate He^{1+} and C^{3+} beams in a cyclotron. This method avoids the difficulties encountered with the energy definition and stability of most cyclotron beams. Larsen et al. (La 72), using low energy ^{32}S beams (see section 4.7), were able to determine the sign of the $2^{+'}$ interference term. Hosayama et al. (Ho 73) and Gillespie et al. (Gi 76) have measured the

Table 5.1. Summary of the present and previous
measurements of B(E2; $0^+ \rightarrow 2^+$) and Q_{2^+}
in the cadmium isotopes.

The nucleus ^{106}Cd

Reference	Q_{2^+} e.b	B(E2; $0^+ \rightarrow 2^+$) $e^2.b^2$
Steadman et al. (St 70)	-0.84±0.28	0.417±0.029
Kleinfeld et al. (Kl 70)	-0.83±0.16	0.399±0.023
Hall et al. (Ha 74)	-0.15±0.11	0.43 (assumed)
Milner et al. (Mi 69)	-	0.426±0.017
Present work	-0.28±0.08	0.384±0.004

The Nucleus ^{108}Cd

Reference	Q_{2^+} e.b	$B(E2;\ 0^+ \rightarrow 2^+)$ $e^2.b^2$
Steadman et al. (St 70)	-0.9±0.6	0.417±0.029
Hall et al. (Ha 74)	-0.35±0.13	0.45 (assumed)
Milner et al. (Mi 69)	-	0.442±0.018
Present work	-0.45±0.08	0.407±0.004

The Nucleus ^{110}Cd

Reference	Q_{2^+} e.b	B(E2; $0^+ \rightarrow 2^+$) $e^2.b^2$
Steadman et al. (St 70)	-0.24±0.09	0.436±0.022
Harper et al. (Ha 71)	-0.55±0.08	0.44±0.04
Berant et al. (Be 72)	-0.42±0.10	0.432±0.006
McGowan et al. (McGo 65)	-	0.459±0.054
Milner et al. (Mi 69)	-	0.467±0.019
Present work	-0.36±0.08	0.427±0.004

The Nucleus ^{112}Cd

Reference	Q_{2+} e.b	$B(E2; \ 0^+ \rightarrow 2^+)$ $e^2.b^2$
Steadman et al. (St 70)	-0.15±0.07	0.478±0.033
Häusser et al. (Hä 71)	-0.40±0.16	0.52±0.02
McGowan et al. (McGo 65)	-	0.514±0.06
Milner et al. (Mi 69)	-	0.524±0.021
Werdecker et al (We 73)	-	0.486±0.008
Present work	-0.39±0.08	0.484±0.004

The Nucleus ^{114}Cd

Reference	Q_{2^+} e.b	$B(E2; 0^+ \rightarrow 2^+)$ $e^2.b^2$
Simpson et al. (Si 68)	+0.05±0.27	0.509±0.009
Saladin et al. (Sa 69)	-0.68±0.09	0.561±0.017
Schilling et al. (Sc 70)	-0.64±0.19	-
Kleinfeld et al. (Kl 70)	-0.40±0.12	0.498±0.027
Andreyev et al. (An 70)	-0.53±0.17	-
Berant et al. (Be 72)	-0.28±0.09	0.513±0.005
Larsen et al. (La 72)	-0.35±0.07	-
Hosoyama et al. (Ho 73)	-0.36±0.07	0.472±0.048
Gillespie et al. (Gi 76)	-0.38±0.04	0.517±0.049
McGowan et al. (McGo 65)	-	0.571±0.067
Milner et al. (Mi 69)	-	0.576±0.023
Wakefield et al. (Wa 70)	-	0.547±0.013
Pryor et al. (Pr 70)	-	0.553±0.014
Present work	-0.36±0.08	0.528±0.004

The Nucleus ^{116}Cd

Reference	Q_{2^+} e.b	B(E2; $0^+ \rightarrow 2^+$) $e^2.b^2$
Steadman et al. (St 70)	-0.90±0.25	0.653±0.035
Stokstad et al. (St 67, Ha 75)	-0.65±0.12	0.621±0.008
Hall et al. (Ha 75)	-0.64±0.12	-
McGowan et al. (McGo 65)	-	0.580±0.068
Milner et al. (Mi 69)	-	0.581±0.023
Werdecker et al. (We 73)	-	0.533±0.008
Present work	-0.42±0.08	0.532±0.004

B(E2) and Q_{2^+} in ^{114}Cd through electron scattering experiments. Although the analysis is model dependent, their results are in agreement with most of the previous measurements. In summary, it can be said that the quadrupole moment of ^{114}Cd has now been well established, and the experimental data yield a mean value of about -0.36±0.05 e.b (Kl 75).

The Nucleus ^{116}Cd

In this nucleus there have been three previous measurements. The Rutgers value, in contrast to their results for ^{110}Cd and ^{112}Cd, is large in magnitude. The earlier measurement by Stokstad et al. (St 67) was affected by vacuum deorientation; later, appropriate corrections were applied by Hall (Ha 75), giving a value of -0.65 e.b. The third measurement is from Liverpool. These measurements all yield large values for $|Q_{2^+}|$ in ^{116}Cd (table 5.1) with an average for Q_{2^+} of -0.7±0.06 e.b. However, the present result is smaller and similar in magnitude to those measured in the other cadmium isotopes.

The B(E2 ; $0^+ \to 2^+$) value for ^{116}Cd obtained in the present work is in disagreement with those determined by Stokstad et al. and Steadman et al. The average of these two measurements is 0.64±0.02 $e^2.b^2$ whereas the present value is 0.532±0.004 $e^2.b^2$. The 20% difference is surprising; however the present relative B(E2)'s are similar to those of Milner et al. (Mi 69) for all isotopes studied. In addition, the present value is in good agreement with a preliminary result, B(E2) = 0.53 $e^2.b^2$, of Werdecker et al. (We 73), and with recent Glasgow electron scattering data (Gi 76 a). The relatively large Liverpool result for $|Q_{2^+}|$ in ^{116}Cd may be due, in part, to the use in their analysis of too large a value for B(E2);$0^+ \to 2^+$).

5.2 Predictions of Simple Collective Models

The present results, in contrast to some of the earlier data, do not support the existence, in the cadmium isotopes, of quadrupole moments as large as the rotational model value. Other elements in the $Z \sim 50$ region also have Q_{2^+} values significantly smaller than the rotational value. Therefore, the theoretical emphasis on apparently large moments in ^{106,108,116}Cd shifts to smaller values which are, hopefully, more amenable to successful theoretical interpretation.

Following the discovery of the non-zero quadrupole moment in ^{114}Cd (de Bo 65), Tamura and Udagawa (Ta 66) reviewed the theories which could be applied to "vibrational type" nuclei. Some of their conclusions will be reproduced here for those cases in which the theories could yield large enough quadrupole moments. The nucleus ^{114}Cd will be used as an example, bearing in mind that the quadrupole moments in all the cadmium isotopes appear, on the basis of the present work, to be similar in value.

As outlined in chapter 1, the simple harmonic model predicts zero Q_{2^+} and the rotational model gives -0.7 e.b. The shell model prediction can be obtained from equation 1.3 by assuming that the 2^+ state in ^{114}Cd is mainly due to the proton configuration $(g_{9/2})^{-2}$. The result is Q_{2^+} = -0.10 e.b, which is small compared to the experimental values (table 5.1). The triaxial rotation-vibration coupling model of Davydov and Filipov (Da 58), in which β vibrations and a fixed non-axial deformation γ are considered, is unsuitable for nuclei which are "soft" with respect to γ vibrations. Nevertheless, using the appropriate parameters obtained from the known properties of the levels in ^{114}Cd, this model yields a value of -0.33 e.b, which is in good agreement with experiment.

Another model which can successfully reproduce large quadrupole moments together with many other properties of vibrational nuclei is that

proposed by Goldhaber and Weneser (Go 55) and Raz (Ra 59). In this model the two proton holes $(g_{9/2})^{-2}$ are coupled together and also to a harmonic vibrational core. The particle-vibration coupling (P-V-C) model has been further developed by Alaga and his co-workers (Al 67) who have performed extensive numerical calculations. The properties of this model will be further discussed in section 5.3. Tamura (Ta 65a) has proposed extending the vibrational model by including one- and two-phonon admixtures in the wave functions of the $2^{+'}$ and 2^+ states respectively. The present results will be discussed in terms of the phonon-mixing model in section 5.5.

5.3 The Particle-Vibration Coupling Model

The variation of the quadrupole moment as a function of neutron number has now been determined with a reasonable degree of confidence for Pd, Sn, Cd and Te nuclei in the mass A~100 region (Ha 75, Kl 75). In all cases the data indicate a monotonic change in Q_{2+} across the isotopes. Furthermore, in the cadmium isotopes, (as shown in the present work), and in the palladium isotopes (Ha 75), there are no discernible neutron sub-shell effects. The relative insensitivity to neutron pair addition suggests the applicability of the semi-microscopic particle-vibration coupling model (Alaga, Al 67) to the above-mentioned nuclei. The harmonic vibrational core has zero quadrupole moment and that of a single particle is small (see chapter 1). The coupling of one or more protons (or proton holes) to the vibrator effectively polarizes the core and enhances the quadrupole moment. In this picture the behaviour of the coupled system is governed by the valence protons and the effect of the addition of neutron pairs is absorbed into renormalized single proton and phonon energies (Lo 75). Thus for the closed proton shell (Z=50) tin isotopes, the measured $|Q_{2+}|$ are small (Gr 75) and insensitive to neutron number. Neutron shell effects are observed, however, in the Te isotopes, and the quadrupole moment decreases

with increasing neutron number because of the proximity of the major

closed shell at N=82 (Bo 76a).

The Hamiltonian used in the P-V-C model is of the form

$$H = H_o + H_{pair} + H_{int} \quad , \quad \quad (5.1)$$

where H_o represents the energy of the unperturbed system consisting of

a quadrupole vibrator and two proton holes (for cadmium) in a central

field. The residual interaction between the two proton holes is the pairing

interaction, and the interaction between the proton-hole cluster and the

core is given by

$$H_{int} = +k \sum_{\mu=-2}^{2} \alpha_2^{\mu} Y_2^{\mu*}(\theta,\xi) \quad , \quad \quad (5.2)$$

where k is the strength of the interaction, α_2^{μ} are the deformation parameters,

and θ and ξ are the particle coordinates. For non-zero coupling strength

k, the wavefunctions of H contain more than one phonon number and therefore,

as in the case of the phonon-mixing model, can give rise to non-zero quad-

rupole moment. The P-V-C model has been used for calculating the level

scheme and transition rates in ^{114}Cd (Al 69), Sn (Br 72) and Te (De 74)

nuclei. In the tellurium calculation it was observed that the quadrupole

moment is highly sensitive to the position of the $d_{3/2}$ single-particle

state. In ^{114}Cd only the $g_{9/2}^{-1}$, $P_{3/2}^{-1}$ and $P_{1/2}^{-1}$ hole states were included

in the calculation (curve (a) in fig. 5.2). In this case, the calculated

Q_{2+} is sensitive to the position of the $P_{1/2}^{-1}$ and $P_{3/2}^{-1}$ states, lowering of

which tends to suppress Q_{2+} in magnitude (curve (b) in fig. 5.2). The

inclusion of the $f_{5/2}^{-1}$ proton state (curve c) has even greater influence

and a large prositive quadrupole moment can be obtained depending on the

coupling strength (k) used. No such low-lying $f_{5/2}^{-1}$ state has been observed,

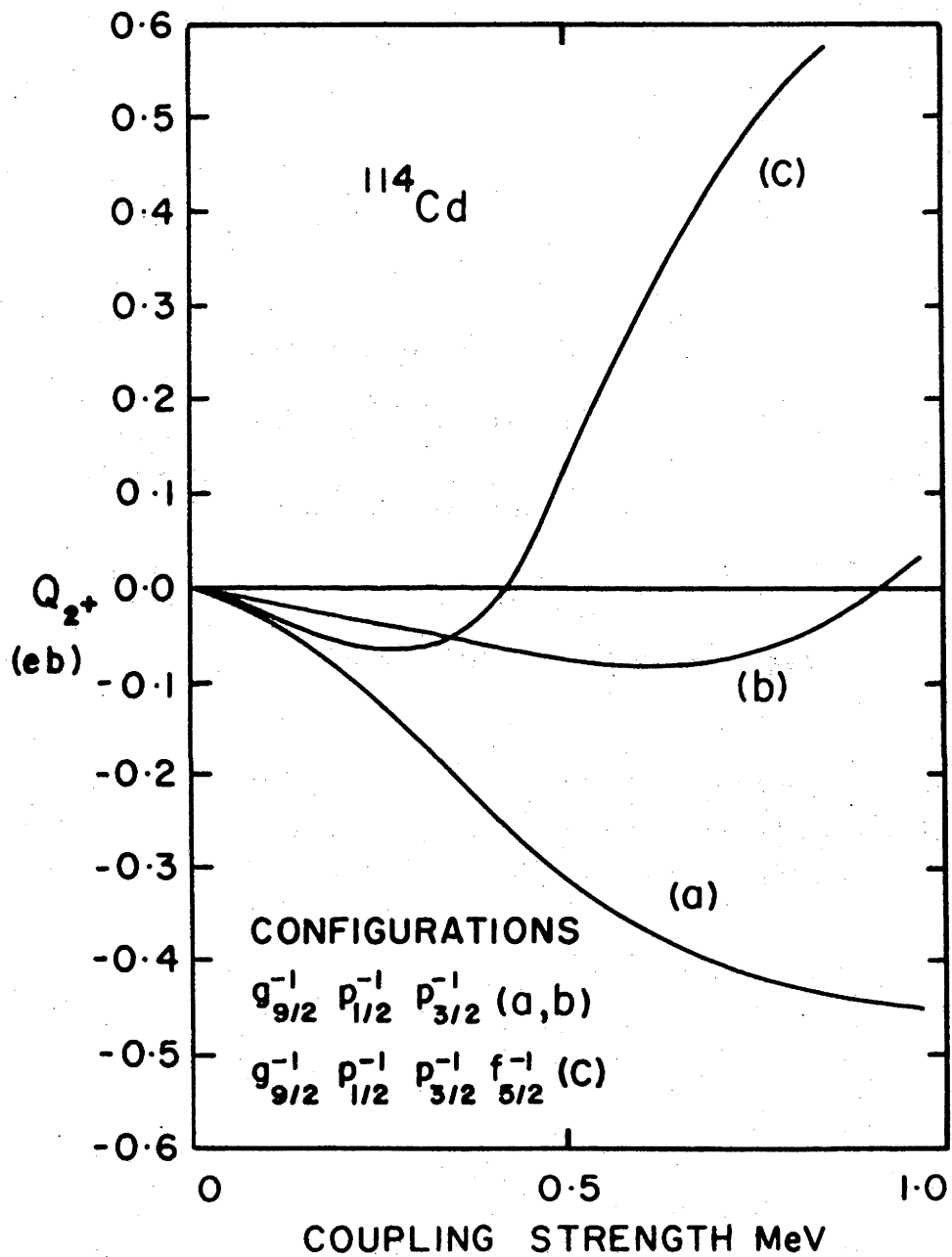however, in the neighbouring odd indium isotopes (He 74a). It appears,

Figure 5.2.   The sensitivity of Q_{2^+} to the particle-vibration coupling strength and to the various hole-states included in the calculation.   Adopted from V. Lopac (Lo 75).

therefore, that Q_{2^+} is highly sensitive to the configuration and relative energies of the proton shell model states used in the calculation.

The results of the P-V-C calculation by Alaga (Al 69) for ^{114}Cd are shown in figure 5.3 together with the experimentally determined energy spectrum (Ki 75). The sequence of "two-phonon" states 0^+, 2^+, 4^+ is reproduced but the level ordering is reversed. The third 0^+ and 2^+ states are also reproduced but at somewhat higher energy than the experimentally observed ones. The calculated E2 transition rates are listed in table 5.2 together with the experimental values. It can be seen that the overall agreement is good. Similar calculations for the other cadmium isotopes have not been done. In view of the similarities in the electromagnetic properties of the cadmium isotopes, such as transition rates and quadrupole moments and the success of the P-V-C model in ^{114}Cd, equally good results can be expected for the other cadmium isotopes.

A previous attempt by Sips (Si 71) to determine the variation of Q_{2^+} with mass in the cadmium isotopes is shown in figure 5.1 (the dashed line). The method used for the calculation was a graphical perturbation expansion in terms of the P-V-C model. The trend predicted by this calculation does not agree with the present data. However, doubt has now been cast on the validity of this calculation by Broglia et al. (Br 72).

5.4 Boson Expansion Methods

An alternative approach to the description of the properties of vibrational type nuclei comes under the general heading of "Boson-Expansion Methods". In contrast to the simple ideas outlined above for the particle-vibration coupling calculation, it is difficult to grasp the underlying physical picture or differentiate between various boson expansion

methods. The basic recipe, first proposed by Belyaev and Zelevinsky (Be 62), is to expand a microscopic Hamiltonian, written in terms of fermion creation and annihilation operators, in terms of boson creation and annihilation operators. Sorensen (So 67) has extended the method by deriving the boson Hamiltonian up to fourth order terms. Recently, this method has been further extended and refined by Kishimoto and Tamura (Ki 72), who solve exactly the equations for the coefficients of the boson expansion up to sixth order.

Both Sorensen (So 73) and Kishimoto and Tamura (Ki 76) have applied the method to the cadmium isotopes. The boson expansions used include anharmonic branches; in addition, Sorensen has included particle degrees of freedom and uses the amplitude of the interaction Hamiltonian as a variational parameter. Sorensen's results for Q_{2^+} in the cadmium isotopes are shown in figure 5.1. The calculation is in agreement with the earlier values for ^{106,108,116}Cd, but is clearly in disagreement with the present results and with those of Hall et al. (Ha 74) for ^{106,108}Cd. The level scheme predicted by Sorensen for ^{114}Cd is shown in figure 5.3. The dashed lines represent the "particle" states and the solid lines the "vibrational" states. It can be seen that the fit, compared to that predicted by the particle-vibration coupling model, is poor.

In a recent paper Kishimoto and Tamura (Ki 76) have calculated the properties of a dozen nuclei by the boson expansion method. The calculations were taken up to fourth order and non-collective branches were included as well. They were able to obtain very good agreement with experiment in all of the nuclei studied, which range from ^{110}Pd to ^{198}Hg and include ^{114}Cd. For example, they were able to reproduce the vibration-to-rotation transition observed in the samarium isotopes and the prolate-to-oblate transition in the Os-Pt region. For ^{198}Hg, they predict a
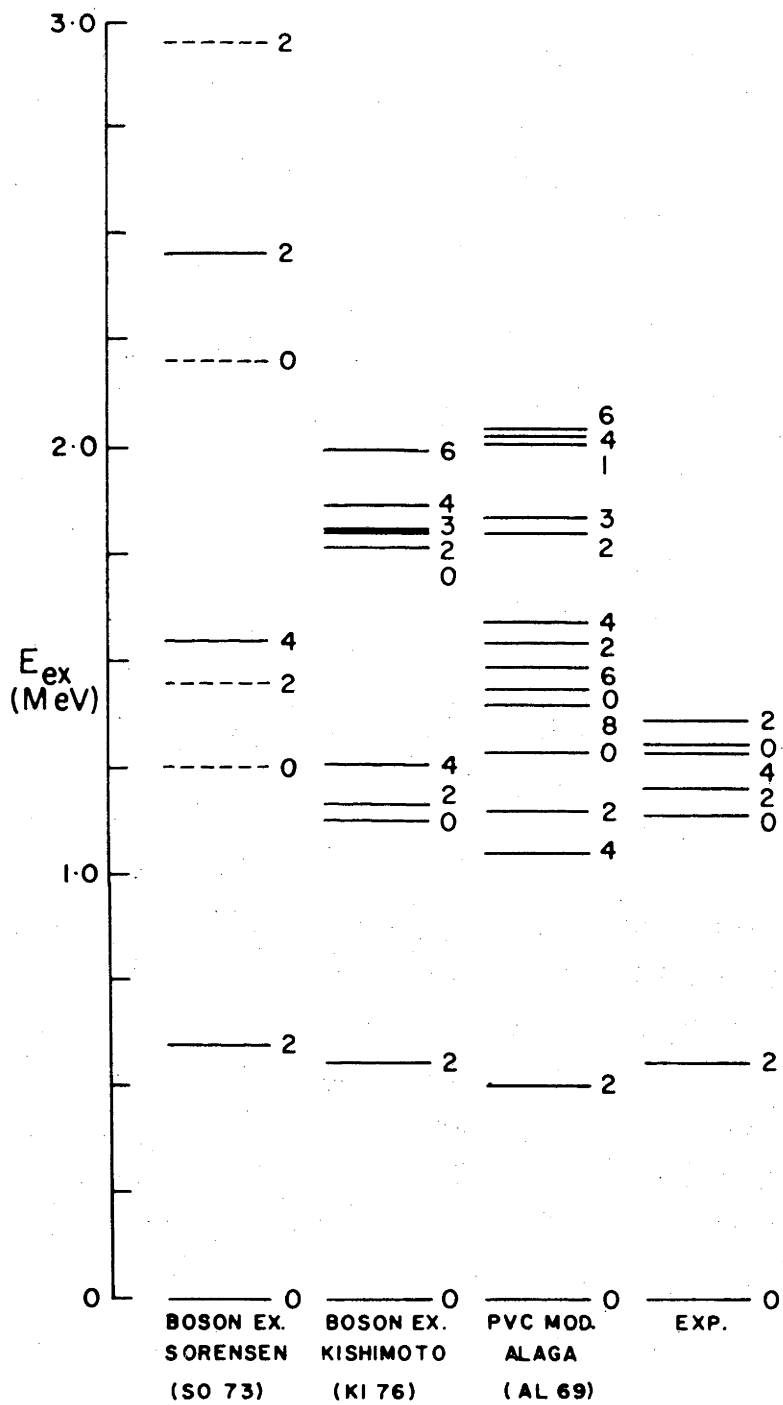
Figure 5.3. The experimentally determined energy spectrum
            of ^{114}Cd compared with calculations using
            boson expansion methods and the particle-
            vibration coupling model.

Table 5.2. The theoretical and experimental values of
$B(E2; J_i \rightarrow J_f)$ and Q_{2^+} in $e^2.b^2$ and e.b respectively.

J_i	J_f	Boson Expansion Method (Ki 76)	Particle-Vibration Coupling (Al 69)	Experiment
2	0	0.103	0.112	0.106±0.001
2'	0	0.0023	0.003	0.0019±0.0003
2	2	-0.379	-0.329	-0.36±0.08
0'	2	0.135	0.067	0.096±0.002
2'	2	0.137	0.134	0.08±0.02
4	2	0.182	0.203	0.212±0.001

positive quadrupole moment (which agrees with the prediction of the particle-vibration coupling model, Co 67). However, no experimental data exist in this case.

The spectrum for ^{114}Cd, calculated by Kishimoto and Tamura, is shown in figure 5.3, and the electromagnetic properties are listed in table 5.2. The level sequence in the two-phonon region is reproduced and the electromagnetic properties calculated are in good agreement with experiment. The third 2^+ and 0^+ states are missing since Kishimoto and Tamura do not explicitly include particle degrees of freedom in their calculation. However, they claim that a preliminary calculation in which the particle branches are included, agrees well with the experimentally observed level scheme (Ta 75).

5.5 The Phonon-Mixing Model

Tamura (Ta 65a) has extended the vibrational model by assuming that the wave functions of the first excited (one-phonon) and second excited (two-phonon) 2^+ states contain both one and two phonon components. Restricting any admixtures to those which differ in phonon number N by one, and ignoring multipolarities λ higher than quadrupole, the wave functions of the various states can be written (in notation $|N,J\rangle$) as

$$0^+ \text{ ground state, } |0^+\rangle = |0,0\rangle \quad ,$$
$$\text{first excited } 2^+ \text{ state, } |2^+\rangle = \sqrt{1-x^2}\,|1,2\rangle + x|2,2\rangle \quad ,$$
$$\text{second excited } 2^+ \text{ state, } |2^{+\prime}\rangle = x|1,2\rangle - \sqrt{1-x^2}\,|2,2\rangle \quad , \quad (5.3)$$
$$\text{first excited } 0^+ \text{ state, } |0^{+\prime}\rangle = |2,0\rangle \quad ,$$
$$\text{first excited } 4^+ \text{ state, } |4^+\rangle = |2,4\rangle \quad ,$$

where $|x|^2$ is the mixing parameter. In order to calculate the E2 matrix elements between the various states, the E2 transition operator is assumed

to be of the form

$$M(E2) = \alpha(b + b^\dagger) \quad , \tag{5.4}$$

where $b^\dagger$ and b are the phonon creation and annihilation operators respectively, and α is a constant. Given the matrix elements for the operator $b^\dagger$ (Ra 59, Al 69), it is easy to work out the reduced transition probabilities. The matrix elements of $b^\dagger$ relevant to the present model are

$$<1,2 \| b^\dagger \| 0,0> = \sqrt{5} \quad ,$$
$$\tag{5.5}$$
$$<2,J \| b^\dagger \| 1,2> = \sqrt{2(2J + 1)} \quad .$$

The reduced matrix elements for the various transitions are listed in table 5.3, together with the experimental values for all cadmium isotopes. The $(2^+ \rightarrow 0^+)$ and $(2^+ \rightarrow 2^+)$ matrix elements are from the present work and the other matrix elements were obtained from McGowan et al. (McGo 65), Milner et al. (Mi 69), and Grabowski et al. (Gr 73). Since the present results for Q_{2^+} differ significantly from some previous data, it is of interest to compare these with the predictions of the phonon-mixing model. A particularly transparent way of doing this is to plot the ratio $<J \| M(E2) \| J'>_{calc} / <J \| M(E2) \| J'>_{exp}$ versus the mixing parameter $|x|^2$, as was done by Häusser et al. for ^{112}Cd (Hä 71). The constant α was chosen to match the experimental E2 transition probabilities; its value, 31 e.fm^2, was kept constant for all the isotopes. The results are shown in figure 5.4. In ^{112}Cd and ^{114}Cd there is a third 2^+ state; the phonon-mixing model is unable to account for such states and their contribution has been added to those of $2^{+'}$ states. Similarly in ^{114}Cd the matrix elements of the $0^{+'}$ and $0^{+''}$ states have been combined before comparing with the calculation. Only the $(2^{+'} \rightarrow 0)$ matrix elements in ^{112,114}Cd are significantly affected by this procedure (table 5.3). The non-observation

Table 5.3. The reduced matrix elements in the cadmium isotopes and the corresponding anharmonic model expressions.

J_i	J_f	$\langle J_i \| M(E2) \| J_f \rangle$ e.fm²	The experimental values of the reduced matrix elements in e.fm²					
			^{106}Cd	^{108}Cd	^{110}Cd	^{112}Cd	^{114}Cd	^{116}Cd
2	0	$\sqrt{5}\sqrt{(1-x^2)}\alpha$	61.97±0.3	63.80±0.3	65.35±0.3	69.57±0.3	72.66±0.3	72.94±0.3
2'	0	$\sqrt{5}x\alpha$	19±1	17±1	15±1	10±1	9.8±0.8	14±1
2''	0		–	–	–	7±1	8.4±0.7	–
2'	2	$-(2x^2-1)\sqrt{10}\alpha$	32±5	53±8	71±10	54±5	64±7	60±8
2''	2		–	–	–	4±3	2±1	–
4	2	$3\sqrt{2}\sqrt{(1-x^2)}\alpha$	111±7	106±6	113±7	131±8	138±8	133±14
0'	2	$\sqrt{2}\sqrt{(1-x^2)}\alpha$	–	–	–	–	31±3	32±3
0''	2		–	–	–	–	31±5	–
2	2	$2x\sqrt{(1-x^2)}\sqrt{10}\alpha$	37±11	59±11	48±11	52±11	48±11	55±11
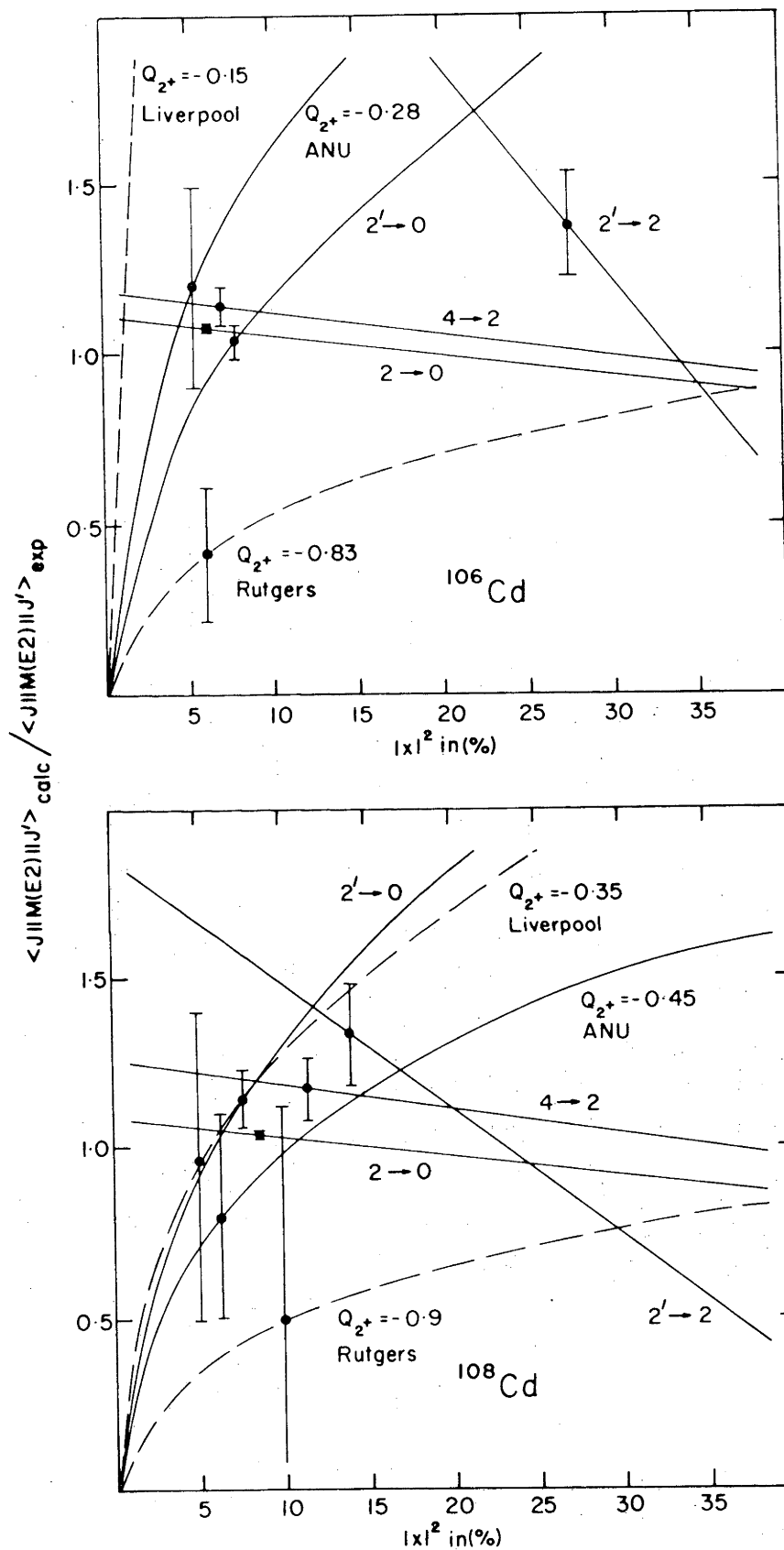
Figure 5.4. Ratios of calculated and experimental reduced E2 matrix
elements in the even mass cadmium isotopes. A common value
of $\alpha=31$ e.fm^2 was used for all isotopes. Error bars are
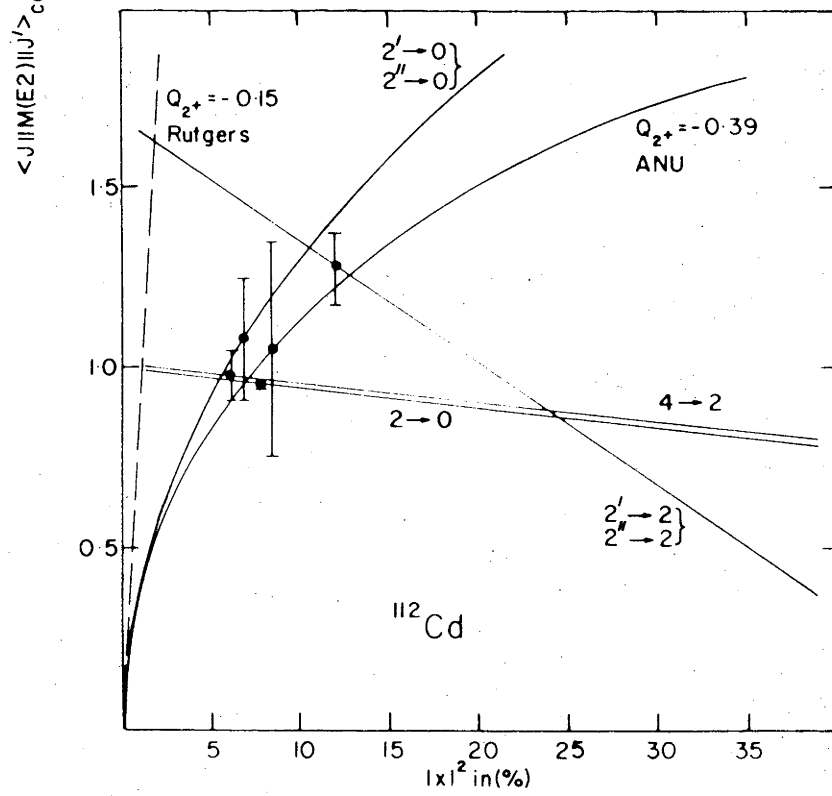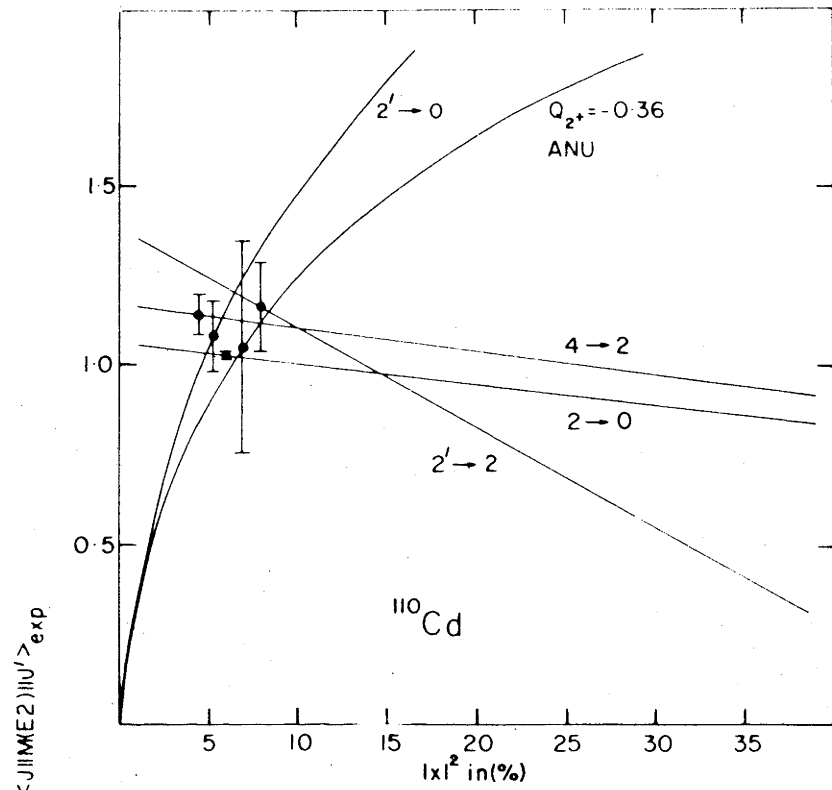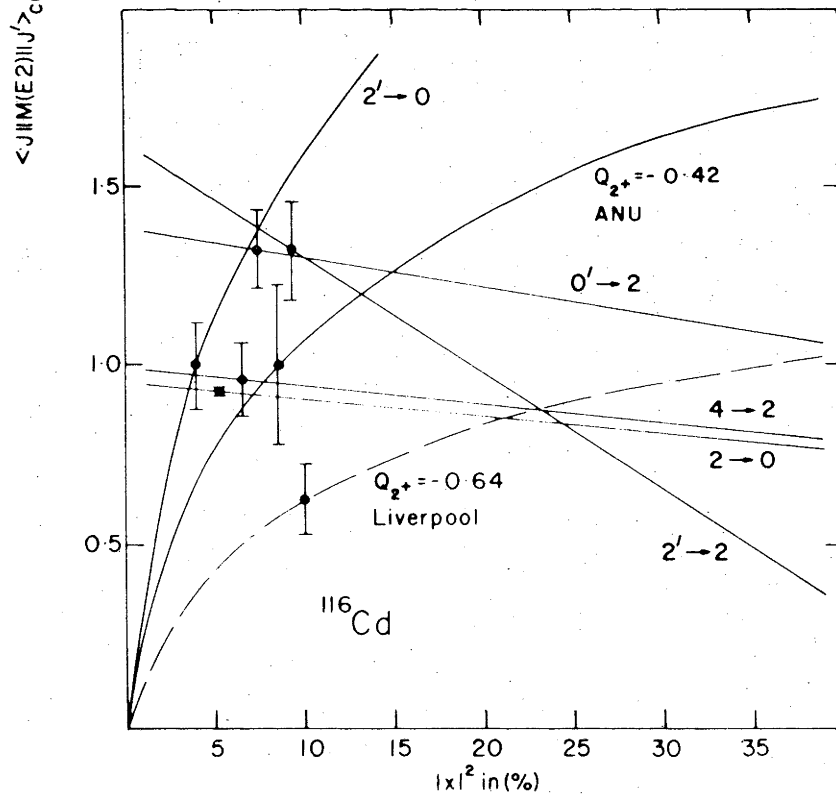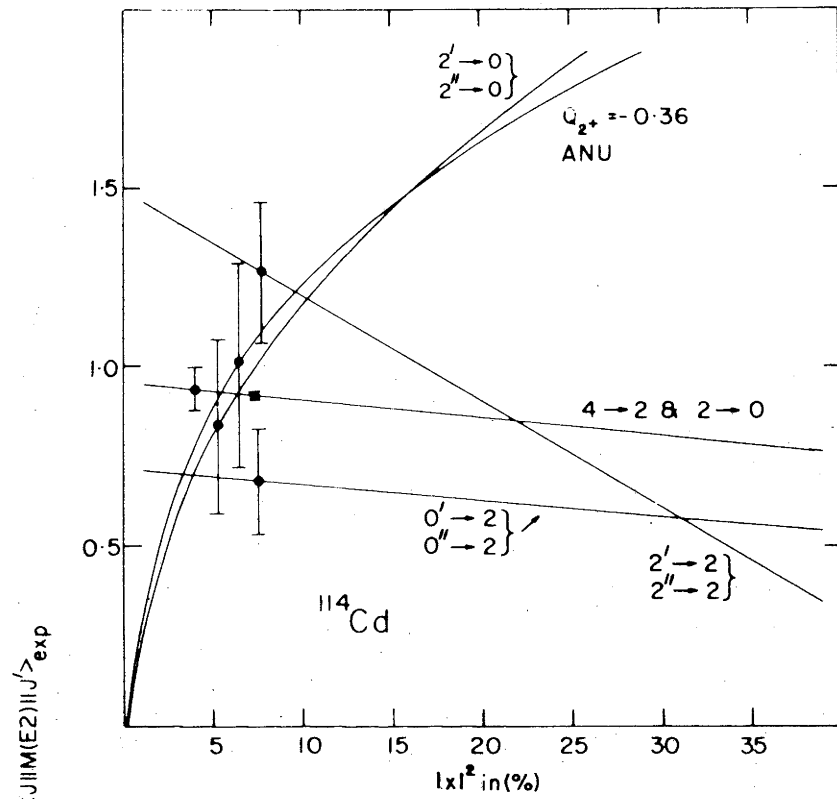indicated at arbitrary values of $|x|^2$; each line represents
a band with the width determined by the length of the error
bar.

of similar $2^{+''}$ states in the other cadmium isotopes (see fig. 4.15 and

Sp 76) and the similarity of the $(2^{+'}\rightarrow 0)+(2^{+''}\rightarrow 0)$ matrix elements (table

5.3) in all of the cadmium isotopes are arguments in favour of such a

combination. The error bars in figure 5.4 were placed at arbitrary points

along each curve and represent bands with the width determined by the

length of the error bar. The Liverpool results for Q_{2+} in $^{106,108,116}Cd$

and the Rutgers data for $^{106,108,112,116}Cd$ are also shown for comparison.

A striking pattern is revealed in these plots; with a few

exceptions, which will be discussed below, all the curves for each isotope

are coincident, within the error bands, at a mixing value which ranges

between 5 to 10%. Another feature is that the model is highly sensitive

to the value of the quadrupole moment. For example, in $^{106,108,116}Cd$ the

large values of $|Q_{2+}|$ obtained prior to the present work are inconsistent

with the rest of the matrix element ratios. Similar comments apply for

values of $|Q_{2+}|$ less than about 0.2 e.b. In contrast to these, the

present results for all of the cadmium isotopes, with the possible

marginal exception of ^{108}Cd, are in excellent agreement with the model.

A criticism of this simple model, in the past, has been the following:

"The difficulty with this naive model was that the ratio $S = B(E2;2^{+'}\rightarrow 0^{+})/$

$B(E2;2^{+'}\rightarrow 2^{+}) = 0.14$ predicted by this model was about one order of magni-

tude too large compared with the experimental value (in ^{114}Cd) $S = 0.015$"

(Tamura and Kishimoto, Ta 73). On the basis of the present data, the

model prediction for S with 7% mixing is 0.05, the experimental values

S_{exp} for each isotope are listed below.

Isotope	106	108	110	112	114	116
S_{exp}	0.35±0.13	0.10±0.03	0.05±0.02	0.09±0.01 0.03±0.01	0.08±0.02 0.02±0.003	0.05±0.02

The second entry for ^{112,114}Cd does not include the $2^{+''}$ state contribution.
It is clear from these figures that except for ^{106}Cd, the experimental and
model predictions for S (for a fixed value of α and $|x|^2$) are in reasonable
agreement. Therefore, using the present results for B(E2) and Q_{2^+}, the
anharmonic vibrational model is seen to be in substantial agreement with
most of the electromagnetic properties of the cadmium isotopes. Further
support for this model can be found in the results of electron scattering
measurements (Ho 73, Gi 76). The quadrupole moment of ^{114}Cd determined
from these, using the phonon-mixing model, is in good agreement with those
values obtained through reorientation measurements.

The level scheme for ^{114}Cd has been calculated in terms of a
similar, but more sophisticated, model, which includes up to third order
anharmonicities in the interaction Hamiltonian, by Sips and Lopac (Si 70).
The model has four parameters and up to seven phonons were included. Sips
and Lopac, in agreement with the results of the phonon mixing model
presented above for S and in figure 5.4, find that "large" quadrupole
moments and "small" cross over transitions are not incompatible. The
level scheme calculated for ^{114}Cd up to the 2-phonon region is in reason-
able agreement with experiment.

The anomalous $2^{+'} \rightarrow 2^+$ transition matrix element in ^{106}Cd (table
5.3, fig. 5.4) is that recently obtained by Grabowski et al. (Gr 73).
In comparison with the other cadmium isotopes, this value is small. In
fact, the previously preferred result of Milner et al. (Mi 69) is much
more consistent with the data shown in figure 5.4.

5.6 Trends in Level Energies, Transition Probabilities, and Quadrupole Moments in Pd, Te and Cd Nuclei

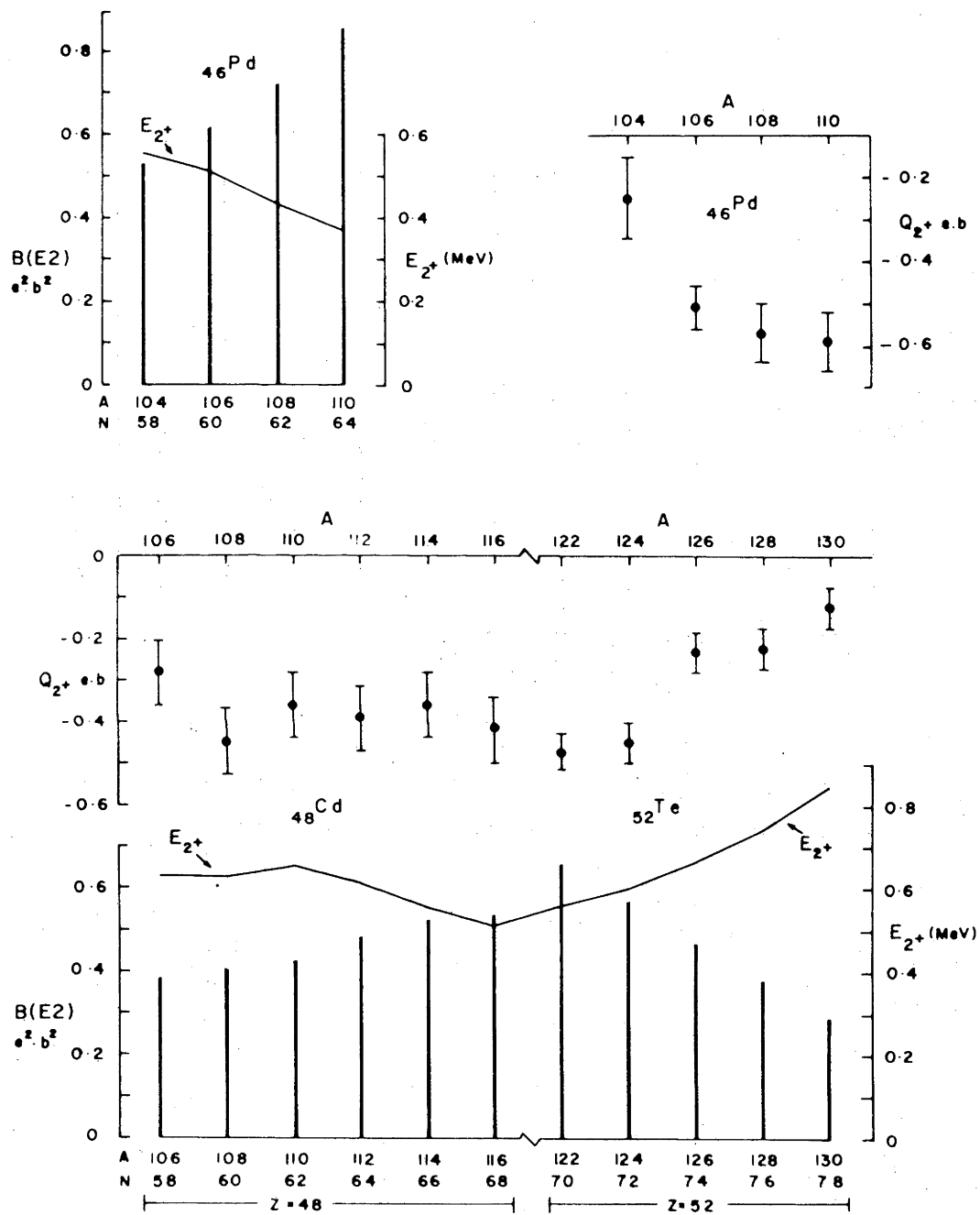A summary of B(E2; $0^+ \rightarrow 2^+$) and Q_{2^+} values, together with level

Figure 5.5. Summary of the experimental E_{2^+}, $B(E2; 0^+ \to 2^+)$ and Q_{2^+} values in the Pd, Cd, and Te isotopes.

energies E_{2^+}, are shown in figure 5.5 for Pd, Te and Cd isotopes. The

Te and Pd data were obtained from compilations by Bockisch et al. (Bo

76a) and by Hall (Ha 75) respectively. The Cd data are from the present

work.

The results of the present and previous determinations of Q_{2^+}

in the cadmium isotopes are summarized in figure 5.1. Prior to the present

work the only attempt to measure systematically the variation of Q_{2^+} with

A for all the even cadmium isotopes was made by Steadman et al. (St 70).

They obtained a variation with mass similar to that shown for reference

(Ch 72) in figure 5.1. Steadman et al. suggested that the minimum in $|Q_{2^+}|$

observed at ^{112}Cd was due to the closure of the $g_{7/2}$ neutron subshell.

However, there is no indication of neutron subshell effects in the present

data for the cadmium isotopes, or as pointed out by Hall et al. (Ha 74),

in the palladium isotopes.

The recent results of Hall et al. (Ha 74, Ha 75) at Liverpool

for ^{106}Cd, ^{108}Cd and ^{116}Cd suggest a monotonic increase in $|Q_{2^+}|$ with

mass number. This has been interpreted (Ha 75) as indicating a trend

from vibrational to rotational type nuclei, in accord with the observed

trend of excitation energies E_{2^+} and the B(E2; $0^+ \to 2^+$) values (fig. 5.5).

Such a trend is quite pronounced in the Te isotopes because of the

proximity of the N=82 closed shell. A similar trend exists in the Pd

isotopes, although it is not as pronounced as in the Te nuclei. The

difference in B(E2; $0^+ \to 2^+$) and E_{2^+} values in going from ^{106}Cd to ^{116}Cd

is even smaller than for the Pd isotopes. Therefore, it might be expected

that the variation of Q_{2^+} with A in cadmium would also be small. The

experimental data show that this is so.

5.7 Conclusion

The present results for the quadrupole moments of the cadmium isotopes, contrary to those of Steadman et al. (St 70) and Kleinfeld et al. (Kl 70), and to the boson-expansion calculation of Sorensen (So 73), show no evidence of any neutron subshell effects. The present result for ^{114}Cd is in good agreement with the value adopted by Christy and Häusser (Ch 72) and with the more recent value reported by Larsen et al. (La 72) (table 5.1). This indicates that, in addition to giving reliable relative values for quadrupole moments, the present results are also accurate in absolute magnitude.

As discussed in sections 5.3 and 5.4, the particle-vibration coupling model (Al 69) and the boson-expansion method of Kishimoto and Tamura (Ki 76) appear to reproduce successfully many properties of ^{114}Cd. A more exacting test of these theories would be a calculation to reproduce the variation of Q_{2^+} in the cadmium isotopes with neutron number.

The phonon-mixing model calculation in section 5.5 shows that most of the electromagnetic properties of the one-phonon and two-phonon states can be reproduced with a single value of α and $|x|^2$ (including the cross-over $2^{+'} \to 0^+$ transition). This is indicative of a uniform vibrational character for all the cadmium isotopes. The results of the alpha-particle scattering experiment (Sp 76), briefly mentioned in chapter 4, are displayed in a composite diagram in figure 5.6. The variation of the various cross sections with mass number relative to the elastic yield $(\sum J^\pi / \sum 0^+)$ and the double ratio $(\sum J^\pi / \sum 0^+)/B(E2;\ 0^+ \to 2^+)$ are shown in figure 5.7. The striking regularity of the one-quadrupole phonon and one-octupole phonon excitations is clearly evident. These data strongly support the uniform character of vibrational excitations in the cadmium isotopes.

It is, therefore, not surprising that the quadrupole moments in the cadmium isotopes also show no significant variation with mass number.
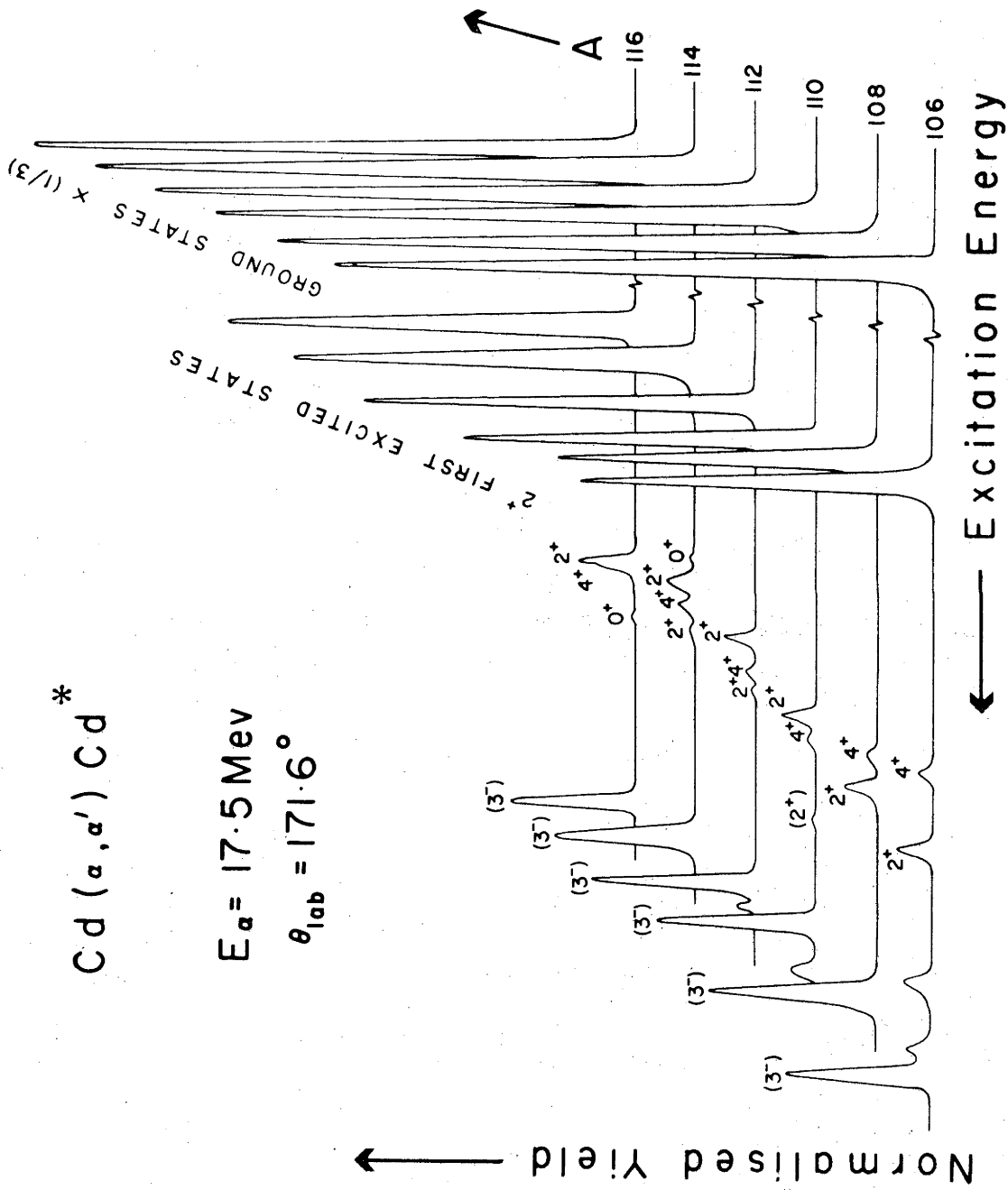
Figure 5.6. Spectra of the even-mass cadmium isotopes obtained at a bombarding energy of 17.5MeV and laboratory angle of 171.6°. Contributions of impurity isotopes have been subtracted from the data.
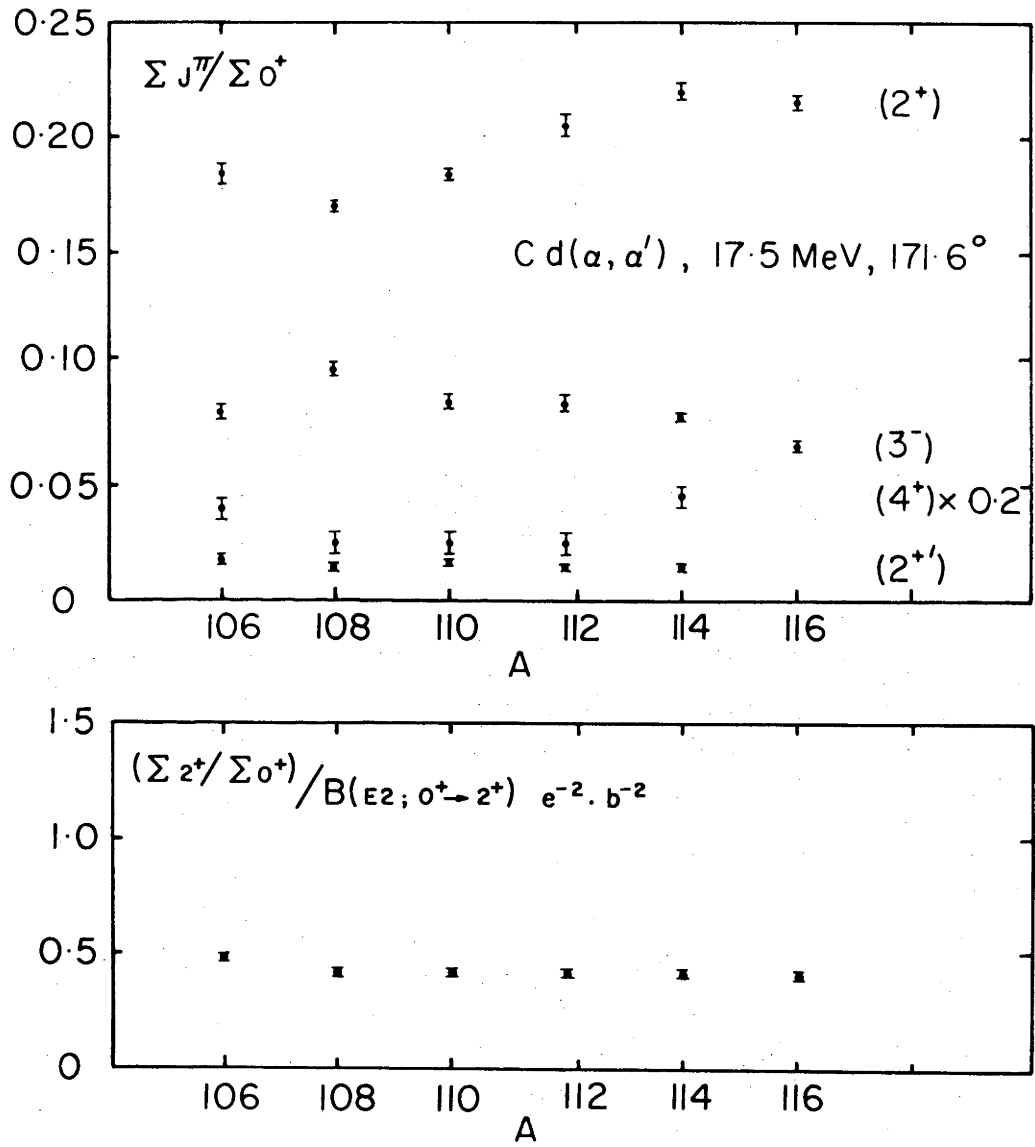
Figure 5.7. The ratio $\sum J^{\pi}/\sum 0^+$ plotted for various states in the even-mass stable cadmium isotopes together with the double ratio $(\sum 2^+/\sum 0^+)/B(E2;\ 0^+\rightarrow 2^+)$.

REFERENCES

(Al 67)   G. Alaga, F. Krmpotic and V. Lopac, Phys. Lett. <u>24B</u> (1967) 537.

(Al 69)   G. Alaga, "Struttura dei nuclei e reazioni nucleari", Proc. of the International School of Physics "Enrico Fermi" Corso XL. Ed. by M. Jean (Academic Press, New York, 1969).

(Al 56)   K. Alder, A. Bohr, T. Huus, B. Mottelson and A. Winther, Rev. Mod. Phys. <u>28</u> (1956) 432.

(Al 69)   K. Alder and H.K.A. Pauli, Nucl. Phys. <u>A128</u> (1969) 193.

(Al 72)   K. Alder, F. Roesel and R. Morf, Nucl. Phys. <u>A186</u> (1972) 449.

(Al 75)   K. Alder and A. Winther, Electromagnetic excitation, (North-Holland, Amsterdam, 1975).

(An 70)   D. S. Andreyev, G. M. Gusinsky, K. I. Erokhir, M. F. Kudojarov, I. Kh. Lemberg and I. V. Chuganov, Phys. Lett. <u>32B</u> (1970) 187.

(Ar 70)   H. Arenhövel and J. M. Maison, Nucl. Phys. <u>A147</u> (1970) 305.

(Be 62)   H. J. Behrend and D. Budnick, Z. Phys. <u>168</u> (1962) 155.

(Be 62)   S. T. Belyaev and V. G. Zelevinsky, Nucl. Phys. <u>39</u> (1962) 582.

(Be 72)   Z. Berant, R. A. Eisenstein, Y. Horowitz, U. Smilansky, P. N. Tandon, J. S. Greenberg, A. M. Kleinfeld and H. G. Maggi, Nucl. Phys. <u>A196</u> (1972) 312.

(Be 69)   P. R. Bevington, Data reduction and error analysis for the physical sciences, (McGraw-Hill, New York, 1969).

(Be 70)   R. Beyer, R. P. Scharenberg and J. Thomson, Phys. Rev. <u>C2</u> (1970) 1469.

(Bl 72)   J. Bleck, R. Bott, H. Hass, W. Ribbe and W. Zeitz, Phys. Rev. Lett. <u>29</u> (1972) 1371.

(Bo 76)   A.Bockisch, P. Dickers, W. Klein and A. M. Kleinfeld, Nucl.
            Instr. 135 (1976) 145.

(Bo 76a)   A. Bockisch and A. M. Kleinfeld, Nucl. Phys. A261 (1976) 498.

(Bo 75)   E. Bodensted, The electromagnetic interaction in nuclear
            spectroscopy, ed. W. D. Hamilton, (North-Holland, Amsterdam,
            1975) p. 735.

(Bo 69)   A. Bohr and B. R. Mottelson, Nuclear structure, vol. 1, (W.A.
            Benjamin, Inc., New York, 1969) p. 7.

(Bo 69a)   A. Bohr and B. R. Mottelson, Nuclear structure, vol. 1 (W.A.
            Benjamin, Inc., New York, 1969) p. 341.

(Br 56)   G. Breit and J. P. Lazarus, Phys. Rev. 100 (1955) 942, and
            G. Breit, R. L. Gluckstern and J. E. Russel, Phys. Rev. 103
            (1956) 727.

(Br 72)   R. A. Broglia, S. Landowne and A. Winther, Phys. Lett. 40B
            (1972) 293.

(Ca 69)   B. Carnahan, H. A. Luther and J. O. Wilkes, Applied numerical
            methods, (John Wiley and Sons, Inc., New York, 1969).

(Ch 72)   A. Christy and O. Häusser, Nucl. Data Tables 11 (1972) 281.

(Cl 69)   D. Cline, H. S. Gertzman, H. E. Gove, P. M. Lesser and J. J.
            Schwarts, Nucl. Phys. A133 (1969) 445.

(Co 71)   B. L. Cohen, Concepts of nuclear physics, (McGraw-Hill, New
            York, 1971).

(Co 67)   A. Covello and G. Sartoris, Nucl. Phys. A104 (1967) 189.

(Da 68)   A. S. Davidov and G. T. Filippov, Nucl. Phys. 8 (1958) 237.

(deBo 65)   J. de Boer, R. G. Stokstad, G. D. Symons and A. Winther, Phys.
            Rev. Lett. 14 (1965) 564.

(deBo 68)   J. de Boer and J. Eichler, Advances in Nuclear Physics, eds. M. Barager and E. Vogt, vol. 1 (Plenum Press, New York, 1968) p. 1.

(deCa 71)   N. V. de Castro Faria, J. Charbonneau, L. L'écuyer and R.J.A. Lévesque, Nucl. Phys. A174 (1971) 37.

(De 74)   E. Degrieck and G. Vanden Berghe, Nucl. Phys. A231 (1974) 141.

(De 69)   S. Devons and I. Duerdoth, Advances in nuclear physiscs, eds. M. Baranger and E. Vogt, vol. 2 (Plenum Press, New York, 1969) p. 295.

(Ei 70)   J. M. Eisenberg, W. Greiner, Excitation mechanisms of the nucleus (North-Holland, Amsterdam, 1970).

(En 74)   J. B. A. England, Techniques in nuclear structure physics, part 2 (Macmillan, London, 1974) p. 313.

(Es 76)   M. T. Esat, D. C. Kean, R . H. Spear and R. A. I. Bell, Phys. Lett. 61B (1976) 242.

(Fa 76)   C. Fahlander, L. Hasselgren, J. E. Thun, A. Bockisch, A. M. Kleinfeld, A. Gelberg and K. P. Lieb, Phys. Lett. 60B (1976) 347.

(Fe. 65)   H. Frauenfelder and R. M. Steffen, Alpha-, beta- and gamma-ray spectroscopy, ed. K. Siegbahn, vol. 2 (North-Holland, Amsterdam, 1965) p. 997.

(Fr 76)   J. M. Freeman, Nucl. Instr. 134 (1976) 153.

(Gi 74)   D. R. Gill, N. Ahmed, W. J. McDonald, and G. C. Neilson, Phys. Rev. Lett. 16 (1974) 889.

(Gi 76)   W. A. Gillespie, R. P. Singhal, S. W. Brain, A. Johnston and E. W. Lees, J. Phys. G2 (1976) 185.

(Gi 76a)   W. A. Gillespie, private communication.

(Go 55)   G. S. Goldhaber and J. Weneser, Phys. Rev. 98 (1955) 212.

(Go 68)   G. Goldring, Hyperfine structure and nuclear radiations, eds.
            E. Matthias and D. A. Shirley, (North-Holland, Amsterdam,
            1968) p. 640.

(Gr 73)   Z. W. Grabowski and R. L. Robinson, Nucl. Phys. A206 (1973) 633.

(Gr 75)   R. Graetzer, S. M. Cohick and J. X. Saladin, Phys. Rev. C12
            (1975) 1462.

(Gr 71)   L. Grodzins and O. Klepper, Phys. Rev. C3 (1971) 1019.

(Gr 73)   L. Grodzins, B. Herskind, D. R. S. Somayajuln and B. Skaali,
            Phys. Rev. Lett. 30 (1973) 453.

(Ha 74)   I. Hall, M. F. Nolan, D. J. Thomas and M. J. Throop, J. Phys.
            A7 (1974) 50.

(Ha 75)   I. Hall, Proc. Topical Conf. on problems of vibrational nuclei,
            Zagreb, 1974, ed. G. Alaga, V. Paar and L. Sips (North-Holland,
            Amsterdam, 1975) p. 385.

(Ha 47)   A. O. Hansen and J. L. McKibben, Phys. Rev. 72 (1947) 673.

(Ha 71)   R. P. Harper, A. Christy, I. Hall, I. M. Naqib and B. Wakefield,
            Nucl. Phys. A162 (1971) 161.

(Ha 76)   L. Hasselgren, C. Fahlander, F. Falk, L. O. Edvardson, J. E.
            Thun and B. S. Ghuman, Nucl. Phys. A264 (1976) 341.

(Hä 71)   O. Häusser, T. K. Alexander, A. B. McDonald and W. T. Diamond,
            Nucl. Phys. A175 (1971) 593.

(Hä 73)   O. Häusser, A. B. McDonald, T. K. Alexander and A. J. Ferguson,
            Nucl. Phys. A212 (1973) 613.

(Hä 74)   O. Häusser, Nuclear spectroscopy and reactions, ed. J. Cerny,
            part C (Academic Press, New York, 1974) p. 55.

(He 73)   A. W. Herman, L. A. McNelles and J. L. Campbell, Nucl. Instr.
            109 (1973) 429.

(He 71)   B. Herskind, Hyperfine interactions in excited nuclei, ed.
            G. Goldring and R. Kalish, vol. 1 (Gordon and Breach, New York,
            1971) p. 1.

(He 74)   B. Herskind and M. Neiman, Hyperfine interactions studied in
            nuclear reactions and decay, Uppsala, 1974, eds. E. Karlsson
            and R. Wäppling, p. 599.

(He 74)   W. H. A. Hesselink, B. R. Kooistra, L. W. Put, R. H. Siemssen
            and S. Y. Van Der Werf, Nucl. Phys. A226 (1974) 229.

(Ho 71)   P. E. Hodgson, Nuclear reactions and nuclear structure,
            (Clarendon Press, Oxford, 1971) chapter 13.

(Ho 73)   K. Hosoyama, Y. Torizuka, Y. Kawazoe and H. Ui, Phys. Lett.
            30 (1973) 388.

(Hu 58)   D. J. Hughes and R. B. Schwartz, Neutron cross sections, 2nd
            ed. Brookhaven Natl. Lab. Rept. BNL-325 (1958).

(Is 69)   V. I. Isakov and I. Kh. Lemberg, Jetp. Lett. 9 (1969) 438.

(Ke 75)   D. C. Kean, private communication.

(Ki 75)   H. J. Kim, Nucl. Data Sheets 16 (1975) 107.

(Ki 72)   T. Kishimoto and T. Tamura, Nucl. Phys. A192 (1972) 246.

(Ki 76)   T. Kishimoto and T. Tamura, to be published.

(Kl 70)   A. M. Kleinfeld, J. O. Rogers, J. Gastebois, S. G. Steadman,
            and J. de Boer, Nucl. Phys. A158 (1970) 81.

(Kl 75)   A. M. Kleinfeld, Proc. Topical Conf. on problems of vibrational
            nuclei, Zagreb, 1974, ed. G. Alaga, V. Paar and L. Sips (North-
            Holland, Amsterdam, 1975) p. 363.

(Ku 69)   K. Kumar, Phys. Lett. 29B (1969) 25.

(La 72)   R. D. Larsen, J. A. Thomson, R. G. Kerr, R. P. Scharenberg and
            W. R. Lutz, Nucl. Phys. A195 (1972) 119.

(Le 44)   K. Levenberg, Quart. Appl. Maths. 2 (1944) 1964.

(Le 57)   J. S. Levinger, Phys. Rev. 107 (1957) 554.

(Li 72)   J. W. Lightbody Jr., Phys. Lett. 38B (1972) 475.

(Lo 65)   H. M. Lobenstein, D. W. Mingay and C. S. Zaidins, Nucl. Instr.
            33 (1965) 175.

(Le 75)   V. Lopac, Proc. Topical Conf. on problems of vibrational nuclei,
            Zagreb, 1974, ed. G. Alaga, V. Paar and L. Sips (North-Holland,
            Amsterdam, 1975) p. 396.

(Ma 66)   J. B. Marion, Rev. Mod. Phys. 38 (1966) 660.

(McGo 65)   F. K. McGowan, R. L. Robinson, P. H. Stelson and J. L. C. Ford,
            Nucl. Phys. 66 (1965) 97.

(McGo 74)   F. K. McGowan and P. H. Stelson, Nuclear spectroscopy and
            reactions, ed. J. Cerny, part C (Academic Press, New York, 1974)
            p. 3.

(Me 62)   A. Messiah, Quantum mechanics, vol. 2 (North-Holland, Amsterdam,
            1962) p. 722.

(Mi 69)   W. T. Milner, F. K. McGowan, P. H. Stelson, R. L. Robinson
            and R. O. Sayer, Nucl. Phys. A129 (1969) 687.

(Mo 66)   J. M. Morris and T. R. Ophel, Nucl. Instr. 40 (1966) 245.

(Mo 69)   J. M. Mossis and T. R. Ophel, Nucl. Instr. 68 (1969) 344.

(Ne 75)   C. S. Newton, Ph.D. thesis, Australian National University,
            Canberra, 1975.

(Ne 75)   J. O. Newton, The electromagnetic interaction in nuclear
            spectroscopy, ed. W. D. Hamilton (North-Holland, Amsterdam,
            1975) p. 237.

(Op 71)   T. R. Ophel, Notes on nuclear spectroscopy instrumentation, ANU-P/502.

(Pe 57)   I. Pearlman and J. O. Rasmussen, Handbuch der Physik, vol. 42, ed. S. Flügse (Springer-Verlag, Berlin, 1957) p. 151.

(Pr 75)   M. A. Preston and R. K. Bhaduri, Structure of the nucleus (Addison-Wesley, London, 1975) p. 340.

(Pr 70)   R. J. Pryor, F. Rösel, J. X. Saladin and K. Alder, Phys. Lett. 32B (1970) 26.

(Ra 73)   R. S. Raghavan, P. Raghavan and E. N. Kaufmann, Phys. Rev. Lett. 31 (1973) 111.

(Ra 50)   J. Rainwater, Phys. Rev. 79 (1950) 432.

(Ra 71)   S. Raman and H. J. Kim, Nucl. Data Sheets 6 (1971) 39.

(Ra 71a)   S. Raman and H. J. Kim, Nucl. Data Sheets 5 (1971) 181.

(Ra 59)   B. J. Raz, Phys. Rev. 114 (1959) 1116.

(Ro 69)   R. L. Robinson, F. K. McGowan, P. H. Stelson, W. T. Milner and R. O. Sayer, Nucl. Phys. A124 (1969) 553.

(Sa 69)   J. X. Saladin, J. E. Glenn and R. J. Pryor, Phys. Rev. 186 (1969) 1241.

(Sc 70)   G. Schilling, R. P. Scharenberg and J. W. Tippie, Phys. Rev. C1 (1970) 1400.

(Si 68)   J. J. Simpson, U. Smilansky and J. P. Wurm, Phys. Lett. 27B (1968) 633.

(Si 70)   L. Sips and V. Lopac, Phys. Lett. 32B (1970) 649.

(Si 71)   L. Sips, Phys. Lett. 36B (1971) 193.

(Sm 68)   U. Smilansky, Nucl. Phys. A112 (1968) 185.

(Sm 71)   U. Smilansky, Hyperfine interactions in excited nuclei, ed.
          G. Goldring and R. Kalish, vol. 4 (Gordon and Breach, New York,
          1971) p. 1091.

(So 67)   B. Sorensen, Nucl. Phys. A97 (1967) 1.

(So 73)   B. Sorensen, Nucl. Phys. A217 (1973) 505.

(Sp 76)   R. H. Spear, M. T. Esat, D. C. Kean, A. M. Baxter, M. P. Fewell,
          S. M. Hinds, A. M. Joye and J. P. Warner, to be published.

(St 70)   S. G. Steadman, A. M. Kleinfeld, S. G. Seaman, J. de Boer and
          D. Ward, Nucl. Phys. A155 (1970) 1.

(St 67)   R. G. Stokstad, I. Hall, G. D. Symons and J. de Boer, Nucl.
          phys. A92 (1967) 319.

(St 74)   M. Strautmanis, private communication.

(Ta 65)   T. Tamura, Rev. Mod. Phys. 37 (1965) 679.

(Ta 65a) T. Tamura, Phys. Rev. Lett. 15 (1965) 765.

(Ta 66)   T. Tamura, Phys. Rev. 150 (1966) 783.

(Ta 68)   T. Tamura, Phys. Lett. 28B (1968) 90.

(Ta 73)   T. Tamura and T. Kishimoto, J. Phys. Soc. Japan, 34 Supplement
          (1973) 393.

(Ta 75)   T. Tamura, T. Udagawa and T. Kishimoto, invited paper presented
          by T. Tamura at the Symp. on nucl. structure, Balatonfüred,
          Hungary (1975), to be published.

(Th 71)   J. A. Thomson, R. P. Scharenberg and W. R. Lutz, Phys. Rev.
          C4 (1971) 1699.

(Th 73)   D. J. Thomas, I. Hall, M. J. Throop and B. Wakefield, J. Phys.
          A6 (1973) 1571.

(Ue 35)   E. A. Uehling, Phys. Rev. 48 (1935) 55.

(Vi 72)   F. Videbaek, I. Chernow, P. R. Christensen and E. E. Gross,
           Phys. Rev. Lett. 28 (1972) 1072.

(Wa 70)   B. Wakefield, I. M. Naqib, R. P. Harper, I. Hall, and A. Christy,
           Phys. Lett. 32B (1970) 26.

(Wa 64)   A. H. Wapstra, Nucl. Phys. 57 (1964) 48.

(We 51)   W. F. Weisskopf, Phys. Rev. 83 (1951) 1073.

(We 73)   D. Werdecker, A. M. Kleinfeld and J. S. Greenberg, J. Phys.
           Soc. Japan 34 Supplement (1973) 195.

(Wi 66)   A. Winther and J. de Boer, A computer program for multiple
           Coulomb excitation, reprinted in K. Alder and A. Winther,
           Coulomb excitation, (Academic Press, New York, 1966).